

Microscopic Mechanism of the Staebler-Wronski Effect in a-Si Films and High-Efficiency Solar Cells

Subcontract Report
NREL/SR-520-37990
May 2005

Final Subcontract Report
1 October 2001—30 September 2004

D. Han
University of North Carolina
Chapel Hill, North Carolina

NREL is operated by Midwest Research Institute • Battelle Contract No. DE-AC36-99-GO10337



Microscopic Mechanism of the Staebler-Wronski Effect in a-Si Films and High-Efficiency Solar Cells

Subcontract Report
NREL/SR-520-37990
May 2005

Final Subcontract Report
1 October 2001—30 September 2004

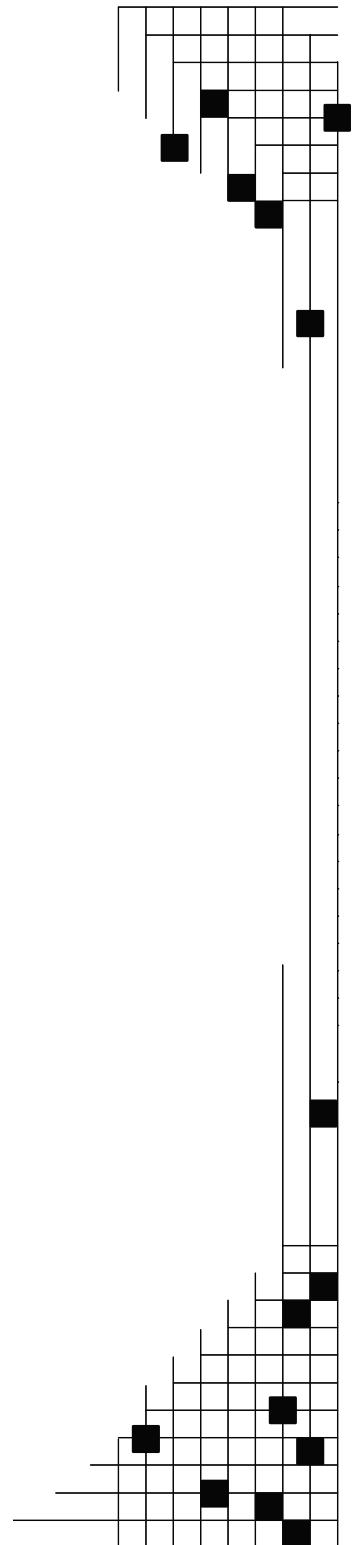
D. Han
University of North Carolina
Chapel Hill, North Carolina

NREL Technical Monitor: Bolko von Roedern
Prepared under Subcontract No. ADJ-1-30630-09

National Renewable Energy Laboratory
1617 Cole Boulevard, Golden, Colorado 80401-3393
303-275-3000 • www.nrel.gov

Operated for the U.S. Department of Energy
Office of Energy Efficiency and Renewable Energy
by Midwest Research Institute • Battelle

Contract No. DE-AC36-99-GO10337



This publication was reproduced from the best available copy submitted by the subcontractor and received no editorial review at NREL.

NOTICE

This report was prepared as an account of work sponsored by an agency of the United States government. Neither the United States government nor any agency thereof, nor any of their employees, makes any warranty, express or implied, or assumes any legal liability or responsibility for the accuracy, completeness, or usefulness of any information, apparatus, product, or process disclosed, or represents that its use would not infringe privately owned rights. Reference herein to any specific commercial product, process, or service by trade name, trademark, manufacturer, or otherwise does not necessarily constitute or imply its endorsement, recommendation, or favoring by the United States government or any agency thereof. The views and opinions of authors expressed herein do not necessarily state or reflect those of the United States government or any agency thereof.

Available electronically at <http://www.osti.gov/bridge>

Available for a processing fee to U.S. Department of Energy and its contractors, in paper, from:

U.S. Department of Energy
Office of Scientific and Technical Information
P.O. Box 62
Oak Ridge, TN 37831-0062
phone: 865.576.8401
fax: 865.576.5728
email: <mailto:reports@adonis.osti.gov>

Available for sale to the public, in paper, from:

U.S. Department of Commerce
National Technical Information Service
5285 Port Royal Road
Springfield, VA 22161
phone: 800.553.6847
fax: 703.605.6900
email: orders@ntis.fedworld.gov
online ordering: <http://www.ntis.gov/ordering.htm>



PREFACE

This final Technical Report covers the work performed by University of North Carolina at Chapel Hill (UNC-CH) for the period Oct.1, 2001 to Sept. 30, 2004 under subcontract No. ADJ-1-30630-09. The report was written by Daxing Han (P.I.) and produced with Keda Wang (co-P.I.) Yue Wu (co-P.I.); Jonathan Baugh; Andrea Hilchey, J.R. Weinberg-Wolf, E.C.T. Harley, Chris Lawyer, and Anthony Canning, graduate students; and Brittany Huie, under graduate student. The samples were obtained from Team members at USOC, BPSolar and the a-Si group at the National Renewable Energy Laboratory (NREL).

This work is part of the amorphous silicon (a-Si:H) teamwork of the National Thin Film PV Program and NREL Thin-Film partnership program. Over the last three years, we have benefited from numerous discussions and cooperation with our Condensed Matter colleagues at UNC-CH, L. E. McNeil, and Y. Wu. At other institutions we have collaborated with: Qi Wang, Yueqing Xu, Lynn Gedvilas, Brent Nelson and Paul Stradins et al. at NREL; Jeff Yang and Baojie Yan et al at USOC; and G. Ganguly at BPSolar. We have also collaborated with S. Nitta and H. Habuch, Gifu University, and Tatsuo Shimizu, Kanazawa University, Japan. Our research has resulted in the publication of 21 papers, 6 papers in press and the submission of quarterly and annual reports. We have completed a review article on *Photo- and electro-luminescence of a-Si:H and mixed-phase alloys* for a special issue of “Solar Energy Materials and Solar Cells” (Elsevier Science) being edited by Hellmut Fritzsche and Subhendu Guha. This article summarizes our recent 10-year work of electroluminescence, the dispersive-transport-controlled recombination, and photoluminescence in a-Si:H and mixed-phase alloys.

TABLE OF CONTENTS

Preface	i
Table of Contents	ii
List of figures	v
List of tables	vii
Results	
I. Nano-voids Related Phenomena in High Growth Rate Intrinsic Hydrogenated Amorphous Silicon Films Prepared by Hot-wire CVD film	1
I.1 Large red shift of PL peak energy in high-growth rate a-Si:H film.....	1
1.1.1 Samples and experimental.....	1
1.1.2 Results and discussion.....	4
1.1.3 Summary.....	4
I.2 Confinement effect on dipole-dipole interactions in nanogas system- NMR results.....	4
1.2.1 Introduction.....	4
1.2.2 Sample and experimental.....	4
1.2.3 Results and discussion.....	5
I.3 Conclusions.....	6
II. Microcrystalline transition from a-Si as a function of hydrogen dilution and substrate temperature of hot-wire CVD	7
II.1 Introduction.....	7
II.2 Samples and Experimental Conditions.....	7
II.3 Results and Discussion.....	8
2.3.1 Raman Spectra.....	8
2.3.2 IR Absorption.....	9
2.3.3 Optical Absorption Spectra.....	13
2.3.4 Conductivity Activation Energy.....	15
2.3.5 PL spectra at 80 K.....	16
II.4 Summary.....	16
II.5. Conclusions.....	17
III. D⁰ May Not Be The Dominant Recombination Centers For Photoconductivity In Hot-Wire a-Si:H	17
III.1 Introduction.....	17
III.2 Sample and Experimental.....	19
III.3 Results.....	20
3.3.1 Natural degradation effect.....	20
3.3.2. Strong recombination center in a-Si:H prepared by HW-CVD.....	21
3.3.3. ESR and CPM studies.....	22
III.4 Summary and Discussion	23

3. 4.1 Summary	23
3. 4.2 Natural degradation effect	23
3. 4.3 Why the activation energy is very large and driven down?	24
III.5 Conclusions	24
IV. PL study of growth rate dependence on solar cells made using DC-CVD by BPSolar	25
IV.1. A special microstructure of high growth rate films	25
4.1.1. A special case of the IR spectra	25
4.1.2. A special case of the PL spectroscopy	27
4.1.3. Summary of the special case	28
IV.2 PL results from a group of new samples	28
4.2.1. Sample and Experimental	28
4.2.2. PL Results	29
4.2.3. In-situ light soaking	30
IV.3. Summary and Discussion	30
V. Systematical Raman study of thin films from amorphous-to-nanocrystalline silicon prepared by HW-CVD	31
V.1. Introduction	31
V.2. Sample and Experimental	32
V.3. Results and discussions	33
V.4. Summary	37
V.5 Conclusion	38
VI. Micro-Raman Studies of Mixed-Phase Hydrogenated Silicon Solar Cells	38
VI.1. Introduction	38
VI.2. Sample and Experimental	39
VI.3. Results and discussions	39
VI.4. Summary	41
VI.5. Conclusion	42
VII. Toward understanding the degradation without light soaking in hot-wire a-Si:H thin films and solar cells	42
VII.1 Introduction	42
VII.2 Experimental Details	42
VII.3 Result and discussion	43
VII.4 Conclusions	46
VIII. Micro-Raman Studies for Electrical-induced Structural Changes in Metal/μc-Si/Metal Structures Made by Hot-Wire CVD	46
VIII.1. Sample and Experiment	46
VIII.2. Results	47
8.2.1. The I-V characteristics of M/a-Si/M and M/ μ c-Si/M structures	47
8.2.2. Raman studies before and after switching of the M/ μ c-Si/M structures	48
VIII.3. Summary	48

VIII.4. Conclusion.....	49
IX. Buffer-layer Effect on Mixed-Phase Cells Studied by Raman and PL Spectroscopy.....	49
IX.1. Introduction.....	49
IX.2. Sample and Experimental.....	49
IX.3. Raman results.....	50
IX.4. PL results.....	51
9.4.1. PL spectra at low temperature.....	52
9.4.2. PL intensity temperature dependence.....	52
9.4.3. <i>in-situ</i> light soaking effect.....	53
IX. 5. Summary.....	53
IX. 6. Conclusion.....	54
X. Correlation of Hydrogenated Nanocrystalline Silicon Microstructure and Solar Cell Performance.....	54
X.1. Introduction.....	54
X.2. Sample.....	54
X.3. Raman and PL results.....	55
X.4. Discussion.....	57
X.5. Summary.....	58
X.6. Conclusion.....	58
FURTHER EFFORTS.....	59
Publications.....	60
References.....	62
ABSTRACT.....	63

List of figures

- Fig. 1.1 (a) Normalized PL spectra excited by a 632 nm laser, (b) the PL peak energies excited by both a 632 nm (solid circles) and a 488 nm laser (open circles) at 80 K as a function of the deposition rate for HW a-Si:H films with growth rates from 10 to 115 Å/s.
- Fig. 1.2 PL spectra as a function of temperature for two HW films with growth rates 10 Å/s.
- Fig. 1.3 The PL main band and defect band from a typical high growth rate film L356. (a) The integrated intensity and (b) the peak energy positions plotted as a function of temperature.
- Fig. 1.4 Raman shift for a-Si:H samples (a) on c-Si substrates, and (b) on ss substrates.
- Fig. 1.5. Illustration of a cross-section of a-Si:H thin-film with a magnified region showing an elongated nanovoid containing a high-density H₂ gas (blue dots). Such voids show strong alignment of the long axis in the growth direction (along the film normal) in the high-growth rate films studied here. The angle Ω is therefore the angle between the external magnetic field (H_0) and the principal axis a of the nanovoid.
- Fig. 1.6. Room temperature proton NMR spectra (a) and their line fits (b) for an a-Si:H thin-film taken at different film orientations with respect to the applied magnetic field (4.7 Tesla). The angle Ω is defined in Fig. 1.5.
- Fig.1.7 Measured dipolar broadening of the o -H₂ peak due to gas-phase intermolecular dipolar interactions, versus Ω . The solid line shows the function $460\text{Hz} \left| P_2(\cos \Omega) \right|$.
- Fig.2.1 Raman shifts from group I and II films with (a) varied hydrogen dilution ratio, R , and (b) varied substrate temperature T_s . The Raman spectrum from the reference film is shown on the bottom of Fig. 2.1(a).
- Fig. 2.2 The IR spectra in three frequency ranges of 550-750 cm⁻¹, 750-1200 cm⁻¹ and 1800-2200 cm⁻¹ that cover the Si-H wag mode, the SiH₂ bending mode, Si-O modes, and the stretch modes. for (1a, 1b, 1c) group I and (2a, 2b, 2c) group II films. The values of R and T_s are indicated in the legend.
- Fig. 2.3 The correlation of C_H (●) and the relative intensity of the 2090 cm⁻¹ peak $I_{2090}/(I_{2000}+I_{2090})$ (○) with microcrystallinity for (a) group I and (b) group II films.
- Fig. 2.4 Optical absorption spectra obtained by using CPM and fitted by TRS for (a) group I and (b) group II films. The values of R and T_s are indicated in the legend. The absorption spectrum for c-Si is plotted in (a) for reference.
- Fig. 2.5 the optical absorption coefficient at 1.4 eV (●) and the c-Si volume fraction (Δ) as a function of (a) R , and (b) T_s .
- Fig. 2.6 Position of Fermi-level (●) and the c-Si volume fraction (Δ) as a function of (a) R , and (b) T_s .
- Fig. 2.7 Relative PL spectral intensity at 80 K for (a) group I and (b) group II films. The PL spectrum for the reference film is show on the bottom of Fig. 1(a).
- Fig. 3.1 Distribution function (a) for strong recombination and (b) for weak recombination relative to re-trapping. E_d is the thermalization demarcation energy, E_q is the quasi-Fermi level and E_c is the electron mobility edge.
- Fig. 3.2 The conductivities before, during and after light soaking for typical intrinsic a-Si:H films made by HW-CVD (solid line) and PE-CVD (dotted line).
- Fig. 3.3 Temperature dependence of photo- and dark conductivity before and after 200 mW/cm² white light soaking for 4 h, (a) for HW-CVD film T779 and (b) for PE-CVD film A7119.
- Fig. 3.4 Thermostimulated conductivity for the same samples in Fig. 3 at annealed State A and light-soaked State B, (a) for HW-CVD film T779 and (b) for PE-CVD film A7119.
- Fig. 3.5 The density of defects for HW- and PE-CVD films before and after 200 mW/cm² white light soaking for 30 h. (a) Measured by CPM, (b) measured by ESR, and (c) light-induced metastable defects measured by CPM and ESR.
- Fig. 4.1 Raman shift for samples with growth rates of 1, 3 and 10 Å/s.

- Fig. 4.2 IR spectra for samples of (a) L0172-3, L0172-4, and L0173-1, (b) L0276-1c, L0277-1c, and L0278-1c.
- Fig. 4.3 PL results for samples L0276-1, L0277-1, and L0278-1 (a) spectra at 80 K, (b) spectra at 180 K.
- Fig. 4.4 PL peak energy as a function of temperature for samples L0276-1, L0277-1, and L0278-1.
- Fig. 4.7 Peak_{main} of samples L2127, L2129, L2316 and L2317 as a function of temperature.
- Fig. 4.8 I_{main} of samples L2127, L2129, L2316 and L2317 as a function of temperature.
- Fig. 4.9 Relative intensity of the I_{defect} as a function of temperature for the four samples.
- Fig. 4.10 Relative intensity of the I_{defect} at 260 K as a function of the sample growth rate before and after in-situ light soaking.
- Fig. 4.11 the Peak_{main}, I_{main}, and I_{defect} vs. T for sample L2127 at State A and State B.
- Fig. 5.1. X_c as a function of R at SiH₄ flow rates of 3, 8, 16 and 22 sccm. The solid and dotted lines indicate the X_c was obtained from the top or bottom layer of ≥ 60 nm, respectively.
- Fig. 5.2. Raman shift and their fittings from the films with SiH₄ flow of 3 sccm, TVP=45%, (a) R=1, and (b) R=2. And the enlarged TO mode of the data in 2(c) and 2(d).
- Figs. 5.3.(a) FWHM and (b) ω_{a-Si} of the TO mode as function of R. The solid dots, dashes, open circles, and crosses represent the films with a SiH₄ flow rate of 3, 8, 16, and 22 sccm, respectively. There are two regimes separated at R \approx 3: the fast changing regime when R <3 and the saturated regime when R >3.
- Fig. 5.4. ω_{c-Si} as a function of R.
- Fig. 5.5. $\omega_{g,b}$ as a function of R.
- Figure 6.1. Schematics of (a) 4 scans for all samples, and (b) 20 scans for 13678-42. The diameter of the dot is ~ 3 μ m.
- Fig. 6.2 Raman spectrum of 13687-32.
- Fig. 6.3 Raman spectrum of 13678-13.
- Fig. 6.4. Raman shifts of mixed-phase cells with (a) V_{OC} = 0.767 V and (b) V_{OC} = 0.748 V.
- Fig. 6.5. Raman Shift of 20 scans on a mixed phase cell 13678-42.
- Fig. 7.1 The hot-probe data for sample T837.
- Fig. 7.2. (a) Current-temperature dependence and (b) current as a function of annealing time at 420 K, for samples of H1441 and H1442 with- and without SiN_x passivation layer. The samples were mounted in the vacuum and in pure oxygen or nitrogen, respectively.
- Fig. 7.3 Degradation experiments: (a) the dark current at 300 K for samples of H1540a in vacuum (\times), H1540b in pure O₂ (\circ), and H1540c in the air (Δ). The data following the arrows indicate the current after E_a measurements. (b) Several measurements of E_a obtained from those three samples after the current measurements at 300 K for about a month. The data following the arrow indicate the measurements were done in vacuum for H1540c.
- Fig. 7.4 PC temperature dependence for (a) HW film T779 and (b) PE-CVD film A7119.
- Fig. 8.1. Typical switching voltage vs. current traces in (a) a 80 μ m-diameter Cr/p⁺a-Si:H/Ag and (b) a $\sim 5 \times 5$ μ m² Cr/p⁺ μ c-Si/Ag devices.
- Fig. 8.2. The Raman spectra fitted using three functions for (a) the seven non-switched, (b) the eight switched devices, and (c) comparing the spectra in (a) and (b).
- Fig. 9.1. Raman spectra for the cells on (a) L13869, (b) L13868, and (c) L13870, corresponding to no buffer layer, 100 Å thick a-Si:H buffer layer, and 500 Å thick a-Si:H buffer layer, respectively.
- Fig. 9.2. PL spectra at 80 K for cells 11, 13, and 22 on sample 13869 for (a) linear and (b) semi-log plots.
- Fig. 9.3. PL spectra of the low V_{oc} cells of L13869-11, L13868-11, and L13870-11 for (a) linear and (b) semi-log plots.
- Fig. 9.4. PL intensities vs. temperature for cells of (a) L13869, (b) L13868, and (c) L13870, where circles represent the a-Si:H main band, triangles the g.b. band, and squares the defect band.
- Fig. 9.5 PL spectra at 80 K before and after light soaking for cells of (a) L13869-11, (b) L13868-11, and (c) L13870-11.
- Fig. 10.1. Raman spectra of the eight nc-Si:H solar cells.

Fig. 10.2. PL spectra of the same nc-Si:H solar cells at 80 K excited by 632.8-nm (solid) and 442-nm (dashed) laser beams.

List of tables

Table I.1. Characteristics of a-Si:H samples with high growth rate.

Table II.1. Preparation conditions and parameters of the transition films prepared by HW-CVD.

Table II.2. The energy peak position and the bandwidth of the Si-H vibration modes.

Table III.1. Sample preparation conditions.

Table III.2. Conductivity activation energies at initial- annealed- and light soaked states.

Table IV.1. Sample preparation conditions, i-layer properties and their solar cell performances.

Table IV.2. Hydrogen content and the absorption strengths of Si-H vibration modes.

Table IV.3. The sample preparing conditions and their PL parameters.

Table VI.1. Sample V_{OC} with Raman results

Table VII.1. Sample information

Table IX.1. The initial performance of the mixed-phase solar cells with different a-Si:H buffer layers at the *i/p* interface.

Table X.I. Preparation conditions and solar cell performance of the nc-Si:H solar cells studied.

Table X.2. Summary of the Raman and PL analyses of the nc-Si:H solar cells.

I. Nano-voids Related Phenomena in High Growth Rate Intrinsic Hydrogenated Amorphous Silicon Films Prepared by Hot-wire CVD

1.1. Large red shift of PL peak energy in high-growth rate a-Si:H films[1]

1.1.1 *Sample and experimental:* The growth rates and the characteristics of the hydrogenated amorphous silicon (a-Si:H) films are listed in Table I. As a reference, a standard device-quality hot-wire chemical vapor deposition (HW-CVD) film was deposited on quartz substrate. For the following photoluminescence (PL) measurements, either a 632 or a 488 nm wavelength laser beam with a light-chopper at frequency 17 Hz was used. The sample was mounted on a cold stage. The steady state PL spectra were analyzed using a grating monochromator equipped with a liquid nitrogen-cooled Ge detector. The signals were recorded by a lock-in amplifier.

Table I.1. Characteristics of a-Si:H samples with high growth rate.

Sample ID	Growth rate ($\text{\AA}/\text{s}$)	Mass density (% of c-Si density)	E_{opt} (eV)	PL _{peak} at 80 K (eV)	$^1\text{H-NMR}$ very narrow line (%)	Nanovoid volume fraction ^a (%)	Raman TO mode Peak (cm^{-1})	FWHM (cm^{-1})
Standard	10	98.0	1.68	1.36	Absence	<0.01	480	70
L388	30			1.23		1-2	"	"
L256	50			1.05		~2	"	"
L354	55	96.0	1.65	1.10	36	~2	"	"
L353	80	95.8	1.67	1.14	27	~2	"	"
L252	90			1.12		2-3	"	"
L355	100	95.3	1.65	1.14	24	~2	"	"
L259	110			1.14		2-3	"	"
L356	115	95.1	1.66	1.14	20	~2	"	"

^a From both mass density and reference

1.1.2 Results and discussion:

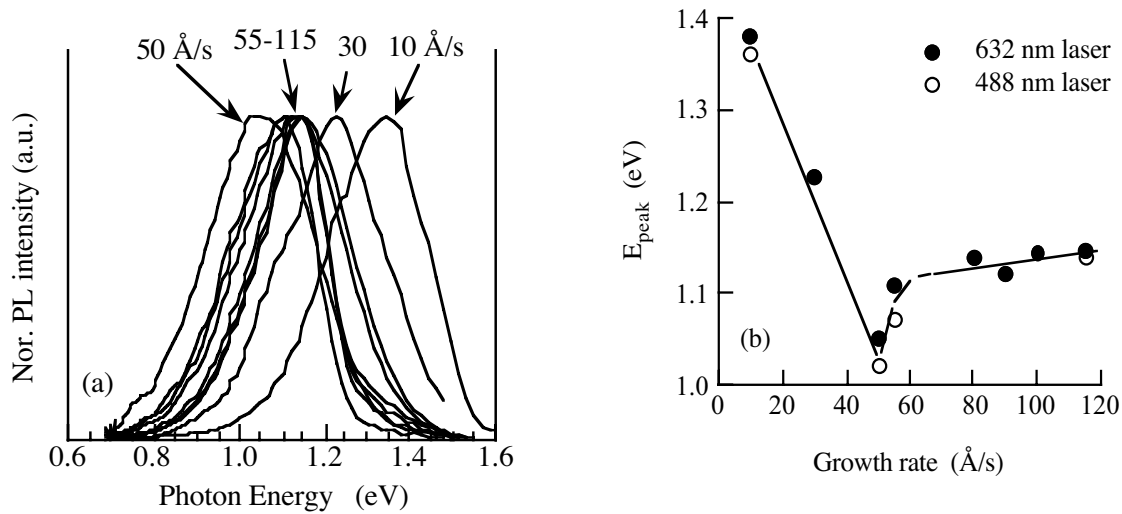


Fig. 1.1 (a) Normalized PL spectra excited by a 632 nm laser, (b) the PL peak energies excited by both a 632 nm (solid circles) and a 488 nm laser (open circles) at 80 K as a function of the deposition rate for HW a-Si:H films with growth rates from 10 to 115 $\text{\AA}/\text{s}$.

In typical intrinsic a-Si:H made by plasma-enhanced (PE)-CVD, the PL spectrum at 80 K is dominated by the tail-to-tail radiative transitions that give a PL main-band peaked at ~ 1.4 eV with full width at half maximum (FWHM) ≈ 0.3 eV. A defect-band peaked at ~ 0.9 eV is 3-4 orders of magnitude weaker than the main band at low temperatures. As the temperature is increased, the PL intensity (I_{pl}) is quenched by non-radiative recombination, and the main-band peak energy position (PL_{peak}) decreases due to carrier thermalization down to the lower-energy band tail states. The PL features of the standard low-deposition rate HW-CVD film are similar to those of PE-CVD film. Surprisingly, the main peak energy PL_{peak} is extremely low at 80 K in the high-growth rate films compared to the standard film. Fig. 1.1a shows normalized PL spectra excited by a 632 nm laser. The PL_{peak} decreases rapidly from 1.36 to 1.05 eV when the growth rate increases from 10 to 50 Å/s; it then reaches a saturated value of ~ 1.1 eV for growth rates > 50 Å/s. The PL red shift is as large as 0.25 to 0.30 eV. One may question whether the excitation photon energy of the 632 nm laser is large enough for achieving intrinsic excitation. Therefore, we also used a 488 nm laser to excite the PL. Fig. 1.1b plots the PL_{peak} excited by both 632 and 488 nm laser at 80 K as a function of the deposition rate. Using the 488 nm laser, we observed a PL_{peak} position even 10-30 meV lower than that obtained using the 632 nm excitation. This can be understood as resulting from film non-uniformity in the growth direction and the more shallow penetration of the 488 nm laser beam probing a film portion close to the surface. The PL efficiency, on the other hand, is similar to that of the standard film in all the high-growth rate films.

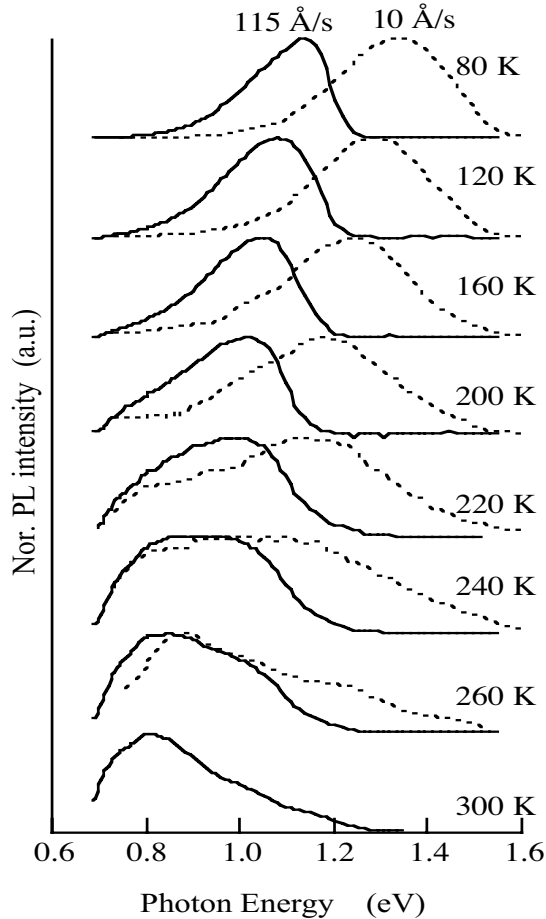


Fig. 1.2 PL spectra as a function of temperature for two HW films with growth rates 10 Å/s.

To explore whether or not the PL follows carrier thermalization in band tails, we measured the PL temperature dependence. Fig. 1.2 shows normalized PL spectra excited by a 488 nm laser as a function of temperature for the film deposited at 115 Å/s. The standard film PL spectra are plotted as a reference. At low temperatures, the PL main-band dominates. We see clearly that the PL_{peak} red shifts. As the temperature increases, the 0.8-eV defect band gradually dominates, and the PL spectral lineshapes of the two films become similar. The data was fitted using two Gaussian functions f1 and f2 with line widths of 0.20 eV and 0.25 eV representing the main and defect bands, respectively. Figure 1.3a shows the thermal quenching of the PL main-band intensity and a weak temperature dependence of the defect band intensity. Figure 1.3b shows that the PL_{peak1} of the PL main band decreases from 1.15 to 1.04 eV as the temperature increases from 80 K to 180 K and saturates at ~ 1.04 eV (at which the carriers reach the bottom of the tail states). On the other hand, the peak energy position of the defect band, PL_{peak2} , decreases from 0.90 to 0.82 eV as the temperature increases from 150 to 300 K. The results in Fig. 1.3 indicate that both the PL intensity and the peak energy follow the model of carrier thermalization in band tail states. However, the large red shift of the PL main-band (from tail-to-tail transition) is puzzling since the optical gap of the high rate film is similar to that of the standard film.

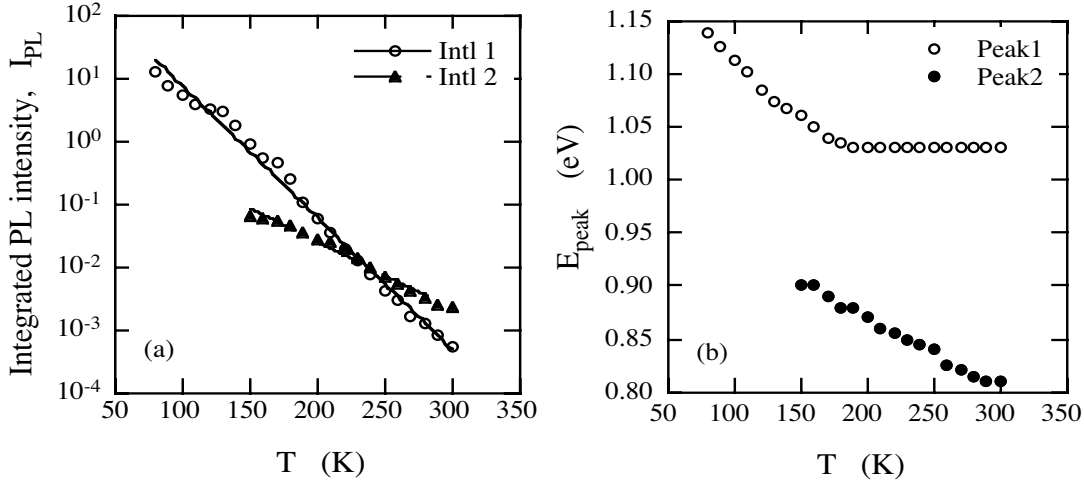


Fig. 1.3 The PL main band and defect band from a typical high growth rate film L356. (a) The integrated intensity and (b) the peak energy positions plotted as a function of temperature.

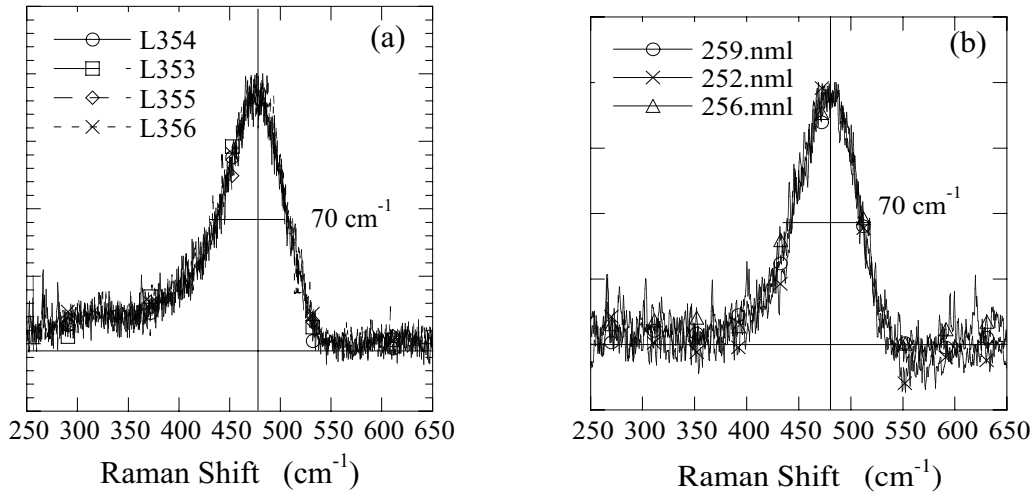


Fig. 1.4 Raman shift for a-Si:H samples (a) on c-Si substrates, and (b) on ss substrates.

To explore how the microstructure could be related to the PL red shift, we first measured the Raman shift. The spectra in Figs. 1.4(a) and 1.4(b) show the same lineshapes as standard device-quality a-Si:H, i.e. transverse optical (TO) mode peaked at $\sim 480 \text{ cm}^{-1}$ with FWHM $\sim 70 \text{ cm}^{-1}$ for all the films in Table I. We further studied the hydrogen microstructure and the material structural ordering by ^1H -nuclear magnetic resonance (NMR) and mass density measurement. We found a very narrow Lorentzian component in the spectra with $\sim 1 \text{ kHz}$ linewidth in addition to the conventional Lorentzian ($\sim 3 \text{ kHz}$) and Gaussian ($\sim 40 \text{ kHz}$) components in the high growth rate films L353-L356. This very narrow component is related to molecular hydrogen that is absent in the standard film but comprises 20-30% of the total spectral intensity for the four samples L353-356. The mass densities were obtained by the flotation method. The average

was 2.28 ± 0.02 and 2.22 ± 0.02 (g/cm^3) for the standard films and the high growth rate films, respectively. We obtain a $\sim 2\%$ volume fraction of the nanovoids in the high growth rate films. This H_2 peak exhibits a long room-temperature spin-lattice relaxation time (T_1) ~ 1.2 s, which implies that there is a negligible density of spin-lattice relaxation centers (i.e. dangling bonds) associated with the nanovoids. This lack of dangling bonds may indicate an ease of weak bond formation on the surfaces. Additionally, the spin-spin relaxation time (T_2) of the H_2 peak shows a dependence on the film orientation with respect to the dc magnetic field. Such unusual anisotropy in a gas system can only be understood if we consider the effects of confinement in nano-scale voids that are non-spherical and on the average aligned in the film. The experimental NMR results of the H_2 peak fit well with the calculated properties of H_2 in an elongated elliptical geometry of 1-3 nm diameter and length several times the diameter. Meanwhile, we have learned that small-angle x-ray scattering (SAXS) also indicates that the 1-3% volume fraction nanovoids are elongated and aligned in the high growth rate films.

1.1.3 Summary: A large red shift of the PL peak energy is found in a-Si:H films prepared by HW-CVD with a high growth rate ≥ 50 $\text{\AA}/\text{s}$. The origin of the red shift is clarified by employing ^1H nuclear magnetic resonance (NMR) and mass density measurements. A $\sim 2\%$ volume fraction of tube-like nanoscale voids is identified. We suggest that highly strained bonds on these surfaces form broad conduction-band tail states that are responsible for the PL red shift.

1.2. Confinement Effect on Dipole-dipole Interactions in Nanogas System -NMR Results[2]

1.2.1 Introduction: Intermolecular dipole-dipole interactions were once thought to average to zero in gases and liquids as a result of rapid molecular motion, which leads to sharp nuclear magnetic resonance (NMR) lines. Recent papers have shown that small residual couplings survive the motional averaging if the magnetization is nonuniform or nonspherical. Here, we show that a much larger, qualitatively different intermolecular dipolar interaction remains in nanogases and nanoliquids as an effect of confinement. The resulting dipolar coupling is identical for all spin pairs and depends on the volume of the gas/liquid container, its shape and orientation with respect to the magnetic field. This nanoscale effect is quite useful in the determination of nanostructures and could have unique applications in the exploration of quantum space.

1.2.2 Sample and experimental: Proton NMR is carried out on a pulsed NMR spectrometer operating at a radio frequency of 200 MHz in an external magnetic field of 4.7 Tesla. The low proton background was achieved by employing homemade plastic-free capacitor in the resonant tank circuit of the probe. Only carefully etched and cleaned metal or metal-shielded parts are placed in the region of homogeneous magnetic field. The sample region was purged by constant flow of dry nitrogen gas to avoid moisture in the air. For the measurement of a single a-Si:H film on quartz substrate a flattened solenoid NMR coil was employed. The flat coil surface orientation can be varied with respect to the external magnetic field for the measurement of orientation dependence. The typical employed 90° rf pulse is 1.5 μs . The temperature variation was achieved by placing the rf coil in a resistive furnace. In order to remove the effect of the heating current which could generate magnetic field, the current power supply was controlled by the pulse programmer of the spectrometer through a TTL pulse, which turns on or off the heating current in about 50 ms. The heating current was off during the NMR data acquisition time of about 16 ms and was turned back on immediately thereafter. Stable and homogeneous temperature across the sample can be achieved by this method over a long time period.

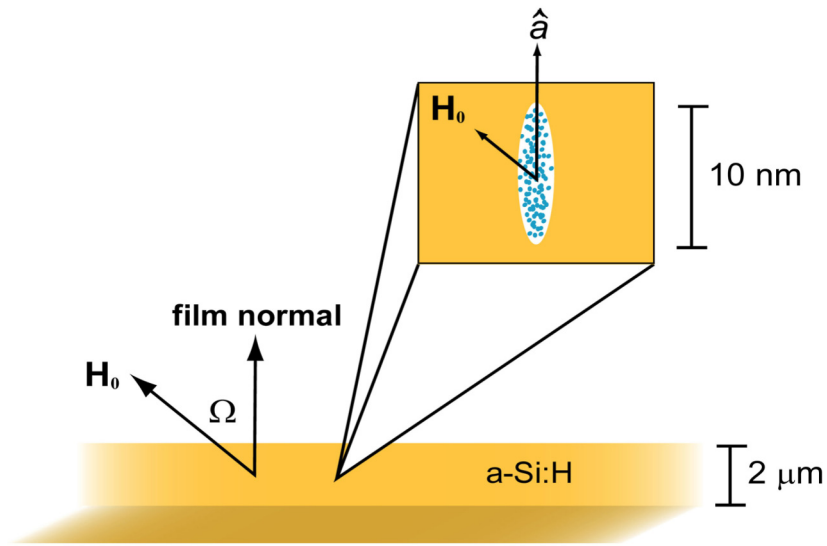


Fig. 1.5. Illustration of a cross-section of a-Si:H thin-film with a magnified region showing an elongated nanovoid containing a high-density H₂ gas (blue dots). Such voids show strong alignment of the long axis in the growth direction (along the film normal) in the high-growth rate films studied here. The angle Ω is therefore the angle between the external magnetic field (H_0) and the principal axis a of the nanovoid.

1.2.3 Results and discussion:

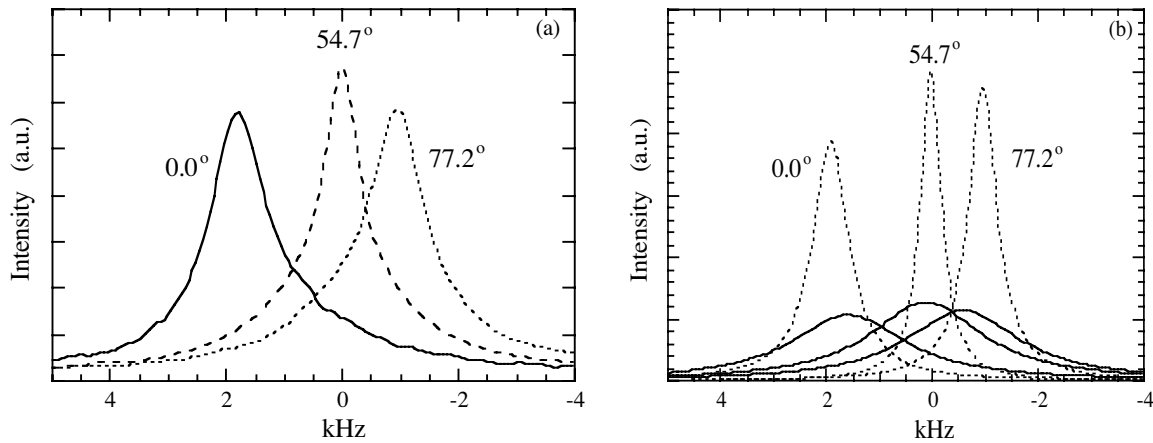


Fig. 1.6. Room temperature proton NMR spectra (a) and their line fits (b) for an a-Si:H thin-film taken at different film orientations with respect to the applied magnetic field (4.7 Tesla). The angle Ω is defined in Fig. 1.5.

It is well known that a-Si:H possesses nanovoids, which contain high-pressure H₂ gas of up to 2 kbar. Recently, it was found [2] that such nanovoids are elongated and aligned perpendicular to the film surface in a-Si:H produced by HW-CVD at high growth rate, as illustrated in Fig. 5. Small angle x-ray scattering

(SAXS) shows that the total volume fraction of such nanovoids is $\sim 2\%$ and that the estimated diameters of the nanovoids are a few nm and the lengths are several times longer than the diameter. To investigate the angular dependence NMR measurements were carried out on a single a-Si:H film about $1 \mu\text{m}$ thick on quartz substrate using a flattened solenoid coil in an ultralow ^1H background probe. Figure 6 shows the room temperature (RT) ^1H spectra of high growth rate (55 \AA/s) HW-CVD a-Si:H at $\Omega=0^\circ$, 55° , and 77° . The inset of Fig. 6 shows both the conventional broad (FWHH=35 kHz) and narrow (FWHH=3.3 kHz) peaks associated with Si-H clusters and isolated Si-H bonds, respectively. In addition, a narrower peak with FWHH of less than 1 kHz is also visible. This peak arises from H_2 in nanovoids and broadens significantly below 60 K due to the slow-down of H_2 motion and subsequent H_2 freezing. Fittings of the conventional narrow peak and the H_2 peak are also shown in Fig. 1.6.

The contribution of the dipole-dipole interactions to this linewidth was determined by the Hahn-echo decay using the pulse sequence $90^\circ - t - 180^\circ - t - \text{echo}$. As expected, the rate of the echo height decay is the slowest at $\Omega=55^\circ$ and follows $\exp(-2t/T_2)$ with $T_2=1.3 \text{ ms}$. The Ω -dependent part of the Hahn-echo decay was determined from the Gaussian part of the decay function. Figure 7 shows the measured $2.36\sqrt{M_2}/2\pi$ versus the angle Ω . The experimental data are consistent with the calculation very well.

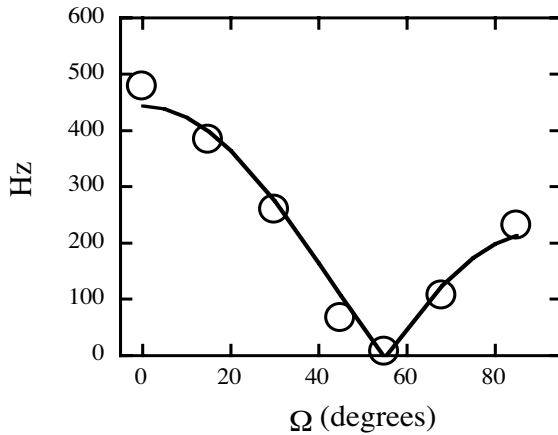


Fig.1.7 Measured dipolar broadening of the $o\text{-H}_2$ peak due to gas-phase intermolecular dipolar interactions, versus Ω . The solid line shows the function $460\text{Hz} |P_2(\cos \Omega)|$.

The NMR results clarified that the nanovoids are not only related to dangling bond defect centers but could be related to radiative centers. We propose that highly strained bonds (weak bonds) on the surfaces of the tube-like nanovoids result in a broad conduction band tail. In a recent molecular dynamics study of band tails in a-Si:H, Fedders et al [3] conclude that stretched bonds affect the conduction band tail; whereas, short bonds affect valence band tail states. The nanovoid-related states do not produce a new type of luminescence center but only contribute to the continuous distribution of tail states. Therefore, such states could cause the peak energy to red shift instead of forming a new PL peak. [1].

1.3 Conclusions:

We observed new phenomena in high growth rate HWCVD a-Si:H films by PL and NMR. We explain that the nonsocial elongated nanovoids filled with one-dimensional H_2 gas alignment in the growth direction in the high-growth rate films.

II. Microcrystalline transition from a-Si as a function of hydrogen dilution and substrate temperature of hot-wire CVD [4]

II.1 Introduction

The transition films from amorphous (a)- to microcrystalline (μc) -Si:H have attracted a great deal of attention because the most stable, high-performance a-Si:H solar cells were prepared at a hydrogen-to-disilane dilution ratio just below the onset of microcrystallinity. On the other hand, μc -Si:H films can be directly deposited at substrate temperatures (T_s) of 200-300 °C in a PE-CVD system with a varied hydrogen dilution ratio, $R=\text{H}_2:\text{SiH}_4$. However, the reaction gas must be highly diluted by hydrogen such as $20 < R < 100$ which leads to a very low deposition rate. Many efforts have been made to increase the deposition rate such as using very high frequency plasma CVD and a microwave-based CVD techniques. Nevertheless, a one-step high growth rate process is desirable for device applications. A deposition rate of ~ 10 Å/s is standard for HW-CVD technique without using hydrogen dilution. In order to utilize the preparation conditions to make device-quality transition films, the correlation between the preparation conditions, the structure of the materials, the hydrogen configuration, and the optoelectronic properties need to be studied.

II.2 Samples and Experimental Conditions

Table II.1. Preparation conditions and parameters of the transition films prepared by HW-CVD.

Sample	ID	T_s (°C)	R H_2/SiH_4	Thickness (μm)	Dep. Rate (Å/s)	C_H (at.%)	E_{opt} (eV)	n	c-Si volume fraction (%)	
Group I	H955	250	0	0.8	4.7	12.6	1.76	3.55	0	
	H946	250	1	0.5	4.7	10.9	1.80	3.60	0	
	H948	250	2	0.7	4.7	8.9	1.78	3.45	2	
	H947	250	3	0.7	4.7	6.2	1.82	3.36	43	
	H945	250	10	1.0	1.0	3.9	4.1	1.77	3.36	82
	*	T519	240	20	1.1	2.3	3.9	1.75	3.24	92
Group II	H954	150	3	0.7	4.3	9.7	1.81	-	0	
	H951	200	3	0.7	4.7	8.3	1.80	3.4	3	
	H947	250	3	0.7	4.6	6.2	1.81	3.36	41	
	H950	350	3	0.7	4.7	5.5	1.78	3.41	44	
	H952	450	3	0.7	4.4	3.8	1.74	3.53	36	
	H953	550	3	0.7	4.4	3.2	1.72	3.52	37	
Ref.	H949	560	0	1.0	9.0	7.1	1.72	-	0	

* The sample was deposited in the tube system.

C_H , E_{opt} and n represent the hydrogen content, the Tauc optical gap, and the refraction index

Intrinsic a-S:H films were deposited by HW-CVD on c-Si substrate for IR, on rough-surface Corning 1737 glass for PL and Raman, on smooth surface Corning 1737 glass for transmission spectroscopy (TRS), constant photocurrent method (CPM) and conductivity studies. Coplanar Cr electrodes were evaporated on the top of the films for CPM and conductivity measurements. Group I films were deposited at the same substrate temperature, $T_s = 250$ °C, with varied R from

0 to 10. Group II films were deposited at the same $R=3$ with varied substrate temperature, T_s , from 150 to 550 °C. In addition, a reference sample was deposited at 560 °C with pure silane. The film preparation conditions and parameters are listed in Table II.1. Raman spectra were measured using an XY triple spectrograph equipped with a LN_2 -cooled CCD camera. The data were taken at room temperature using the 514.5 nm line of an argon-ion laser. The power of the laser was kept below the level that would thermally induce crystallization. IR spectra were measured at room temperature by a commercial FTIR spectrometer. The details of IR measurements can be found elsewhere [4]. For PL measurements, a micro-refrigerator operating between 80 to 300 K was used to mount the sample. A 5-mW HeNe laser with a bandpass filter was used for PL excitation. The penetration depth of the 632.8 nm light in a-Si:H was $\sim 1 \mu m$ which is greater than the sample thickness. Between consecutive measurements, the sample was kept at the same position and the experimental error was < 10 meV in the experimental range of photon energy. The luminescence signal was dispersed by a grating monochromator and then collected by a liquid-nitrogen-cooled Ge detector. The lock-in technique was used with a light chopper at a frequency of 17 Hz. The optical absorption spectra were studied by using CPM combined with TRS at room temperature.

II.3 Results and Discussion

2.3.1 Raman spectrum

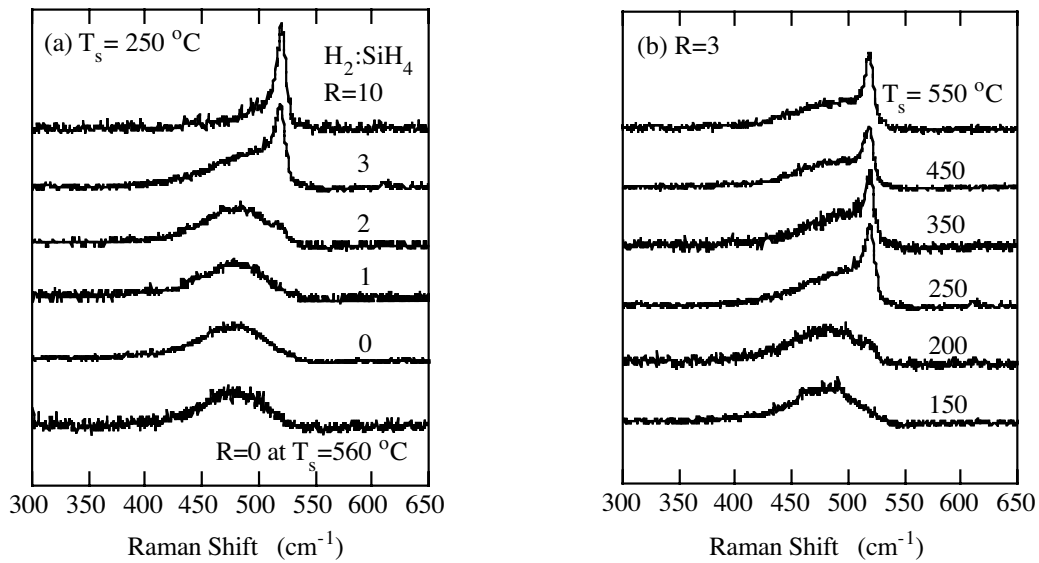


Fig.2.1 Raman shifts from group I and II films with (a) varied hydrogen dilution ratio and (b) varied substrate temperature. The reference is shown on the bottom of Fig. 2.1(a).

The material structure was measured by Raman spectra. For device-quality a-Si:H films, the TO mode peaks at 480 cm^{-1} with a bandwidth of $\sim 70 \text{ cm}^{-1}$. The Raman lineshape does not change with microvoid density in high growth rate films. Figs. 2.1(a) and 2.1(b) show the Raman results from these two groups of films, respectively. The Raman result from the reference film is shown on the bottom of Fig. 2.1(a). Concerning the hydrogen dilution dependence, when $R \leq 1$, the film remains in the amorphous phase characterized by the broad band centered at 480 cm^{-1} . When the hydrogen dilution ratio becomes $R=2$, one can see an emergence of the band at 520 cm^{-1} . The 520 cm^{-1} band grows as R continues to be increased. Finally, the 520 cm^{-1} band dominated at $R=10$. Fig. 2.1(b) shows the substrate temperature

dependence. At $T_s < 200$ °C, the film remains amorphous; when $T_s = 200$ °C, there is an emergence of the band at 520 cm^{-1} . When $T_s \geq 250$ °C, a saturated height of the narrow band at 520 cm^{-1} is observed after the onset of microcrystallinity. Unlike the case of increasing R , there is no gradual increase of the 520 cm^{-1} band as T_s continues to be increased. Nevertheless, using H-dilution is a necessary condition for crystalline transition within this temperature range. As shown on the bottom curve in Fig. 2.1(a), although the T_s was as high as 560 °C, the film was still in a full amorphous phase without hydrogen dilution.

$\mu\text{c-Si}$ materials consist of the a-Si matrix, the c-Si grain and the grain boundaries (g.b.). For the best curve fitting we used three components: the narrow crystalline band at 520 cm^{-1} , a Gaussian function peaked at 480 cm^{-1} with a full width at half maximum (FWHM) 72 cm^{-1} , and the Gaussian function peaked at 498 - 505 cm^{-1} which is associated with bond dilation at grain boundaries. Notice, for these two groups of films, the a-Si:H band was at the same energy position with the same FWHM. It implies that the growth of the c-Si grains does not change the local Si-Si bonding structure of the a-Si:H matrix. The crystalline and g.b. volume fractions, X_c , and X_{gb} were estimated from $X_c = (I_c + I_{gb}) / [I_c + I_{gb} + y(L)I_a]$, and $X_{gb} = I_{gb} / [I_c + I_{gb} + y(L)I_a]$ where I_c , I_a , and I_{gb} are integrated intensities of the crystalline, amorphous, and intermediate peaks, respectively, and $y = 0.9$ was used. The results are listed in Table II.1.

2.3.2. IR Absorption

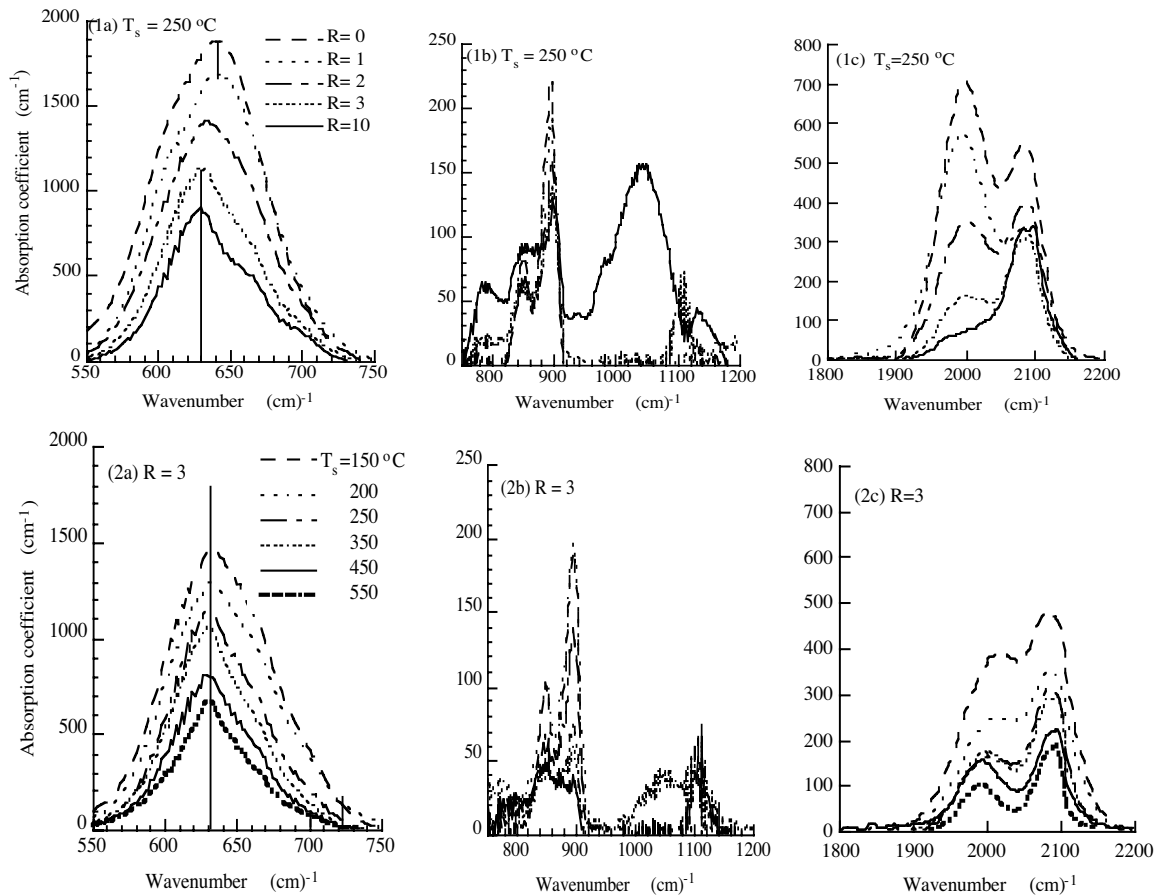


Fig. 2.2 The IR spectra in three frequency ranges of 550 - 750 , 750 - 1200 and 1800 - 2200 cm^{-1} that cover the Si-H wag mode, the SiH_2 bending mode, Si-O modes, and the stretch modes for (1a, 1b, 1c) group I and (2a, 2b, 2c) group II films. The values of R and T_s are indicated in the legend.

Hydrogen plays a crucial role in determining the structural phase transition of a-Si:H. The question then arises as to what are the hydrogen distribution and local bonding configuration in regard to the microcrystallinity. IR spectra were used to study the Si-H vibration absorption. Generally, IR spectra of a-Si:H consist of three absorption regions: at 630 cm⁻¹ related to the SiH wag mode, a doublet at 850, 890 cm⁻¹ related to SiH₂ bending modes, and the peaks at 2000-2090 cm⁻¹ related to SiH stretch modes. In Figs. 2.2(1a, 1b, 1c) and 2 (2a, 2b, 2c) we show the IR spectra in the three frequency ranges of 550-750 cm⁻¹, 750-1200 cm⁻¹ and 1800-2200 cm⁻¹ that cover the SiH wag mode, the SiH₂ bending mode, SiO modes, and the stretch modes. The IR spectrum from the reference film is not shown in Fig. 2.2. Instead, the calculated results are listed in Table II.2. All the peaks in Fig. 2 were fitted using Gaussian functions and the integral intensity $I = \int \omega^{-1} \alpha(\omega) d\omega$ was calculated. Assuming the absorption strength, A, is a constant, the corresponding hydrogen concentrations, N₆₃₀, N_{850,895}, N₂₀₉₀ and N₂₀₀₀, were calculated using $A_{630} = 2.1 \times 10^{19} \text{ cm}^{-2}$, $A_{850,895} = 2 \times 10^{19} \text{ cm}^{-2}$, $A_{2090} = 2.2 \times 10^{20} \text{ cm}^{-2}$ and $A_{2000} = 9.0 \times 10^{19} \text{ cm}^{-2}$. The peak energy positions and the bandwidth (FWHM) for the SiH wag and stretch modes as well as the percentage of the 850-895 cm⁻¹ mode concentration, $N_{850,895}/N_{630} = I_{850,895}/I_{630}$, and the percentage of the 2090 cm⁻¹ mode absorption, $I_{2090}/(I_{2000} + I_{2090})$ are listed in Table II.2. For both group I and II films, the IR spectra mainly contain the monohydride modes at 630 cm⁻¹ and at 2000-2090 cm⁻¹. The absorption of the dihydride-bending mode at 850-895 cm⁻¹ is an order of magnitude lower compared to the 630 cm⁻¹ absorption.

Table II.2 The energy peak position and the bandwidth of the Si-H vibration modes.

Sample ID	T _s (°C)	R	Wag mode Peak, FWHM (cm ⁻¹)		Stretch mode 1 Peak, FWHM (cm ⁻¹)		Stretch mode 2 Peak, FWHM (cm ⁻¹)		I ₂₀₉₀ /(I ₂₀₀₀ +I ₂₀₉₀) (%)	N _{850,895} /N _H (%)
H955	250	0	640	89	2000	86	2085	62	32	3
H946	250	1	640	89	1995	94	2088	62	23	3
H948	250	2	635	87	2002	94	2088	62	38	3
H947	250	3	631	75	2005	94	2090	62	52	5
H945	250	10	631*	68	2010	113	2088	62	68	5
H954	150	3	630	87	2000	112	2090	69	38	4
H951	200	3	630	87	2000	112	2092	69	42	5
H947	250	3	630	76	2005	95	2090	60	52	5
H950	350	3	630	69	2001	86	2088	55	50	3
H952	450	3	630	64	1995	86	2088	55	46	4
H953	550	3	630	57	1996	67	2088	45	50	5
H949	560	0	635	95	1996	86	2088	86	14	0.4

* There is a small shoulder at 690 cm⁻¹

Therefore, we calculate the hydrogen concentration from the wag mode absorption. In comparison, it will be calculated from the stretch mode later. Assuming all the hydrogen is bonded in the matrix, the IR absorption at frequency ω is related to the hydrogen concentration by

$$N_H = AI = A \int [\alpha(\omega)/\omega] d\omega \quad (2.1)$$

where A is sensitive to the local field. Usually, the value of A is deduced experimentally using independent techniques to measure the total hydrogen content. Previous work has shown that for both a-Si:H and hydrogenated microcrystalline silicon, the absorption strength of the Si-H wag mode at 630 cm⁻¹ is independent of hydrogen content and of sample preparation. This makes using the Si-H wag intensity a good measure of the hydrogen concentration, which we do by

$$N_{630} = A_{630} I_{630}. \quad (2.2)$$

The results of hydrogen contents, $C_H = N_{630}/N_{Si}$, are listed in Table II.1. $N_{Si} = 5 \times 10^{22} \text{ cm}^{-3}$ is used. The difference is $\pm 5\%$ between the integrated absorption peak from 550 to 750 cm^{-1} and the integral of the Gaussian function. The hydrogen content, C_H , decreases monotonically by increasing either the hydrogen dilution ratio or the substrate temperature. We will show the detailed features of both the C_H and the stretch modes in correlation with crystallinity later in Fig.2.3.

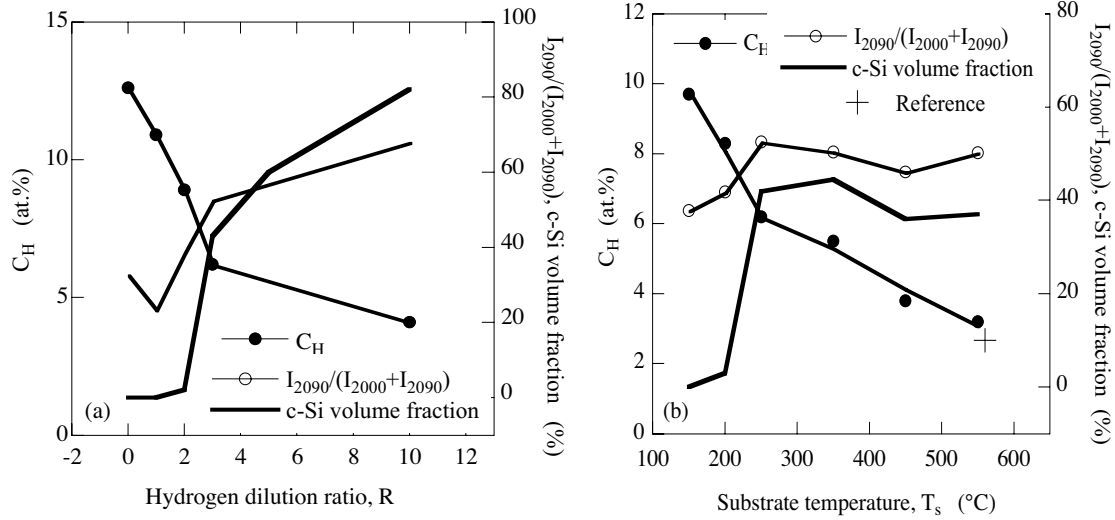


Fig. 2.3 The correlation of C_H (●) and the relative intensity of the 2090 cm^{-1} peak $I_{2090}/(I_{2000}+I_{2090})$ (○) with microcrystallinity for (a) group I and (b) group II films.

Two previous works [5,6] show that, in the $\mu\text{-Si:H}$ deposited by PE-CVD, the frequency of the IR wag mode shifted to 620 or 626 cm^{-1} ; and the absorption peaks are much narrower around 626 , 900 and 2101 cm^{-1} . They claimed that the absorption modes can be assigned to mono- and/or dihydride bonds on (100) and (111) surfaces in silicon crystallites. In these HW-CVD films, we have not found either the low frequency shift of the wag mode or a simple narrowing of the FWHM for $\mu\text{-Si}$ compared to a-Si:H. In Figs. 2.2(1a) and 2.2(2a) and Table II.2, one can see that the frequency of the SiH wag mode is located at 630 - 640 cm^{-1} regardless of whether the film structure is a-Si:H or $\mu\text{-Si:H}$. This wag-mode frequency is typical for standard a-Si:H. In group I films, as the crystallinity increases from 0 to $\sim 82\%$, the FWHM of the wag mode decreases from 89 to 68 cm^{-1} , whereas the FWHM of the 2000 cm^{-1} stretch mode increases from 86 to 113 cm^{-1} without a change of the FWHM in the 2090 cm^{-1} stretch mode. In group II films, the FWHM for both wag and stretch modes behaves the same, i.e. slightly decreases with an increase of crystallinity when $150 \text{ }^\circ\text{C} < T_s < 350 \text{ }^\circ\text{C}$, and rapidly decreases with an increase of the substrate temperature for $T_s > 350 \text{ }^\circ\text{C}$ without an increase of crystallinity. Hence, for the $R=3$ films, the main factor that accounts for the decrease in FWHM is the substrate temperature. If one only looks at one pair of the films deposited at high T_s with and without hydrogen dilution, such as H949 and H953, one may find the FWHM of both the wag mode and stretch mode decreased for the $\mu\text{-Si:H}$ film, H953. In general, we did not find a simple correlation between the FWHM and the crystallinity. However, we observed a clear correlation between the material's crystallinity and a frequency shift of both the bending and the stretch modes. One can see in Fig. 2.2(1b) and 2.2(2b) that the amplitude of the 850 - 895 cm^{-1} absorption is one order of magnitude weaker than the SiH wag mode absorption. As shown in the last column of Table II.2, the relevant hydrogen concentration of $N_{850,890}$ is $\leq 5\%$ of the total hydrogen for both group I and II films. In Fig. 2.2(1b) the 850 - 895 cm^{-1} absorption seems higher for the film with $R=10$. Indeed, it is also about

~5% of N_H after subtracting the contribution from SiO absorption. Notice, the last two rows in Table II.2, the $N_{850,890}/N_H$ is as low as 0.4% in the non-hydrogen-diluted reference film H949 but 5% in the hydrogen diluted film H953. It raises the questions of how hydrogen dilution can bring ten times more SiH_2 incorporation into the film at such a high substrate temperature, and consequently, whether the 850-890 cm^{-1} mode in hydrogen diluted films responds to SiH_2 or SiH at inner surfaces. Indeed, Itoh et al studied gas effusion compared to IR absorption and showed that the 850-890 cm^{-1} and 2100 cm^{-1} modes are both related to Si-H bonds in grain boundaries in hydrogen diluted PE-CVD μc -Si:H films. In these HW-CVD films, in addition to the doublet at 850-900 cm^{-1} , the SiO related modes at 750 and ~1000-1200 cm^{-1} appear when the c-Si volume fraction is above ~40% as shown in the curves with $R = 3$ and 10 in Fig. 2.2(1b) and with $T_s = 450^\circ C$ and $550^\circ C$ in Fig. 2.2(2b). The SiO absorption is largely enhanced for the film with a microcrystalline volume fraction of 82% (see Fig. 2.2(1b) $R=10$). This is because of the fast oxidation in air due to the porous-like structure. The porous-like structure, perhaps, is due to the high growth rate of c-Si grains and left the g.b. regions with much less mass density. Compared to PE-CVD a-Si:H, the HW films exhibit higher structural inhomogeneity and more percentage of clustered hydrogen. In the two-domain model, the mass density and the structural ordering of the high dense domain in a-Si:H are quite close to c-Si. It is reasonable that the structure becomes porous-like if the c-Si grains grow fast without plasma etching out the weak bonds. Finally, the stretch mode absorption is shown in Figs. 2.2(1c) and 2.2(2c). First, we calculate the hydrogen concentration from the stretch mode comparing it to that from the SiH wag mode absorption. We found that the hydrogen concentration, $N_{2000} + N_{2090}$, shows exactly the same two regimes of fast and slow decreases as shown in Figs. 2.3(a) and 2.3(b), and is about 5% less than that calculated from the SiH wag mode, N_{630} . This is within the accuracy of the technique. It implies that the SiH_2 component in these films is negligible if that stretch vibration mode contributes to the 2090 cm^{-1} absorption. One exception is the film with the highest c-Si volume fraction of 82%, in which the sum of $N_{2000} + N_{2090}$ is 15% larger than N_{630} . This could be due to the decrease of the stretch absorption strength in the porous like structure.

In order to find out how the hydrogen distribution changes with the crystallinity, both the hydrogen content and the relative integral intensity of $I_{2090}/(I_{2000}+I_{2090})$ are compared to the c-Si volume fraction. The results are shown in Figs. 2.3(a) and 2.3(b) for group I and II films. The dotted lines, the solid lines and the open circles represent the c-Si volume fraction, the hydrogen content and the $I_{2090}/(I_{2000}+I_{2090})$, respectively. At first, let us look at the solid lines that show the structural transition from a- to μc -Si as a function of R and T_s . One can see a rapid increase of the c-Si volume fraction at the threshold hydrogen dilution ratio $R=2$ in Fig. 2.3(a) and a threshold substrate temperature $T_s = 200^\circ C$ in Fig. 2.3(b). The curves in Fig. 3(a) indicate that the c-Si volume fraction can be as large as >80% at $R=10$. On the other hand, the saturated curve in Fig. 2.3(b) indicates that, at fixed $R=3$, the c-Si volume fraction reaches a maximum of $42\pm 1\%$ at $250 \leq T_s \leq 300^\circ C$, then slightly decreases to 33% at $350 \leq T_s \leq 550^\circ C$. In a previous work, Kroll et al observed a considerably enhanced hydrogen concentration in/near the a/ μc -Si transition zone in PE-CVD films. They suggested that it is due to molecular hydrogen trapped in microvoids. Such an enhanced C_H zone has not been found in these HW-CVD films. Instead, the hydrogen content, C_H , (see the solid dots in Fig. 2.3) decreases in two regimes of fast and slow in both group I and group II films. The turning points from the fast to slow regime are correlated with the onset of crystallinity. Based on the data from NMR and gas effusion for mixed-phase materials, most hydrogen clusters are located in the grain boundaries. When the material became μc -Si:H, the grain boundaries acted as a reservoir for hydrogen. This causes the slow decrease regime in total hydrogen content. Finally, the relative intensities of the 2090 cm^{-1} peak, $I_{2090}/(I_{2000}+I_{2090})$, are plotted as open circles in Figs. 2.3(a) and 2.3(b). The big cross in Fig. 2.3(b) represents the reference film that exists in the lowest $I_{2090}/(I_{2000}+I_{2090})=14\%$ that is equivalent to $N_{2090}/(N_{2000}+N_{2090}) = N_{2090}/(N_{630})=30\%$. It is a reasonable value for the clustered hydrogen in an a-Si:H film deposited at high substrate temperature of $560^\circ C$. The overall $I_{2090}/(I_{2000}+I_{2090})$ changes in the range of 23-68% in group I films and 37-50% in group II films. In other words, the percentage of the hydrogen concentration related to the 2090 cm^{-1} absorption, $N_{2090}/(N_{630})$, varies in the range of 42-83% and 60-71%. The clustered hydrogen deduced from NMR

experiments is in the same range. Interestingly, the changes of the ratio $I_{2090}/(I_{2000}+I_{2090})$ totally follow the manner of microcrystallinity for both group I and II films. The stretch mode doublet at 2000-2100 cm^{-1} has been attributed to either a difference in frequency of a SiH oscillator in SiH and SiH₂ bonding configurations or to a difference in the stretching frequency of SiH groups incorporated in the bulk material or located at internal surfaces. We examine what will be the case in these films as follows. First, we have examined whether there is any correlation of the 850-895 cm^{-1} peaks with the crystallinity. We found that the changes of the integrated intensity of 850-895 cm^{-1} peaks are not correlated to the materials crystallinity at all. Indeed, most of them change in an opposite way compared to the material's crystallinity. Therefore, the contribution from the SiH₂ stretch vibration to the enhancement of the 2090 cm^{-1} absorption is negligible.

We attribute the 2090 cm^{-1} absorption to the stretch vibration of clustered SiH in the g.b. regions. According to Eq. (2.1) we can write:

$$I_{2090}/(I_{2000}+I_{2090}) = N_{2090}/[(A_{2090}/A_{2000})N_{2000}+N_{2090}]. \quad (2.3)$$

The increase of $I_{2090}/(I_{2000}+I_{2090})$ could be caused by a decrease of the absorption strength, A_{2090} , and/or an increase of the relative concentration, N_{2090} . We could argue as follows: a) the absorption strength A is sensitive to the environment of the charged oscillators so that the less dense g.b. regions could result in a smaller A_{2090} . Hence, more g.b. volume fraction results in an increase of $I_{2090}/(I_{2000}+I_{2090})$. Recent observation of a much smaller A_{2000} in a high growth rate film supports this argument. b) Straightforward, the relative clustered SiH bond concentration, $N_{2090}/[N_{2000}+N_{2090}]$, is higher in the g.b. regions than that in the a-Si:H matrix. This is supported by the NMR, gas effusion results and the slow decrease regime of the C_H . Nevertheless, both the factors of a) and b) could contribute to the changes of $I_{2090}/(I_{2000}+I_{2090})$. The next question is whether the SiH bonds are sticking on the cone-shape c-Si grain surfaces or just clustered in the g.b. regions. The latter is more likely because there are 32% and 14% of $I_{2090}/(I_{2000}+I_{2090})$ in the a-Si:H films without c-Si grains (see sample H955 and H949 with $R=0$ in Table II.2), and the changes of the relative intensity, $I_{2090}/(I_{2000}+I_{2090})$, correlated with the g.b. volume fraction well (see Fig.2.3). In addition, the frequency range of 2085-2092 cm^{-1} (see Table II.2), is consistent with the SiH stretch frequencies of 2080-2098 cm^{-1} that were found in a-Si surfaces. So, we attribute the $\sim 2090 \text{ cm}^{-1}$ absorption to clustered SiH in the g.b. regions. This is in agreement with previous work.

2.3.3 Optical absorption spectra

TRS and optical absorption spectra at room temperature were used to study the optical constant and the density of electronic states. The measurements were carried out by light incident through the top surface of the film. The refraction index, n , was deduced from the TRS data in the long wavelength region between 1500 to 2000 nm. The Tauc optical gap was deduced from the absorption spectrum between 1.7 to 3.0 eV. The results are listed in Table II.1. We will not discuss them in detail but concentrate on the optical absorption spectra. The intrinsic absorption data on the high-energy side are deduced from TRS, whereas, CPM gives the low-energy absorption data where the penetration depth is large. Therefore, the absorption coefficient, α , is the average through the whole film. Figures 2.4(a) and 2.4(b) show the optical absorption spectra obtained by using CPM and fitted by TRS for group I and II films, respectively. The typical absorption spectrum of c-Si is plotted in Fig. 2.4(a) for reference. The absorption is contributed by the transitions from three components: the a-Si:H matrix, the c-Si grains and the grain boundaries. α at 1.4 eV is as small as $\approx 1 \text{ cm}^{-1}$ in a device-quality a-Si:H matrix. It is correlated to the bottom of the tail states of a-Si:H. The extra absorption coefficient at 1.4 eV shall represent the transition in c-Si grains and the g.b. We plot the absorption coefficient at 1.4 eV as a function of R , and T_s in Figs. 2.5(a) and 2.5(b) to extract the information of density of states (DOS) related to microcrystallinity.

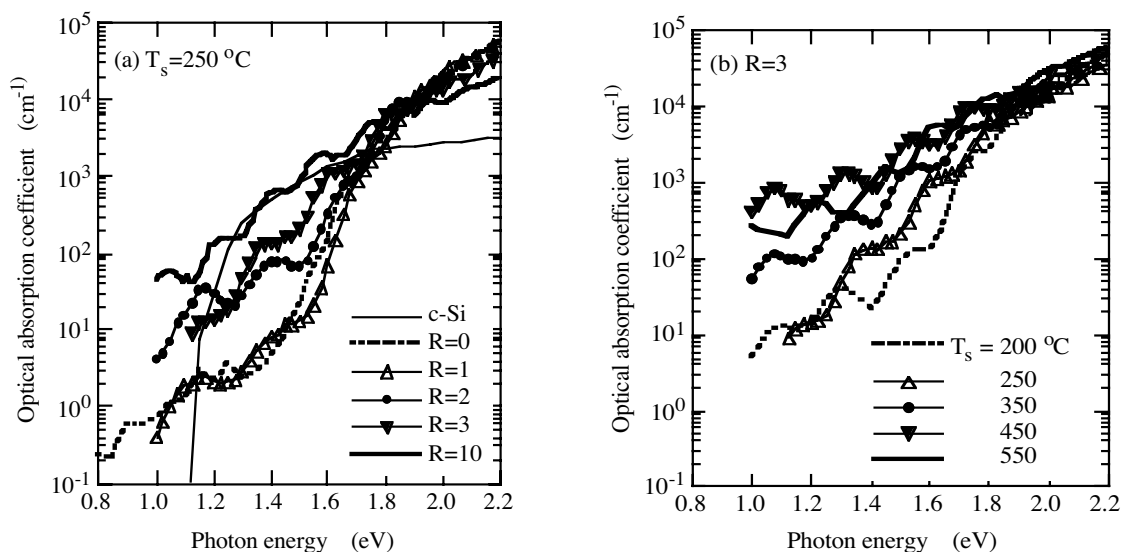


Fig. 2.4 Optical absorption spectra using CPM fitted by TRS for (a) group I and (b) group II films. The absorption spectra for c-Si is plotted in (a) for reference.

The dotted and the solid lines indicate the c-Si volume fractions and the absorption at 1.4 eV, respectively. For the first group of films shown in Fig. 2.5(a), the data of $\alpha(1.4 \text{ eV})$ in logarithmic plot and c-Si volume fraction are clearly correlated. When R increases, the density of electronic states related to $\alpha(1.4 \text{ eV})$ increases due to increase of crystallinity. Meanwhile, the increase of hydrogen dilution ratio at $T_s=250 \text{ }^\circ\text{C}$ does not obviously increase the defect DOS in the a-Si matrix. This will be seen in the relatively large radiative recombination efficiency in PL. For the second group of films, when $T_s > 250 \text{ }^\circ\text{C}$, the c-Si volume fraction does not increase but $\alpha(1.4 \text{ eV})$ does. This indicates an increase of both the tail states and the defect states in the a-Si matrix at high deposition temperature due to less hydrogen incorporation. This will be seen in the relatively low radiative recombination efficiency in PL, and the pinned Fermi energy position in the following sections.

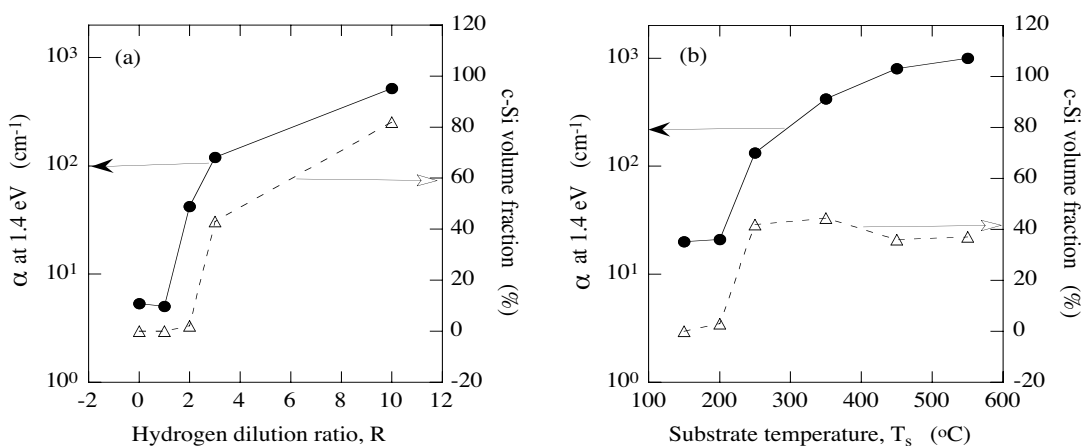


Fig. 2.5 the optical absorption coefficient at 1.4 eV (●) and the c-Si volume fraction (Δ) as a function of (a) R, and (b) T_s .

2.3.4 Conductivity activation energy

Dark-conductivity temperature dependence is also measured. The conductivity curves were obtained by cycling the temperature up and down. The thermally activated conductivity of $\sigma = \sigma_0 \exp(-E_a/kT)$ was obtained by using the decreasing-temperature conductivity curves. We obtain the value of the Conductivity activation energy, E_a , by an exponential fitting. Assuming electron conduction domination, the value of the activation energy indicates how much the position of the Fermi level, E_f , is below the conduction band edge. Figs. 6(a) and 6(b) show the E_a as a function of H-dilution ratio and substrate temperature for group I and II films. Again, the same thresholds of the decrease of E_a and the increase of microcrystallinity are shown in both groups of films. The detailed correlation between E_a and the material microcrystallinity is clearly shown in Fig. 2.6(a). As the material became more crystallized with an increase of R, the Fermi energy position moved up towards the conduction band edge. This implies that the energy position of the states at the g.b. regions is located at the upper part of the gap. On the other hand, in Fig. 2.6(b) when $T_s > 250$ °C, the E_a did not change much as T_s continually increased. This indicates that the defect states created by a high substrate temperature are located around the middle of the gap. Therefore, it does not change the position of Fermi level.

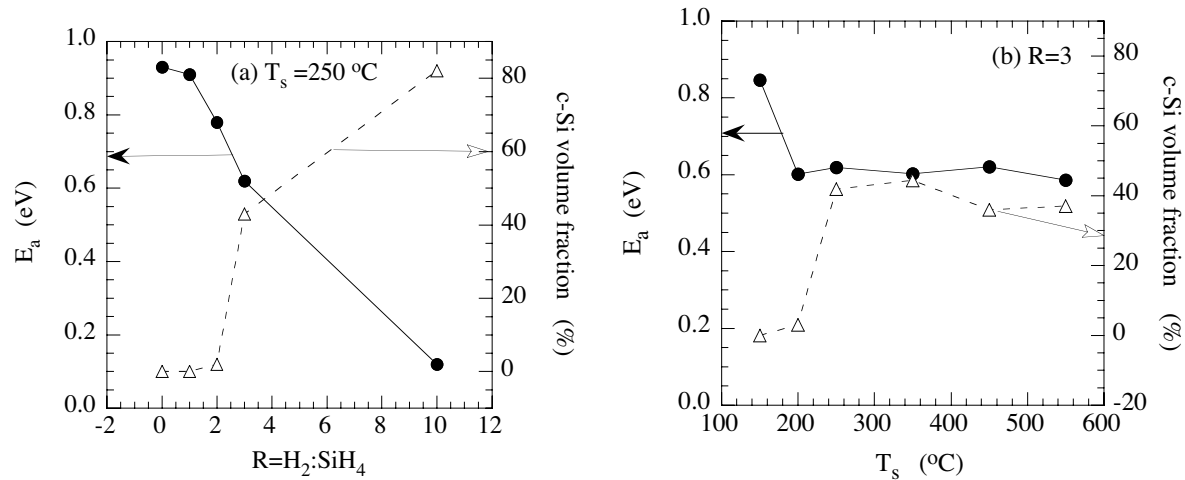


Fig. 2.6 Position of Fermi-level (●) and the c-Si volume fraction (Δ) as a function of (a) R, and (b) T_s .

2.3.5 PL spectra at 80 K

PL is another commonly used technique to study the DOS. In a-Si:H films, the PL signal at low temperatures originates from radiative band tail-to-band tail transitions. Hence, we obtain information about the electronic states including the optical gap, tail states and density of defects. A low energy band at ~ 1.0 eV has been observed in $\mu\text{c-Si}$ films. For these two groups of films and the reference film, the relative intensity of the PL spectra at 80 K is given in Figs. 2.7(a) and 2.7(b). The bottom dotted line in Fig. 2.7(a) represents the PL spectrum from the reference film. The intensity of the PL is 100 times larger for the films with $R=0, 1,$ and 2 films in Fig. 2.7(a) and 50 times larger for the films with $T_s = 150$ °C and 200 °C in Fig. 2.7(b). It means that the relative PL intensity is higher in group I films and lower in group II films. The PL intensity is especially low for the films with high $T_s = 450$ and 550 °C. This is due to the high density of non-radiative centers, in agreement with the optical absorption data in Figs. 2.5(b) and 2.6(b), whereas, more radiative centers exist at the g.b regions in the hydrogen diluted films. Comparing

the top curves in Fig. 2.7(a) and 2.7(b) for the two $\mu\text{c-Si}$ films, one can see the PL efficiency from the high hydrogen diluted $\mu\text{c-Si}$ is much higher than that from the high T_s $\mu\text{c-Si}$. For the reference film shown on the bottom curve in Fig. 2.7(a), the relative PL efficiency is as high as the a-Si:H film deposited at 250 °C except the peak energy is lower. This is consistent with the Raman data shown in Fig. 2.1(a) that HW film deposited at high T_s without hydrogen dilution is fully amorphous. It is clear that the PL features also indicate a sudden change from amorphous to microcrystalline at the same thresholds of R and T_s . One observes that the low energy PL from grain boundaries becomes dominant and the PL total intensity decreases as either R or T_s increases.

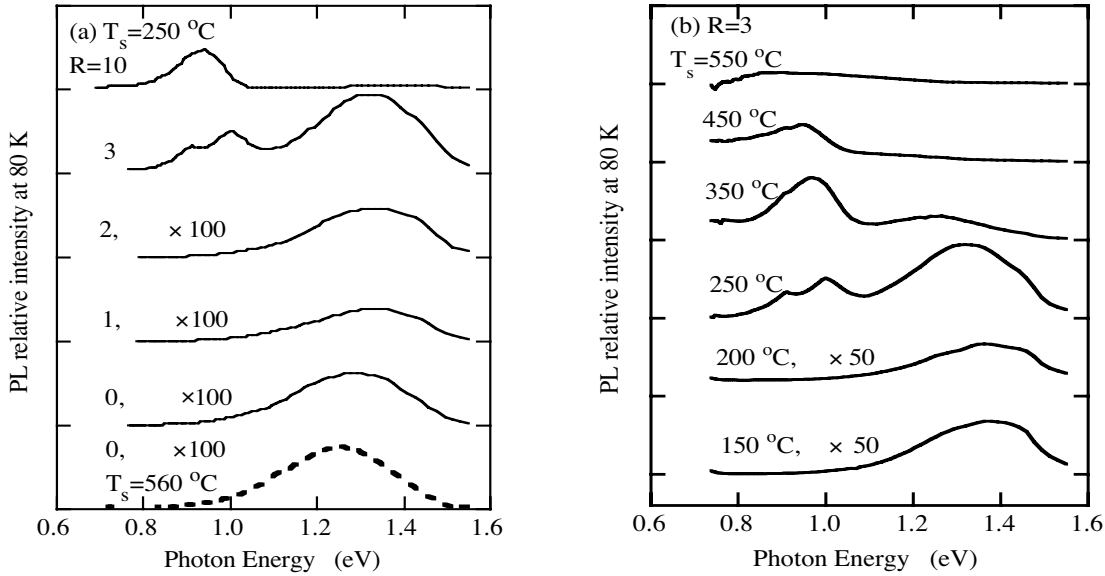


Fig. 2.7 Relative PL spectral intensity at 80 K for (a) group I and (b) group II films. The PL spectrum for the reference film is shown on the bottom of Fig. 1(a).

II.4. Summary

We studied the hydrogen incorporation and the optoelectronic properties in transition films from a- to $\mu\text{c-Si}$ made by hot-wire CVD as a function of hydrogen dilution of $0 < R < 10$ and substrate temperature of $150\text{ °C} < T_s < 550\text{ °C}$. The c-Si volume fraction, $X_c = (I_c + I_{gb}) / [I_c + I_{gb} + y(L)I_a]$, deduced from Raman spectra, is used to describe the degree of crystallinity. Raman results indicate that there is a threshold H-dilution ratio $R=2$ at $T_s = 250\text{ °C}$ and a threshold $T_s=200\text{ °C}$ at $R=3$ for the onset of the a- to $\mu\text{c-Si}$ transition. The maximum c-Si volume fraction 82% was found with $R=10$ at $T_s = 250\text{ °C}$. We found that the monohydride silicon bonding is the dominant configuration in both a-Si:H and $\mu\text{c-Si}$ films being studied. We have not found an enhanced hydrogen concentration in the a- to $\mu\text{c-Si:H}$ transition zone and the low frequency shift of the wag mode to 626 or 620 cm^{-1} , and there is no simple narrowing of the FWHM with increasing crystallinity as reported for PE-CVD films. However, we observed that both the hydrogen bonding distribution and optoelectronic properties are well correlated to the material's crystallinity. In summary:

- With an increase in either R or T_s , the hydrogen content, C_H , decreases in a fast and slow regime separated by the onset of microcrystallinity. We describe that this is due to the grain boundaries acting as a reservoir for hydrogen, which makes the decrease of total hydrogen content slow down with an increase of R and T_s .

- The relative absorption of the 2090 cm^{-1} peak, $I_{2090}/(I_{2000}+I_{2090})$, but not the 850-890 cm^{-1} peak, increases with c-Si volume fraction. Therefore, we attribute the 2090 cm^{-1} peak to the SiH stretch vibration from the clustered SiH in the grain boundary regions but not due to silicon dihydride. Meanwhile, the frequency of the wag mode remains unchanged at 630-640 cm^{-1} no matter whether the SiH oscillator is clustered or distributed.
- The density of electronic states was studied by optical absorption spectra. The position of the Fermi level was measured by the conductivity temperature dependence. The radiative states were studied by PL spectra at 80 K. The absorption coefficient at 1.4 eV, $\alpha(1.4 \text{ eV})$, is used to describe the DOS related to microcrystallinity. We found that the same threshold of the material's crystallinity is also visible in the increase of $\alpha(1.4 \text{ eV})$, in its relevant PL(1.0 eV) band, and in the position of E_f . We explain that the increase of crystallinity results in an increase of the low energy electronic density of states including radiative and non-radiative centers. The low energy PL peak at $\sim 1.0 \text{ eV}$ originates from the radiative centers in the g.b. regions. More defects were created in the a-Si matrix when $T_s > 250 \text{ }^\circ\text{C}$. So, the Fermi level position is pinned at the middle of the gap in films deposited at $R=3$ and $T_s > 250 \text{ }^\circ\text{C}$.

We have shown both the features of the hydrogen incorporation and the electronic density of states are well correlated to the crystalline threshold and the changes of the c-Si volume fraction. We attribute the above features mainly related to the g.b. regions. The arguments are as follows. The hydrogen content is low in the tetrahedron c-Si lattice. The increase of c-Si grains would result in a decrease of the total hydrogen content, but does not explain the two regime of the C_H decrease. Furthermore, in response to the 2090 cm^{-1} absorption, the SiH bonds are not sticking on the cone-shape c-Si grain surfaces but just clustered in the g.b. regions as we have discussed in section III.2. In crystalline silicon, on the other hand, the electronic gap states are low, and the PL efficiency is limited by momentum conservation. Hence, the low energy luminescence centers can only be in the g.b. regions. The most defect states in $\mu\text{c-Si}$ phase are also in the g.b. regions and/or in the a-Si:H matrix for the high T_s films. Therefore, we attribute the above a) b) and c) observations mainly to the formation of the c-Si grain boundaries during microcrystallization.

II.5. Conclusions:

We conclude that making $\mu\text{c-Si}$ films by the HW-CVD technique can result in a high growth rate with relatively low hydrogen dilution ratio. Controlling hydrogen dilution is the key factor to depositing device-quality $\mu\text{c-Si:H}$ films. Deposition at $T_s \sim 250 \text{ }^\circ\text{C}$ with varied R produces the films with either the lowest defect density or the highest volume fraction of crystallinity. However, the high density of microvoids in the high-growth rate films cannot be detected by Raman spectra. The porous-like structure in the highly microcrystallized films causes the oxidation problem that can be solved.

III. D° May Not Be The Dominant Recombination Centers For PC In Hot-Wire a-Si:H [7]

III.1 Introduction

A fundamental problem of a-Si:H is the light-induced metastable defect creation. The original Staebler-Wronski paper describes that long exposure to light decreases both photoconductivity (σ_{PC}) and dark conductivity (σ_{d}) in a-Si:H prepared by PE-CVD. Interestingly, the σ_{PC} shows a relatively stable value and the σ_{d} increases upon light soaking in a-Si:H films prepared by HW-CVD. However, it was found that the density of metastable defects is in the same order of $10^{16}/\text{cm}^3$ in both PE and HW films. As we have known, the typical intrinsic a-Si:H is slightly n-type and the Fermi level lies above the middle of the gap and the neutral silicon dangling bonds, (D°), act as the non-radiative recombination centers. Generally, the electron lifetime, τ , is in reverse proportion to the density of D° . The σ_{d} activation energy,

$E_a(A)$, is ~ 0.7 eV at the annealed state and increased to $E_a(B) \sim 0.75$ eV at the light-soaked state due to metastable D^0 creation near the middle of the gap. In order to understand the anomalous photo-induced changes of σ_{pc} and σ_d in intrinsic device-quality a-Si:H deposited by HW-CVD, we first explore the properties of the recombination centers by measuring thermostimulated conductivity (σ_{TSC}).

In intrinsic a-Si:H, electron mobility is much greater than hole mobility. Using an Ohmic contact, the measured conductivity is attributed to electron's motion. σ_{TSC} spectrum and temperature dependence of σ_{pc} have been used to explore the properties of deep states in a-Si:H. Based on the multiple-trapping model, Fritzsche et al found that σ_{TSC} can be written as

$$\sigma_{TSC} = e\mu\tau g(E)f(E)1.2\beta |E|/T, \quad (3.1)$$

where $\mu\tau$ is the mobility-lifetime product, $g(E)$ is the density of gap states, and β is the heating rate. They analyzed that the general shape of σ_{TSC} in a-Si:H based materials contains three regimes from ~ 120 K to ~ 400 K: (I) an initial rise, σ_{TSC} depends on the heating rate and the Boltzmann tail of the carrier distribution function just before the onset of heating, $f_o(E)$; (II) a steady-state regime, the distribution function $f(E)$ is near constant and σ_{TSC} reflects $\mu\tau g(E)$; and (III) an end of σ_{TSC} that drops to zero when all carriers come to thermal equilibrium. Temperature dependence of $\mu\tau(T)$ can be obtained from σ_{pc} temperature dependence measurements as

$$\sigma_{pc}(T) = e\mu\tau(T)G, \quad (3.2)$$

where G is the electron-hole pair generation rate. During the heating processes in both the σ_{TSC} and $\sigma_{pc}(T)$ measurements, the change of the carrier distribution function, $f(E)$, can be described by quasi-Fermi level,

$$E_{qn}(T) = kT \ln(n/N_c), \quad (3.3)$$

where n is the density of mobile carriers and N_c is the density of states at the mobility edge. On the other hand, the carrier distribution function just before the onset of heating, $f_o(E)$ can be described by a demarcation energy E_d that separates the thermalized and frozen-in states,

$$E_d = -kT \ln(\nu_0 t), \quad (3.4)$$

where $\nu_0 \cong 10^{12} \text{ s}^{-1}$, and $t = t_0$ is the long-delay time in σ_{TSC} experiments. Hence, the position of E_d is nearly fixed but the position of quasi-Fermi energy $E_{qn}(T)$ changes with T during the heating process. In σ_{TSC} measurements the carrier thermal emission rate dn/dt is balanced by the recombination rate $b_r = n/\tau$ and the distribution function $f(E)$. Generally, there are two cases of non-equilibrium carrier distribution: (a) For strong recombination as shown in Fig. 3.1(a), the recombination rate b_r is larger than the trapping rate, $b_r > b_t$. The quasi-Fermi level E_{qn} is always below the demarcation energy E_d and the carrier distribution function $f(E)$ has a sudden jump at E_d by the reduction of mobile carrier density, n , due to strong recombination. (b) For weak recombination as shown in Fig. 3.1(b), $b_r < b_t$. At low temperatures E_{qn} is above E_d and slowly moves down as the temperature increases finally to $E_{qn} = E_d$. The carrier distribution function $f(E)$ has no sudden jump in the transition zone. In the case of strong recombination, the theory predicts that there is a sudden rise near the transition from the initial rise to the steady-state regime. However, this case has never been observed in any a-Si:H-based films. Hence, the commonly recognized recombination centers, D^0 , are sort of weak recombination centers with $b_r < b_t$.

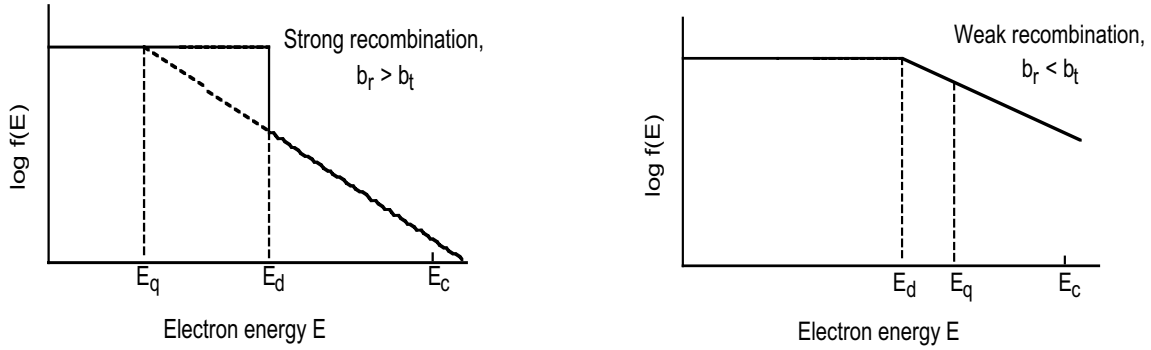


Fig. 3.1 Distribution function (a) for strong recombination and (b) for weak recombination relative to re-trapping. E_d is the thermalization demarcation energy, E_q is the quasi-Fermi level and E_c is the electron mobility edge.

On the other hand, the commonly used techniques to measure the density of defects in a-Si:H are electron spin resonance (ESR) and the CPM. ESR measures the density of neutral dangling bonds D^0 and CPM takes into account all the electron transitions from gap states to conduction band edge. Whereas, a large discrepancy between the defect densities was found by a comparative study of ESR and the CPM in a-Si:H films. For the initial state, the main cause of the difference in undoped a-Si:H was found to be the presence of the thin near-surface layer with a high density of DBs blind to CPM and the presence of negatively charged DBs inactive to ESR; for the light-soaked state, the inhomogeneous distribution of photocreated DBs caused by the penetration depth of the light being less than the film thickness could be the main contribution [8,9]. We studied the recombination centers by ESR/CPM in both HW- and PE-CVD a-Si:H films.

III.2. Sample and Experimental

Table III.1. Sample preparation conditions

Sample ID	Growth method	Subs. T T_s ($^{\circ}\text{C}$)	Filt.current (A)	Reaction gas	Thickness (μm)	Supplier	Measurements
T773	HW	360	16	SiH_4	1.1	NREL	TSC, E_a
T779	HW	360	15	SiH_4	0.45	NREL	TSC, E_a
T837	HW	400	15	SiH_4	1.2	NREL	TSC, E_a
A7119	dc-PE	200		SiH_4	3.0	BP-SLX	TSC, E_a
11961	rf-PE	~ 200		Si_2H_6 low H-dilut.	0.5	USSC	TSC, E_a
H954	HW	150	16	SiH_4	0.7	NREL	ESR/CPM
H955	HW	250	16	SiH_4	0.8	NREL	ESR/CPM
PE#1	rf-PE	250-300		SiH_4	0.8	Kanazawa Univ.	ESR/CPM

Device-quality intrinsic a-Si:H films were prepared by HW-CVD at the National Renewable Energy Lab (NREL) and by PE-CVD at BPSolarex, United Solar Ovonic Corporation (USOC) and Kanazawa University. The film deposition conditions are listed in Table III.1. T773, T779, T873, A7119, and 11961 were deposited on Corning glass for $\sigma_{PC}(T)$, \square_{TSC} and $\sigma_d(T)$ studies. H954 and H955 and PE#1 were deposited on quartz substrates for ESR/CPM studies. The HW films of H954 and H955 were using a separated deposition system and deposited at a relatively low temperature compared to T773, T779 and T873. Their σ_{PC} were not as stable as those deposited at high temperatures, but they still were more stable than PECVD films and their initial activation energy was large. In σ_{TSC} and conductivity studies, the MMR micro-probe system with vacuum 10^{-4} Torr was used to mount the sample. The σ_{PC} was generated by a 632.8 nm laser at a rate of $G = 5 \times 10^{15}$ photons/cm³s¹ and its temperature dependence was measured from 80 K to 400 K. In the σ_{TSC} study the sample was first cooled down to 120 K and then exposed to the 632.8 nm laser light with an exposure time $t_e = 60$ sec. After a delay time, $t_o = 30$ min σ_{TSC} was measured in a step-heating process with a constant heating rate $\beta = 1.5$ K/min in the dark. Ohmic contact and a low field of 10^3 V/cm were used to avoid electrode effects. A Keithley 6512 programmable electrometer was used to record the current. A LabView program was used for experimental control and data acquisition. Light soaking was performed *in situ*. The sample temperature was kept at 35 °C during light soaking. State A was reached after the sample was annealed in a vacuum for one hour at 160 °C; state B was reached by a 200 mW/cm² white light illumination through a water filter of 4 hours. The details of ESR/CPM measurements can be found elsewhere [8,9].

III.3. Results

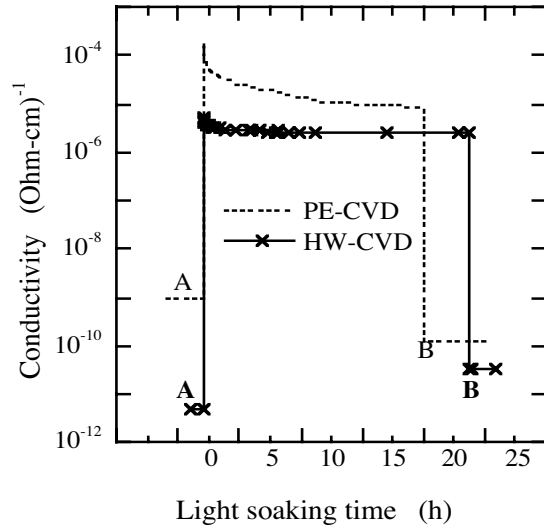


Fig. 3.2 The conductivities before, during and after light soaking for typical intrinsic a-Si:H films made by HW-CVD (solid line) and PE-CVD (dotted line).

Figure 3.2 shows the typical photo-degradation of σ_{PC} and σ_d for device quality intrinsic PE-CVD a-Si:H film deposited at 200 °C and HW-CVD film deposited at 320 °C < T_s < 440 °C. The dotted line represents the light-soaking effect for PE-CVD film that shows a decrease of both σ_{PC} and σ_d . Compared to the PE-CVD film, one finds the better stability of σ_{PC} and the increase of σ_d upon light soaking for the HW film. To explain the anomalous situation for the HW-CVD films, we explore the nature of the defects as follows.

3.3.1 Natural degradation effect

The Fermi-level position is deduced from $\sigma_d = \sigma_{o0} \exp(-E_a/kT)$. We mounted the film on a thermal stage in a vacuum and kept it at 120 °C for 30 min to cleanup the film surface adsorption, then we took the conductivity data from a temperature cycle of 270 K to 420 K to deduce the activation energy at the initial state. However, the value of E_a was driven down with the storage time or a temperature cycle without light soaking. For example, we observed $E_a(I) \sim 0.98$ eV and $E_a(I) \sim 0.89$ eV after being stored in the dark

for several weeks for the film T773; and $E_a(I) \sim 1.05$ eV and $E_a(A) \sim 0.98$ eV after annealing at 160 °C for 1 h for sample T779. We named this "natural degradation" effect because of the similarity to the photo-degradation effect in conductivities. The values of $E_a(I)$, and of $E_a(A)$ and $E_a(B)$ measured before and during the time period of σ_{TSC} studies are listed in Table II. One finds that the activation energy E_a increased from 0.73 to 0.77 eV for the non-hydrogen diluted PE-CVD film #7119. Whereas, all the HW-CVD and the hydrogen-diluted PE-CVD samples show the opposite direction, i.e. the E_a decreased after light soaking.

Table III.2. Conductivity activation energies at initial- annealed- and light soaked states.

Sample ID	11961	A7119	H954	H955	T773	T779	T837
$E_a(I)$ (eV)	-	-	0.86	0.95	0.98	1.05	0.96
$E_a(A)$ (eV)	0.92	0.73	0.84	0.93	0.89	0.93	0.86
$E_a(B)$ (eV)	0.85	0.77	0.81	0.85	0.84	0.86	0.82

3.3.2 *Strong recombination center in a-Si:H prepared by HW-CVD*

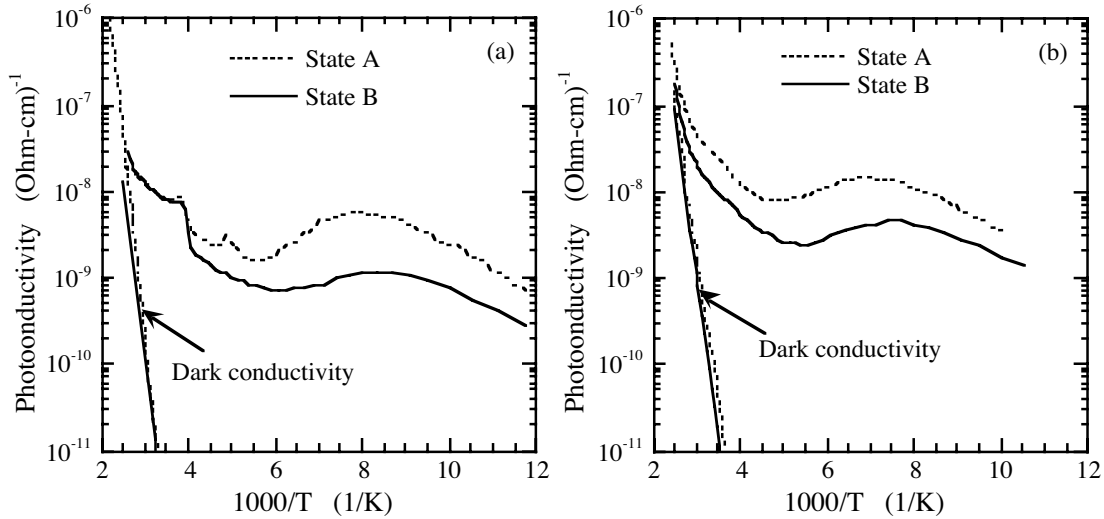


Fig. 3.3 Temperature dependence of photo- and dark conductivity before and after 200 mW/cm² white light soaking for 4 h, (a) for HW-CVD film T779 and (b) for PE-CVD film A7119.

Fig. 3.3 shows both the $\sigma_d(T)$ and the $\sigma_{PC}(T)$ curves for typical device-quality (a) HW sample T779 and (b) PE-CVD a-Si:H sample A7119. The thermal quench valley in all the $\sigma_d(T)$ curves, perhaps, resulted from the trapped holes in the valence band tail. The additional convex peaks at ~ 200 K and ~ 255 K in Fig. 3.3(a) are correlated to the σ_{TSC} peaks in Fig. 3.4(a). Figs. 3.4(a) and 3.4(b) show the σ_{TSC} curves for these same samples of T779 and A7119 at States A and B. We are not going to analyze the σ_{TSC} spectra in detail but only pay attention to the transition near 200 K. Comparing Fig. 3.4(a) with 3.4(b) the most interesting feature is that a sudden rise occurs in the σ_{TSC} near the transition from the initial rise to the steady-state regime in the HW film at both States A and B as shown in Fig. 3.4(a). According to Fritzsche's theory, this is an evidence of strong recombination centers in the HW a-Si:H film at both States A and B. It means that the recombination rate for electrons, b_r is larger than the trapping rate, $b_t > b_r$. D^+ that has a larger capture rate for electrons than D^0 can be the candidate of the strong electron recombination center. A sudden rise in the σ_{TSC} near 200 K has also been observed in the other HW films of T837 and T773; whereas, a smooth transition of σ_{TSC} similar to that in A7119 was observed in PE-CVD

film 11961. Hence the sudden rise feature is the characteristic for the HW-CVD a-Si:H deposited at high substrate temperatures.

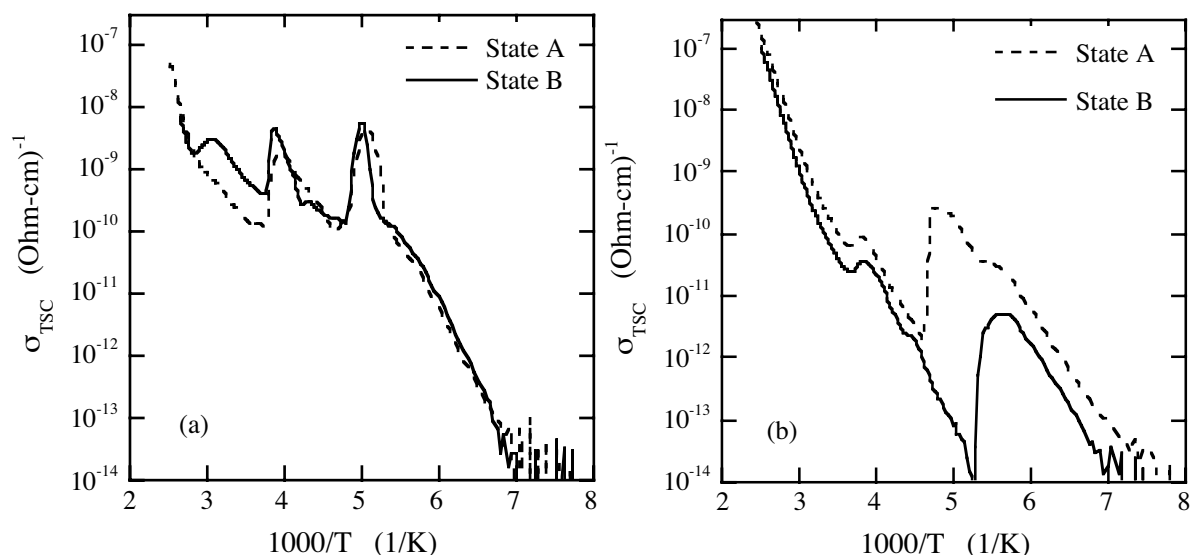


Fig. 3.4 Thermostimulated conductivity for the same samples in Fig. 3 at annealed State A and light-soaked State B, (a) for HW-CVD film T779 and (b) for PE-CVD film A7119.

3.3.3 ESR and CPM studies

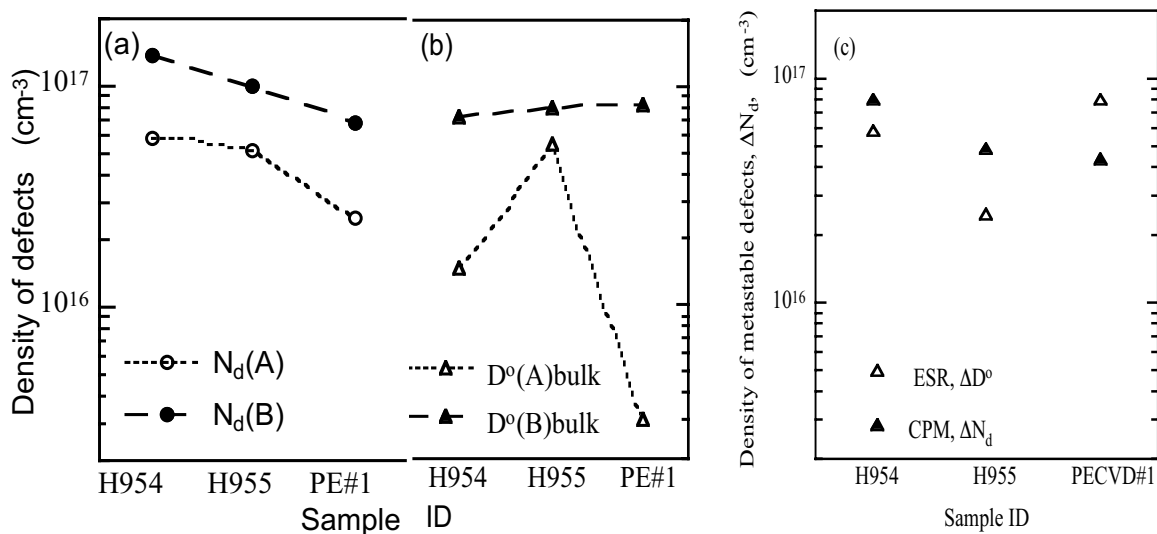


Fig. 3.5 Total density of defects for HW- and PE-CVD films before and after 200 mW/cm² white light soaking for 30 h. measured by (a) CPM, (b) ESR, and (c) light-induced metastable defects measured by CPM and ESR, respectively.

We have measured the density of defect states by ESR and CPM on two HW-CVD films deposited at substrate temperatures of 150 and 250 °C in comparison to the PE-CVD film. Figs. 3.5(a) and 3.5(b)

show the CPM and ESR results at State A and State B (that was reached by light soaking using a 200 mW/cm² white light for 30 h). For the ESR data, only the bulk defect density was counted by assuming that the densities of the surface defect are the same for all the films based on the previous experimental results. Regardless of the absolute values, the light soaking results in an increase of defect density from 3 to 9x10¹⁶/cm³ for all the films. The CPM data show a parallel increase of N_d, but the ESR data show a much larger increase of D⁰ in the PECVD film than in the HW films. We plot the density of light-induced metastable defects, $\Delta N_d = N_d(B) - N_d(A)$ and $\Delta D^0 = D^0(B) - D^0(A)$, in Fig. 5(c). The interesting thing is that in the HW films the ΔN_d deduced from CPM is larger than ΔD^0 ; but in the PECVD film the ΔN_d is smaller than ΔD^0 . The latter is commonly observed in PE-CVD film. Reasonably assuming the same inhomogeneous distribution of photocreated DBs in all the films after the same light soaking processes, the different results between HW- and PE-CVD films can be explained by the opposite direction movement of the Fermi-level upon light soaking; i.e. after light soaking the Fermi-level moved upwards in the HW films which left more negative charged defects, D⁻, that are inactive to ESR. In the PE-CVD film, after light soaking the Fermi-level moved downwards, which results in more D⁰. This means less metastable electron recombination centers, D⁰, hence less light induced σ_{PC} degradation in HW films than that in PECVD film. But, there are more metastable defects in their negative charged state in HW films.

III. 4. Summary and Discussion

3. 4.1 Summary

In HW-CVD a-Si:H films deposited at substrate temperature at 320 °C < T_s < 440 °C, we have observed a relatively stable photoconductivity and upward movement of the Fermi-level after light-soaking. The unusual photo-degradation curve for HW-CVD films in Fig. 3.3 can be explained by either a) or b) as follows. a) The upward movement of the Fermi-level position: Assume D⁰ is the dominant recombination center and the electron lifetime is in a reverse proportion to the density of D⁰. The creation of metastable DBs could be balanced by the upward movement of the Fermi-level, which results in filling up partial D⁰ into D⁻. Therefore, the total number of D⁰ and then the electron lifetime could change much less than the case of the Fermi-level moving downward. The CPM/ESR results in Fig. 5 support these arguments. b) The existence of stronger electron recombination centers such as positive charged defects, D⁺. We have shown evidence of strong recombination centers for electrons by thermal stimulated current measurements. If the D⁺ rather than D⁰ act as dominant non-radiative recombination centers at both States A and B, the σ_{PC} should be relatively stable upon light-induced D⁰ creation. As one knows, the capture rate of D⁺ for electrons is much greater than that of D⁰. A density of 10¹⁵/cm³ of the D⁺ among total defects of 10¹⁶/cm³ would dominate the electron lifetime. Obviously, an increase of metastable D⁰ on the order of 10¹⁶/cm³ cannot change the electron lifetime much. One cannot exclude that both a) and b) could play a role in the unusual photo-degradation curve for HW-CVD films.

The comparative ESR/CPM studies show the light-induced metastable defects in the order of 10¹⁶/cm³ for both the HW and PE-CVD a-Si:H. The density of defects in the HW films is higher than the PE-CVD film in State A, but the change of the density of neutral dangling bonds, ΔD^0 , with light soaking is smaller in the HW films than the PECVD film. Whereas, the ΔN_d deduced from sub gap absorption is larger than ΔD^0 in the HW films; the ΔN_d is commonly smaller than ΔD^0 in PECVD film. We explained this by the opposite direction movement of the Fermi-level in HW- and PE-CVD films upon light soaking. It is a blemish of this work that we do not have films T773, T779 and T837 deposited on ESR quartz substrates to measure ESR.

3. 4.2 Natural degradation effect

We have observed a natural degradation effect, i.e. the activation energy is driven down with storage time and/or temperature cycle without light soaking. In other words, the Fermi level position moved upward with prolonged storage time. This movement results in an increase of the dark conductivity, an increase of the electron mobility-lifetime product, $\mu_n\tau_n$, and a decrease of the hole mobility-lifetime product, $\mu_p\tau_p$, in other words, a decrease of the charge collection length that is crucial for a-Si:H solar cell performance. Therefore, a natural degradation of the a-Si:H solar cells made by HW-CVD can be understood. One may wonder if this degradation was caused by oxidation. This can be distinguished experimentally by storing the sample either in high vacuum or oxygen environment. Results indicate that it was not the oxidation effect, at least, for the films studied in this work.

3.4.3 Why the activation energy is very large and driven down?

How can the activation energy, E_a , be as large as ~ 1.0 eV in a ~ 1.7 eV optical gap material? Why is it driven down with storage time, temperature cycle and light soaking? We try to understand these by an over simplified picture. If there is only the silicon-dangling bond as the defect, one possible explanation for the large E_a is a large deformation potential in the HW-CVD films. The thermal excitation energy of an electron consists of two terms:

$$E_a = E_T + W = E_T + B^2/4A, \quad (3.5)$$

where E_T is the energy of the defect state below the bottom of the conduction band, E_c , W is the lattice relaxation energy at the defect, B is the deformation potential representing the strength of the electron-phonon interaction, and A is the strength of the network vibrations. If W could be as large as ~ 0.3 eV, one could obtain a value of $E_a \sim 1.0$ eV for a defect located 0.7 eV below E_c . However, the assumed lattice relaxation energy may be too large. The lattice relaxation energy at the defect, W , was found not to be larger than 0.1 eV in n-type PE-CVD a-Si:H. It is possible that U has a distribution of values so that a small fraction of defects may have negative U ,

$$U = e^2/4\pi\epsilon\epsilon_0 r - W < 0, \quad (3.6)$$

where $e^2/4\pi\epsilon\epsilon_0 r$ is the Coulomb interaction energy. A higher probability of negative U defects exists in HW film since there is larger lattice relaxation energy than that in PE-CVD film. Whereas, the majority of defects must be positive U defects with ESR signal and unpinned Fermi level. The negative U defects result in the same number of D^- and D^+ . That small number of D^+ could be the strong recombination centers for electrons and the D^- located in the deep of the gap could result in a large E_a . Alternatively, if modeling the disorder as potential fluctuations and the potential fluctuations exceed U ; this permits coexistence of D^0 , D^- and D^+ without negative U , whereas, the large value of the initial E_a can't be explained.

Besides, the strong electron-phonon interaction in HW films shall result in a larger energy difference between the absorption and emission in optical transitions. This was evidently shown in a lower PL peak energy in HW films than that in PE-CVD films; consequently, the value of V_{oc} is lower. Finally, the external factors of storage time, temperature cycle and light soaking may result in a decrease of W , consequently E_a is driven down. Finally, the defect-complex caused by the contamination by the hot filament is not excluded as a candidate of the strong recombination center for electrons. It needs to be studied.

III.5 Conclusions

The features of light soaking effects in a-Si:H prepared by HW-CVD are different from those in PE-CVD films: the PC decreases only slightly and the dark conductivity increases. We explore the properties of the recombination centers using ESR, CPM and σ_{TSC} . We observed a sudden rise of σ_{TSC} near the transition from the initial rise to the steady-state regime of σ_{TSC} . This is an evidence of strong-recombination. When the strong recombination centers such as D^+ rather than D^0 dominate the electron lifetime, the PC would show a relatively stable value.

IV. PL study of growth rate dependence on solar cells made by BPSolar[10,11]

IV.1. A special microstructure of high growth rate films

a-Si:H intrinsic films and their solar cells were prepared using DC-PECVD with growth rates of 1, 3, and 10 Å/s by BPSolar. Fig. 4.1 (Raman shift) shows an identical TO mode for all the samples, which indicates the local silicon-bonding configuration does not change with the growth rate from 1 to 10 Å/s. IR results show that the hydrogen bonding configuration is monohydride (Si-H) dominated, and the hydrogen content obtained from the 630 cm^{-1} wagging mode is 12-14 at.%. Surprisingly, a very small absorption strength for the stretching 2000-2100 cm^{-1} mode was found for the samples deposited at the higher growth rates (3, 10 Å/s). For these same samples, the PL spectra exhibit a red shift. Both the IR and PL results might be related with the same microstructures formed at high growth rates. However, the cell performances were comparable. The i-layer thickness, optical gaps and the solar cell performance are listed in Table IV.1.

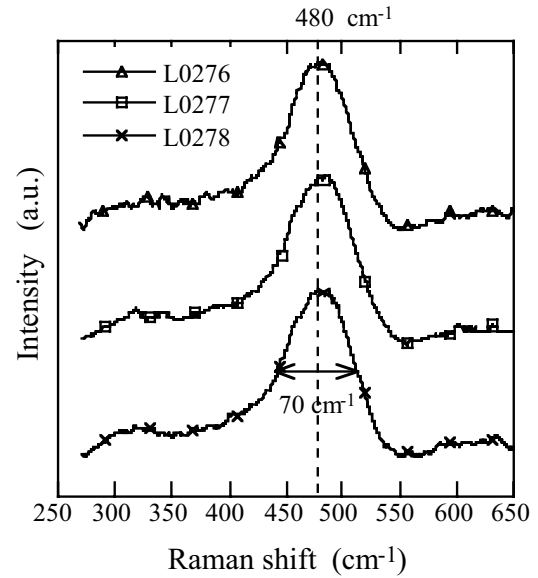


Fig. 4.1 Raman shift for samples with growth rates of 1, 3 and 10 Å/s.

Table IV.1. Sample preparation conditions, i-layer properties and their solar cell performances.

Sample	Growth rate (Å/s)	Thickness (Å)	Optical gap (eV)	FF	V_{oc} (V)	J_{sc} (mA/cm)	Eff. (%)
*L171-2C	1	~2500		0.731	0.895	11.64	7.62
*L172-5C	3	~2500		0.721	0.908	11.68	7.65
L1221-2IR	10	~2500		0.717	0.890	11.51	7.34
*L0172-3	1	~6000					
*L0172-4	3	~6000					
*L0173-1	5	~6000					
L0276-1,1c	1	~6000	1.711				
L0277-1,1c	3	~6000	1.721				
L0278-1,1c	10	~6000	1.715				

* These samples were deposited using a discontinued deposition-chamber configuration

4.1.1 A special case of the IR spectra:

The IR spectra are shown in Fig. 4.2 for the samples (a) L0172-3, L0172-4 and L0173-1, and (b) L0276-1c, L0277-1c and L0278-1c. The absorption at $\sim 630\text{ cm}^{-1}$ was used to calculate C_H using $A_{630}=2.1\times 10^{19}\text{ cm}^{-2}$. $C_H=12-14\text{ at.}\%$ was found and listed in Table IV.2. Interestingly however, the stretch modes were

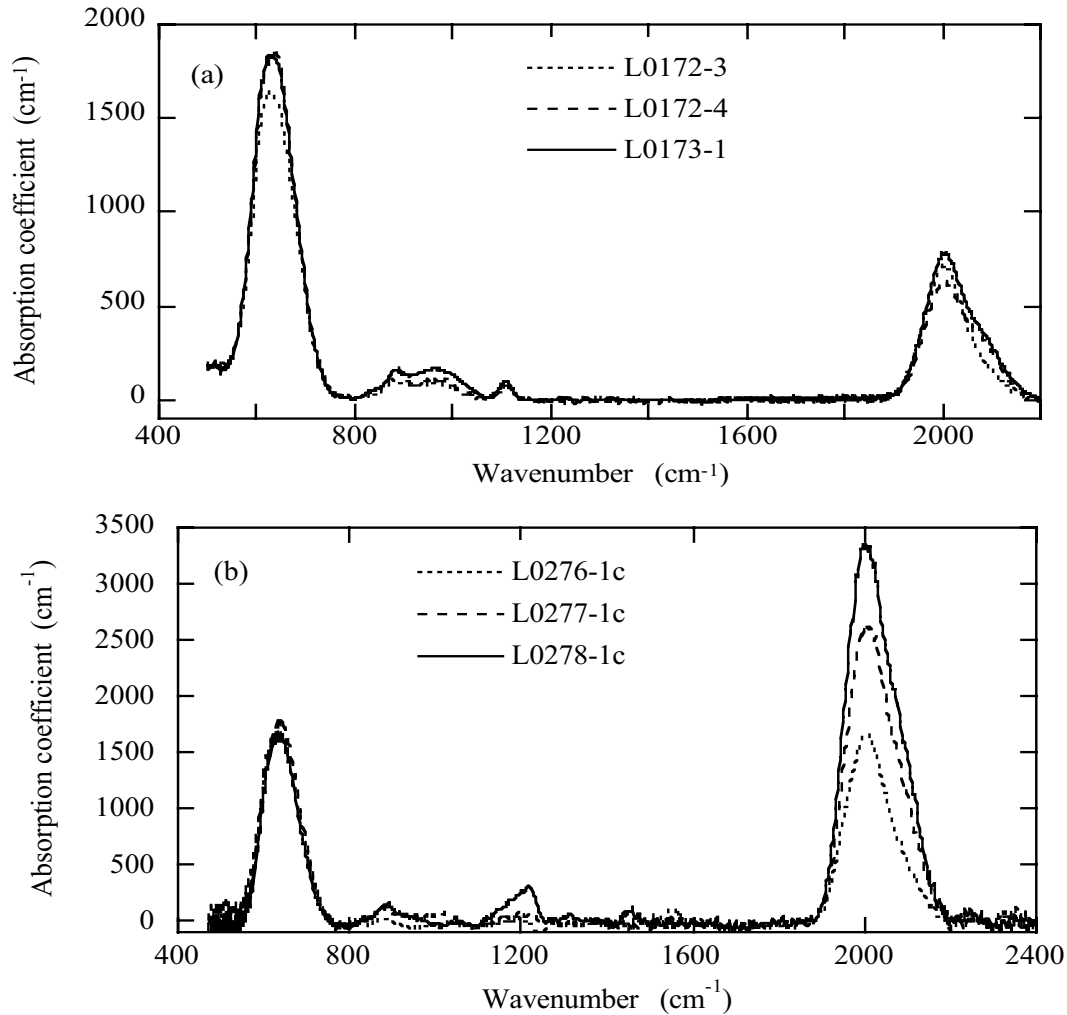


Fig. 4.2 IR spectra for samples of (a) L0172-3, L0172-4, L0173-1, (b) L0276-1c, L0277-1c, and L0278-1c.

unusual in the second group of films as shown in Fig. 4.2(b). The larger $2000-2100\text{ cm}^{-1}$ absorption band indicates the absorption strength for the stretching mode becomes much smaller than previous results. One can see that the stretching absorption increases incrementally when the growth rate increases from 1 to 10 \AA/s . The values of $(I_{2000}+I_{2090})/I_{630}$, $\alpha=(I_{2000}/I_{630})$, and $\beta= I_{2000}/I_{2090}$ are listed in Table IV.2. The results are from the second measurements after one year. One can see that the ratio of $(I_{2000}+I_{2090})/I_{630}$, somewhat is normal for the first group of films L0172-3, L0172-4, and L0173-1 with growth rates of 1, 3 and 5 \AA/s . Whereas, the value of α for the second group of films is much larger. Especially, for the films with growth rate $\geq 3\text{ \AA/s}$ the α values are about a factor of 3-4 larger than previous results. The values of β are also larger than previous results. One possible explanation for the large α and β is that a large

fraction of the Si-H bonds are located at/near some microstructures as clustered monohydrides in the films. The samples were retained in the lab at room temperature for a year and the IR spectra were re-measured twice. The unusually large stretch modes were confirmed.

Table IV.2. Hydrogen content and the absorption strengths of Si-H vibration modes

Sample ID	C _H (at.%)	N _H (10 ²¹ cm ⁻³)	I ₆₃₀ (cm ⁻¹)	I ₂₀₀₀ (cm ⁻¹)	I ₂₀₉₀ (cm ⁻¹)	(I ₂₀₀₀ +I ₂₀₉₀)/I ₆₃₀	α=I ₂₀₀₀ /I ₆₃₀ =A ₆₃₀ /A ₂₀₀₀	β=I ₂₀₀₀ /I ₂₀₉₀ =A ₂₀₉₀ /A ₂₀₀₀
*L0172-3	12.7	6.4	302	36.2	5.1	0.15	0.13	7.1
*L0172-4	14	7.0	333	31.2	10.3	0.13	0.10	3.0
*L0173-1	14	7.0	333	37.2	11.2	0.16	0.12	3.3
L0276-1c	12.3	6.4	292	76.6	13.1	0.31	0.27	5.9
(redb)	12.4	6.2	295	90	18.7	0.39	0.32	4.8
L0277-1c	12.2	6.1	290	148	44.8	0.65	0.50	3.3
(redb)	13.1	6.6	311	143	41.1	0.61	0.47	3.5
L0278-1c	13.4	6.7	319	157	44.8	0.69	0.54	3.5
(redb)	11.7	5.9	278	179	56.0	0.87	0.66	3.2

4.1.2 A special case of the PL spectroscopy: PL spectrum and its temperature dependence were studied for these two groups of samples of L0276-1, L0277-1, L0278-1, and L0171-2c, L0172-5c and L1221-2TR. We found that unlike the IR results, both the spectral lineshape and the total intensity temperature dependence showed similarity between these two groups of samples. Hence, we show the results for one group of films. Figs. 4.3(a), 4.3(b) and 4.3(c) show the PL spectra at temperatures 80 K, 160 K and 180 K; and Fig. 4.3(d) shows the PL peak energy, as a function of the measurement temperature, for samples L0276-1, L0277-1, and L0278-1. One can see that there are differences in the spectral lineshapes between the low growth rate film L0276-1 and the two higher growth rate films L0277-1 and L0278-1. The solid lines in Figs. 4.3 show that the low growth rate film L0276-1 exhibits PL characteristics that are typical for device quality intrinsic a-Si:H, i.e., the peak energy at ~1.4 eV at 80 K and it gradually decreases as the temperature increases due to carrier thermalization in tail states. However, as shown by the cross and dotted symbols for the growth rate = 3 Å/s films, the PL peak energy is red-shifted. There is a PL band at ~1.1 eV in addition to the 1.4 eV band as shown in Figs 4.3(b).

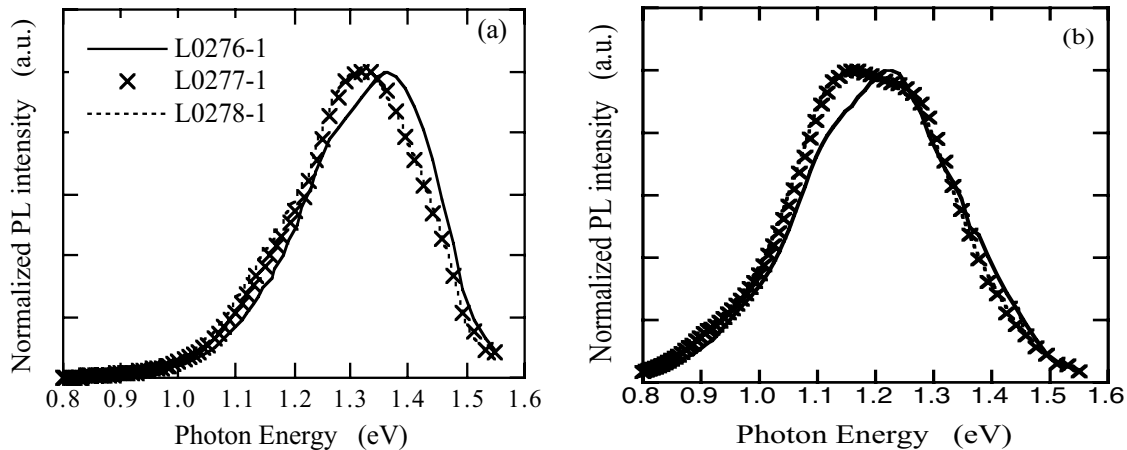


Fig. 4.3 PL results for samples L0276-1, L0277-1, and L0278-1 (a) spectra at 80 K, (b) spectra at 180 K.

The PL peak energy position as a function of temperature is shown in Fig. 4.4. The PL peak position decreases rapidly at ~170 K due to a weak-temperature dependent PL band at ~1.1 eV. A nanovoid-

related large red shift of PL peak energy in hot-wire a-Si:H has been observed recently. It is possible that the 1.1 eV PL in the high-growth rate films is related to the same microstructures that causes a lower absorption strength for the Si-H stretching mode as shown in Fig. 4.2.

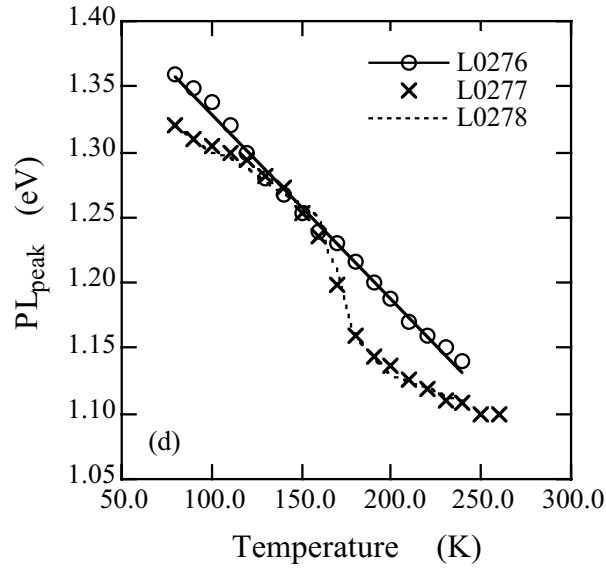


Fig. 4.4 PL peak energy as a function of temperature for samples L0276-1, L0277-1, and L0278-1.

4.1.3. Summary of the special case: The IR and PL results indicate that certain microstructures exist when the growth rate is ≥ 3 Å/s. In the following section we report the results from a second group of samples made at BPSolar using a modified deposition system. The above IR and PL results shown in Figs 4.2 and 4.3 were not reproducible in the second group of samples although the same growth conditions were used. We did not find the microstructure related unusual results of IR and PL. It indicates that the sample quality depends on not only the growth conditions but also the deposition system.

IV.2. PL Results from a Group of New Samples

4.2.1. Sample and Experimental: Four pairs of BP-Solar films, L2127, L2129, L2136, and L2137 at original State A and light-soaked state B (exposed to 1 sun, Na vapor lamp for 600 h at 50 °C) were studied by PL spectroscopy. We have also done the measurements after in-situ light soaking using a 200 mW/cm² white light at 40 °C for two hours. The sample conditions and their PL parameters are listed in table IV.3. The PL energy spectra were measured at the temperature range of 80 K - 300 K

Table IV.3 The sample preparing conditions and their PL parameters

Sample ID	Growth rate (Å/s)	Thickness (µm)	Peak _{main} at 80 K (eV)	Slope of I _{main} , T _L (K)
L2127	1	1.79	1.35	24
L2129	3	1.47	1.36	27
L2136	5	1.65	1.36	28
L2137	10	1.76	1.34	40

where Peak_{main} and I_{main} are the peak energy position and the integral intensity of the PL main band.

4.2.2. PL Results

PL energy spectra at low temperatures. Figure 4.5 shows the PL spectra at 80 K for those four samples listed in table IV.3. The spectral lineshapes show the same features as that of typical device-quality intrinsic a-Si:H; whereas, the peak energy position, $\text{Peak}_{\text{main}}$, is slightly different. The highest growth rate film shows the lowest $\text{Peak}_{\text{main}}$ that can be related to a broader band tail and/or a narrower optical gap. Fig. 4.6 shows the PL spectra at 80-160 K for sample L2127. One can see that both the PL intensity and the $\text{Peak}_{\text{main}}$, decrease when the temperature increases due to carrier-thermolization in the band tail states.

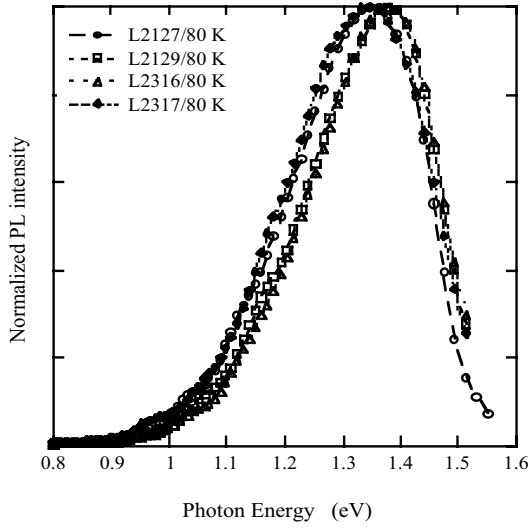


Fig. 4.5 PL spectra of samples with growth rate of 1, 3, 5 and 10 Å/s at 80 K.

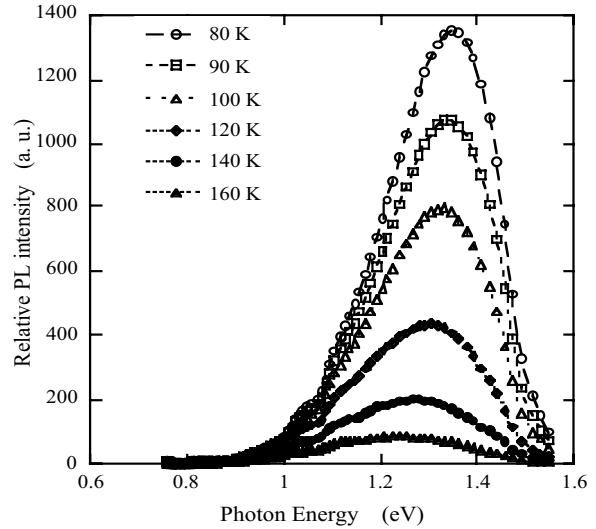


Fig. 4.6 PL spectra of sample with growth rate of 1 Å/s at temperatures of 80 - 160 K.

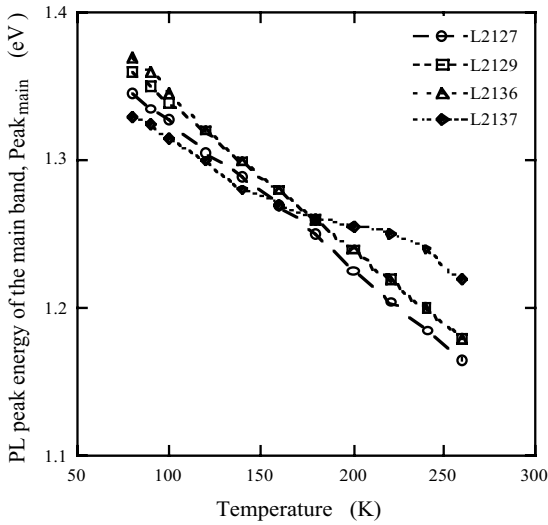


Fig. 4.7 $\text{Peak}_{\text{main}}$ of samples L2127, L2129, L2316 and L2317 as a function of temperature.

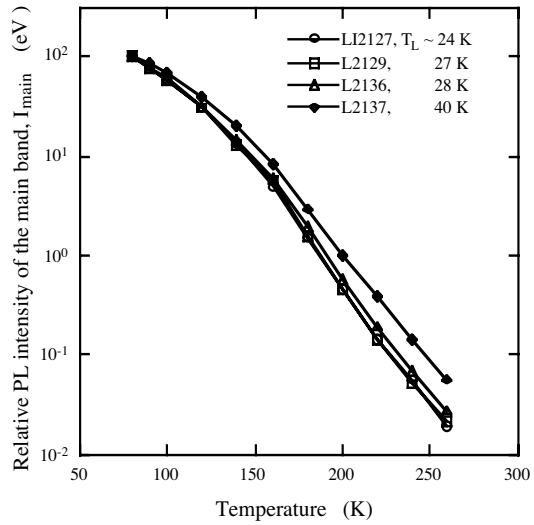


Fig. 4.8 I_{main} of samples L2127, L2129, L2316 and L2317 as a function of temperature.

PL intensity temperature dependence: The $\text{Peak}_{\text{main}}$ position and the integral intensity, I_{main} , as a function of temperature at State A for those four films are plotted in Figs. 4.7 and 4.8, respectively. One can see that for the samples with a growth rate from 1 to 5 Å/ both $\text{Peak}_{\text{main}}(T)$ and $I_{\text{main}}(T)$ is similar as that for typical device-quality a-Si:H. However, for the sample with a growth rate of 10 Å/s both the $\text{Peak}_{\text{main}}$ and I_{main} show much weaker temperature dependence. Especially, the PL peak energy is "saturated" at ~ 1.25 eV when $T > 160$ K. This indicates a deep trapping state in this high growth rate sample. The slope of the I_{main} , T_L , is listed in table IV.3.

4.2.3 In-situ light soaking: The I_{main} decreased slightly and the integral defect PL intensity, I_{defect} , clearly increased after light soaking for two hours. Figure 4.9 shows the I_{defect} as a function of T at State A for those four samples. Figure 4.10 shows the light-induced increase of I_{defect} at 260 K.

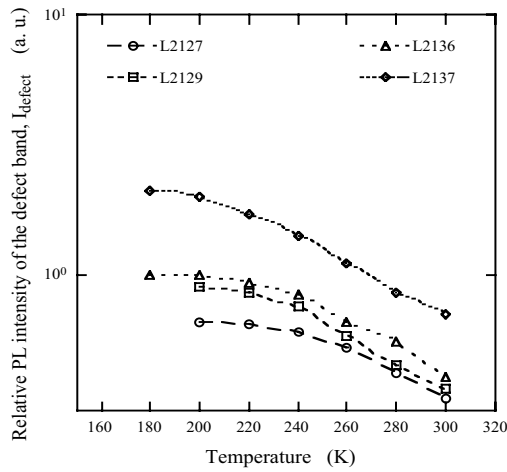


Fig. 4.9 Defect PL intensity I_{defect} as a function of temperature for the four samples.

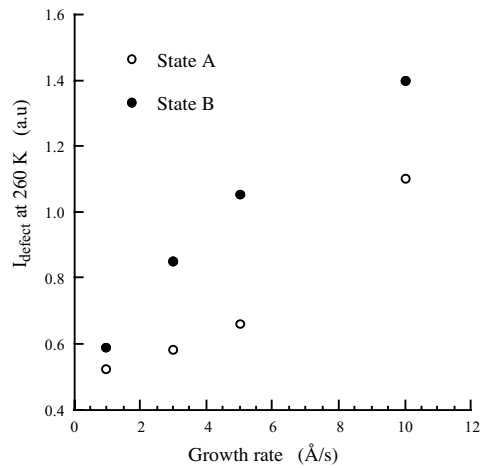


Fig. 4.10 I_{defect} at 260 K as a function of the growth rate before and after light soaking.

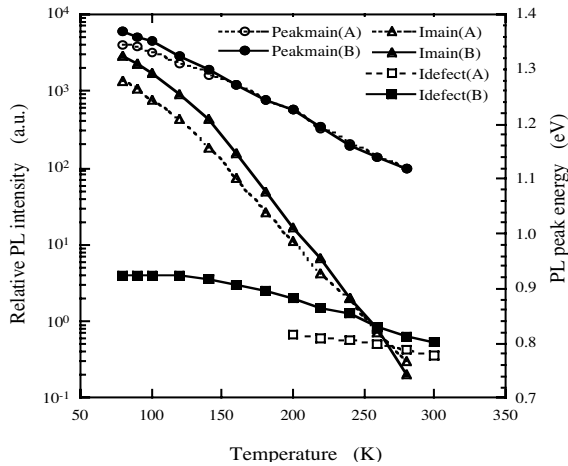


Fig. 4.11 the $\text{Peak}_{\text{main}}$, I_{main} , and I_{defect} vs. T for sample L2127 at State A and State B.

Finally, we show the $\text{Peak}_{\text{main}}$, I_{main} , and I_{defect} for sample L2127 at State A and State B (50 °C, 1 sun, Na vapor lamp for 600 h) in Fig. 4.11. Although the light soaking was not in-situ, the tendencies of light-induced changes are the same, i.e. a decrease of the I_{main} and an increase of the I_{defect} .

IV.3. Summary and Discussion

Unlike the unusual IR and PL results of the first group of samples, the results from the second group of samples are usual (because the deposition system was modified). It suggests that increasing the deposition rate from 1 to 5 Å/s has a modest effect on the electronic tail states and a gradual increase of defect states. The latter, perhaps, will not affect the solar cell performance. Especially, the features of the samples with a growth rate of 3 and 5 Å/s are very close to each other. An increase of the growth rate to 10 Å/s has a dramatic effect in the electronic states. In addition to the broader tail states and higher density of dangling bond states, the deep-trapping states may be related to the microvoids. The material is much more defective compared to the others, that is in consisting with the results of the microstructural studies [11]. The total PL intensity decreased and the relative defect PL intensity increased after light-induced metastable defect creation. We have noticed that the low-growth-rate film (1 Å/s), L2127, shows some unusual features such as the peak energy position is lower than that of the films with a higher growth rate of 3 and 5 Å/s (se Figs. 4.5 and 4.7) and an increase instead of a decrease of both the $Peak_{main}$ and I_{main} after light soaking (see Fig.4.11). We have double-checked the data that were reproducible. The reason remains unclear.

V. Systematical Raman study of thin films from amorphous-to-nanocrystalline silicon prepared by HW-CVD [12]

V.1 Introduction

Raman spectroscopy is a sensitive tool to study the structures of a-Si-based materials. In a-Si, all phonon modes of the transverse acoustic (TA), longitudinal acoustic (LA), longitudinal optical (LO), and TO modes are Raman active. Thus, Raman spectra from a-Si at room temperature yield a reasonable spectral comparison with phonon density of states that are modified substantially by small changes in short-range order (SRO). Theoretical calculations found that the width FWHM, the peak frequency of the TO phonon mode (ω_{TO}), and the relative intensity of the TA mode, TA/TO, are sensitive to bond-angle variation ($\Delta\Theta$) in an a-Si network. Beeman et al. [13] found a linear relationship between the width of the TO mode and the spread in the mean bond angle $\Delta\Theta$ in an a-Si network as

$$FWHM = 15 + 6\Delta\Theta. \quad (5.1)$$

More recent calculations using 1000-atom configurations showed a similar relation of $\Gamma = 18.4 + 6.6\Delta\Theta$ and a shift of the TO mode frequency toward higher frequency as $\Delta\Theta$ decreases following

$$\omega_{TO} = -2.5 \Delta\Theta + 505.5 \quad (5.2)$$

for HV-polarized light. The authors further found that the TA/TO intensity ratio decreases linearly with decreasing $\Delta\Theta$. For device-quality a-Si:H, the TO mode centered at 480 cm^{-1} with FWHM $\sim 70 \text{ cm}^{-1}$. According to equation (5.1), the spread in mean bond angle $\Delta\Theta$ is $\leq 10^\circ$. In c-Si, on the other hand, the Raman spectrum consists of a single sharp TO mode with FWHM of 4 cm^{-1} at a frequency of 520 cm^{-1} . All other modes are not Raman active because of the symmetry in the fcc lattice. However, when the c-Si grain size is as small as a few nm, the momentum conservation will be relaxed and Raman active modes will not be limited to the center of the Brillouin zone. Thus, the frequency could shift from 520 cm^{-1} to $\sim 512 \text{ cm}^{-1}$ with decreasing grain size from ≥ 10 to ~ 3 nm. Below 3 nm, a crystalline-to-amorphous transition occurs. In addition to the a-Si and c-Si phonon modes, the Raman TO mode from nc-Si films contains a third intermediate peak centered around $500 \pm 10 \text{ cm}^{-1}$ which could be attributed to the contribution of grain boundaries or other structures. With hydrogen dilution, Tsu et al. found chainlike

objects in PE-CVD films using high-resolution transmission electronic microscopy (TEM) which they claim is evidence for intermediate ordering in H-diluted films. They found that the a-Si TO band centered at 490 cm^{-1} ($37 \pm 3 \text{ cm}^{-1}$ full width) instead of 480 cm^{-1} .

To determine the c-Si volume fraction from the Raman TO mode, one must take into account the differences between a-Si and c-Si with respect to scattering cross sections and optical absorption coefficients. Bustarret et al. found that the ratio of the cross section for the amorphous-to-crystalline phase for grain size $> 3 \text{ nm}$ at the excitation wavelength 514.5 nm can be written as

$$y(L) = 0.1 + \exp[-(L/250)]. \quad (5.3)$$

It is expected that $y(L)$ will be 2.4 times smaller at 632.8-nm excitation. Based on the above argument, we deduced the crystalline volume fraction, X_c , from the Raman TO mode using

$$X_c = (I_c + I_{gb})/[I_c + I_{gb} + y(L)I_a], \quad (5.4)$$

where $I_c + I_{gb}$ and I_a are integrated intensities of the c-Si, intermediate, and a-Si peaks, respectively; $y(L)$ decreases from 1 to 0.4 when the grain size L grows from 3 nm to 30 nm . We found that when using 514.5-nm laser front excitation, X_c can be deduced in such a way to be consistent with the results from x-ray diffraction (XRD) for HW-CVD transition films. In previous works, we reported Raman, XDR, FTIR, PL, and optical absorption results for HW-CVD films with either varied hydrogen-to-silane ratio, R , with fixed silane flow rate or varied substrate temperature, T_s , at fixed $R = 3$. We observed a blue shift of the a-Si:H PL peak frequency, which was due to narrowing of the band tail states by hydrogen dilution and a low-energy PL band in the nc-Si films. The low-energy PL band originates from the c-Si g.b. regions, and thus, we have attributed the intermediate component of the Raman TO mode to the g.b. regions. The previous Raman results showed a threshold of $R \approx 2$ at $T_s = 240^\circ\text{-}250^\circ\text{C}$ and $T_s \approx 200^\circ\text{C}$ at $R = 3$ for the structural transition from a- to nc-Si:H. Both the threshold growth conditions of crystallinity and the crystalline silicon volume fraction deduced from the Raman TO modes are consistent with the results from XRD. In this work, we have extended our deposition parameter range to include not only the H-dilution ratio R , but also the effect of silane flow rate and total gas pressure. For example, at a fixed R , the individual SiH_4 and H_2 flow rates can be changed so that one condition has a higher silane flow rate than the other. The films deposited at the same R were not the same and depended on the actual gas flow rates. This systematic study of the correlation between material structure and deposition conditions can help us understand the growth mechanism and adjust the growth conditions of nc-Si:H films.

V.2. Sample and Experimental

We studied 125 intrinsic Si films by HW-CVD on Corning 1737 $25 \times 25 \text{ mm}^2$ glass. All of the films were grown at the same substrate temperature, $T_s = 240^\circ\text{C}$. There were four groups with various silane flow rates of 3, 8, 16, and 22 sccm, respectively. The hydrogen flow rate for each group was varied from 0 to 216 sccm. The total gas pressure was controlled by adjusting the throttling valve position (TVP) at 45%, 50%, 60%, 70%, and 80%. The higher percentage leads to lower pressure. For the films with a low silane flow rate of 3 sccm, the thickness was controlled in the range of $1500\text{-}2000 \text{ \AA}$, and the growth rate was in the range of $1\text{-}3 \text{ \AA/s}$; for the films with silane flow rates of 8 and 16 sccm, the thickness was controlled in the range of $5000\text{-}6000 \text{ \AA}$, and the growth rate was in the range of $5\text{-}13 \text{ \AA/s}$; for the films with a silane flow rate of 22 sccm, the thickness was controlled in the range of $0.9\text{-}1.1 \text{ }\mu\text{m}$, and the growth rate was in the range of $8\text{-}21 \text{ \AA/s}$. Two films were made as thin as the penetration depth of the 514.5-nm laser, $60\text{-}70 \text{ nm}$, and these were used for calibrating the Raman spectra from back excitation.

Raman spectra were measured using an XY triple spectrograph equipped with a LN-cooled CCD detector. The data were taken at room temperature using the 514.5-nm line of an argon-ion laser. The spectral resolution was approximately 0.5 cm^{-1} in a frequency range of 100 to 1000 cm^{-1} . The frequency of the Raman lines was calibrated using the TO mode of a (111) c-Si wafer at 520 cm^{-1} . The power of the laser was kept below the level that would thermally induce crystallization. The penetration depth of the 514.5-nm light is $\sim 60 \text{ nm}$ for a-Si:H and is larger for nc-Si:H. Since the Raman spectra reveal the structure of the thin layer, measurements were also done from back-excitation for most samples. To depress the scattering light from the substrate, the light spot was focused on the film using a microscope. The c-Si grain size ranged from 7 to 30 nm, which was obtained from XRD; the crystalline volume fraction, X_c , was deduced using equations (5.3) and (5.4) with $0.4 < y(L) < 0.85$.

V.3. Results and discussion

In general, the structure change is a function of the ratio of hydrogen-to-silane flows, R . Fig. 5.1(a-p) shows the crystalline silicon volume fraction, X_c , as a function of R for four groups of films at SiH_4 flow rates of 3, 8, 16, and 22 sccm and with the total gas pressure varied with the throttling valve position (TVP) of 45%, 50%, 60%, 70%, and 80%. The solid and dotted lines indicate the X_c obtained from the top and bottom layer, respectively. The X_c is found from zero to $>90\%$ (including $X_{g.b.}$ from zero to $\sim 30\%$) in the top layers. In agreement with the previous works, there is a threshold R for the structural transition from a- to nc-Si:H. The common features of the curves in Fig. 5.1(a-p) are: (a) Narrow structure transition region ($\Delta R \sim 1$) from $X_c = 0$ to $\geq 50\%$. We will analyze this transition region in detail shortly. (b) The threshold R of crystallinity increases with increasing SiH_4 flow rates. For instance, the threshold is $R \leq 2$ for low SiH_4 flow rates of 3 and 8 sccm, as shown in Figs. 5.1(a-g), but no crystallinity has yet occurred at $R=2$ for high SiH_4 flow rates of 16 and 22 sccm as shown in Figs. 5.1(i-p). (c) The X_c changes with the total pressure in the chamber in the following way: the films easily become nc-Si at the higher pressure (lower TVP) and lower silane flow rates of 3 and 8 sccm as seen by comparing Figs. 5.1(a) to 5.1(d) and 5.1(e) to 5.1(h); whereas, at high silane flow rates of 16 and 22 sccm, a lower pressure (higher TVP) yields a higher X_c in the film as seen by comparing Figs. 5.1(i) to 5.1(j) or 5.1(m) to 5.1(n).

These surprising results suggest that there is a “growth zone” for the crystallite, and it is our intention to study many deposition parameters, and not just R , to examine this further. We used back excitation to study the early growth of the film. At the early stage of the growth, X_c is much lower than in the late growth of the films as shown by the dotted lines in Fig 5.1. Whereas, in Fig. 5.1(d) for the film with $R = 72$ and $\text{SiH}_4 = 3 \text{ sccm}$, we observe roughly the same X_c value. This is because the film thickness of 70 nm is close to the penetration depth of the 514.5-nm laser. For all of the films in this study, the FWHMs of the a-Si network from the bottom layers are in the range of $75\text{-}83 \text{ cm}^{-1}$. These values are always broader than the $67\text{-}80 \text{ cm}^{-1}$ for the top layers. This implies that the a-Si:H network near the glass substrate is less ordered compared to the top surface layer.

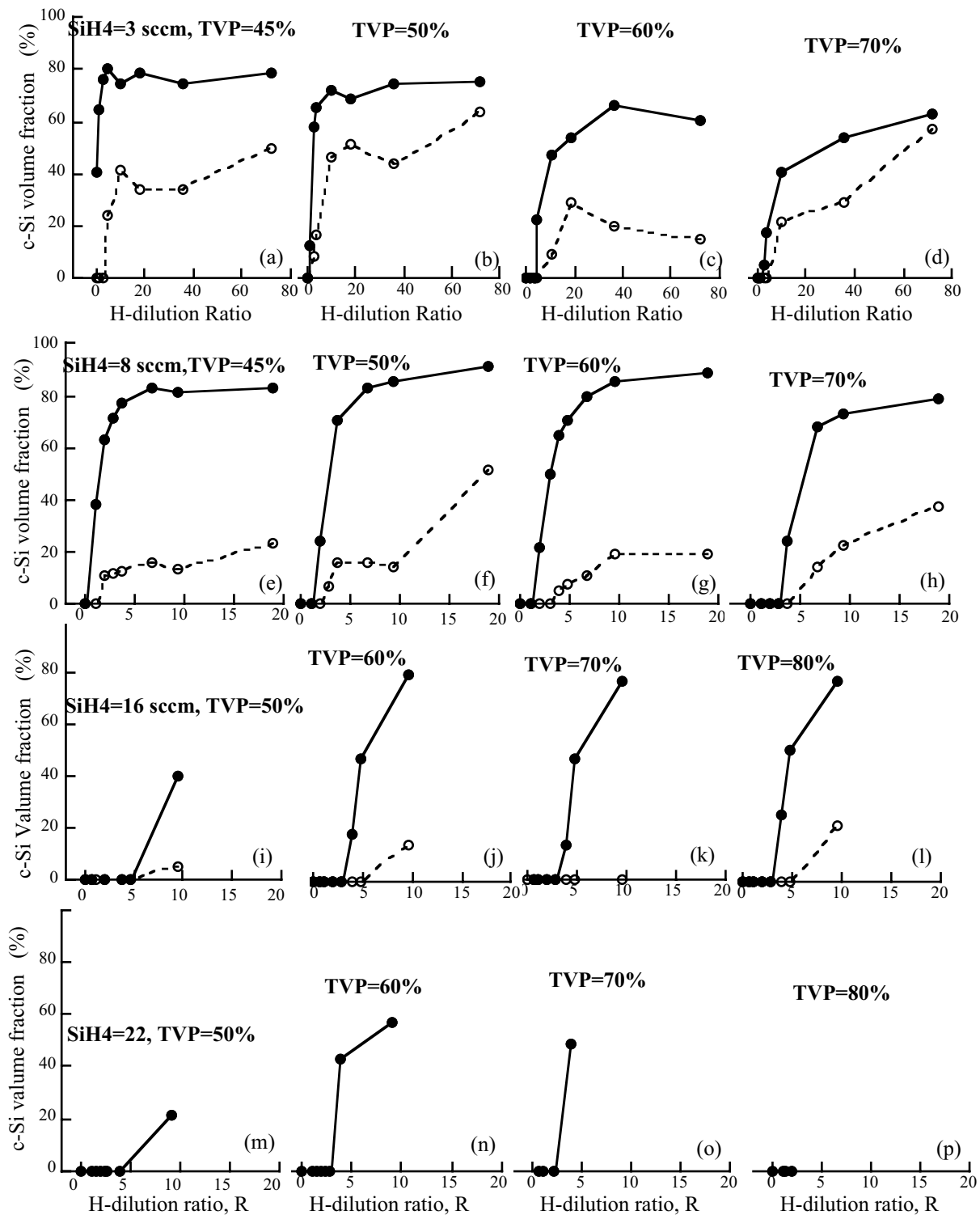


Fig. 5.1. X_c as a function of R at SiH₄ flow rates of 3, 8, 16 and 22 sccm. The solid and dotted lines indicate the X_c was obtained from the top or bottom layer of ≥ 60 nm, respectively.

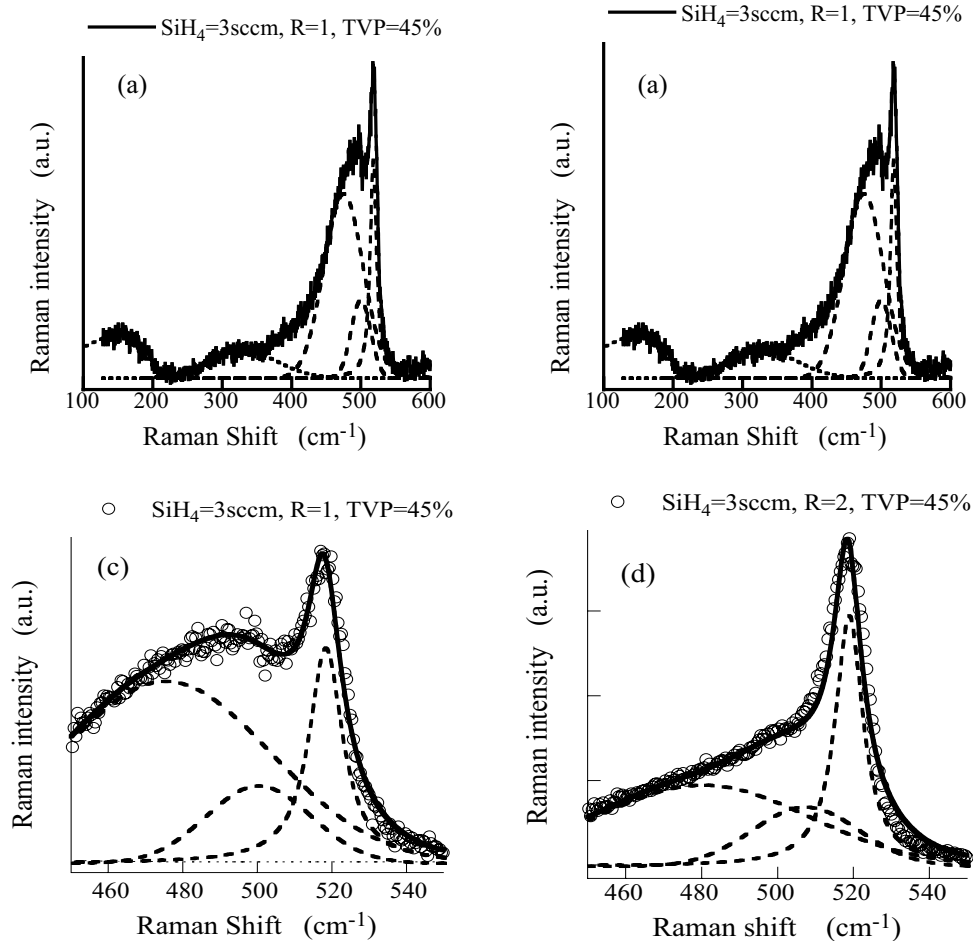
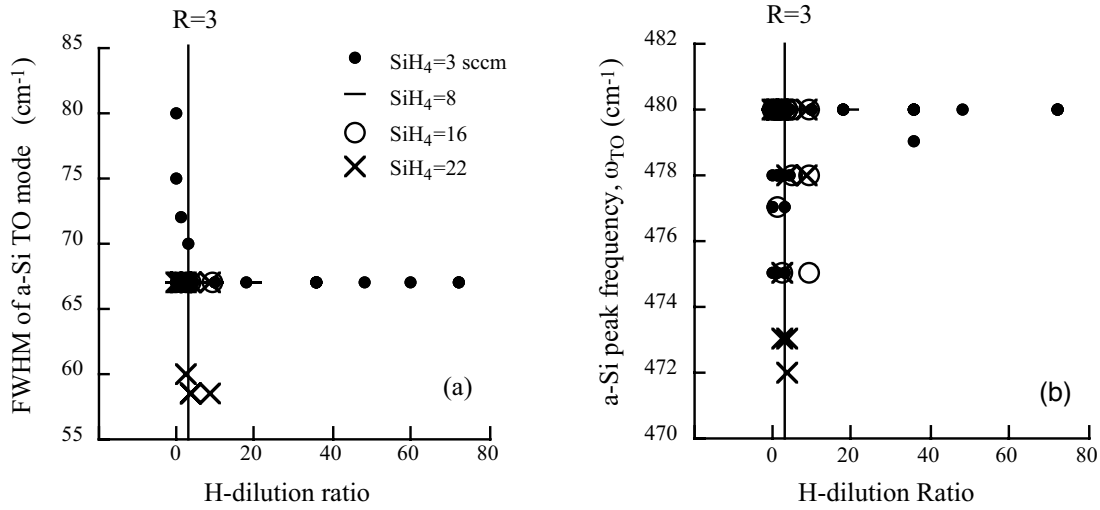


Fig. 5.2. Raman shift and their fittings from the films with SiH₄ flow of 3 sccm, TVP=45%, (a) R=1, and (b) R=2. And the enlarged TO mode of the data in 2(c) and 2(d).

Figs. 5.2(a) and 5.2(b) show the Raman spectra and their fitting functions for the films with SiH₄ flow of 3 sccm, TVP=45%, and R=1 and 2, respectively. The fittings for the TA mode peaked at 145 cm⁻¹ and the LA mode peaked at 330 cm⁻¹, which are also shown. The signal between the TO and LA modes is attributed to the LO mode. Comparing Fig. 5.2(a) and 5.2(b), one can see that the intensity ratio of TA/TO decreased as the film was more crystallized. This agrees qualitatively with the theoretical calculations. More importantly, we obtain the structure information from the TO mode according to equations (5.1) and (5.2). Figs. 5.2(c) and 5.2(d) show the enlarged TO mode between 450 to 550 cm⁻¹ for the same samples in Figs. 2(a) and 2(b). The bandwidth of the TO mode, FWHM, and their peak frequency, ω_{TO} , as a function of H-dilution ratio are plotted in Figs. 5.3(a) and 5.3(b) for all the films in this study. Generally, the FWHM decreases and the ω_{TO} increases in the narrow structural transition region and then reaches a saturation value. Notice that the films with a high SiH₄ flow rate of 22 sccm (the big crosses) show the narrowest FWHM and lowest ω_{TO} . It is perhaps related to column-like structures. The changes can be seen more clearly for the low growth rate films with a SiH₄ flow rate of 3 sccm which are represented by solid dots in both Fig. 5.3(a) and 5.3(b).



Figs. 5.3.(a) FWHM and (b) ω_{a-Si} of the TO mode as function of R. The solid dots, dashes, open circles, and crosses represent the films with a SiH₄ flow rate of 3, 8, 16, and 22 sccm, respectively. There are two regimes separated at $R \approx 3$: the fast changing regime when $R < 3$ and the saturated regime when $R > 3$.

The improvement of SRO of the a-Si:H network in the a-to-nc-Si transition region is clearly shown in both the changes of FWHM and ω_{TO} . In Fig. 5.3(a), the FWHM decreases from 80 to 67 cm⁻¹ when $0 \leq R \leq 3$, and then remains at 67 cm⁻¹ when $R > 3$. This indicates that the spread in the mean bond angle $\Delta\Theta$ decreased from 10.8° to 8.6° according to equation (5.1). The corresponding frequency shift ω_{TO} for the same films in Fig. 5.3(b) is from 475 cm⁻¹ to 480 cm⁻¹, which indicates that the $\Delta\Theta$ decreased from 12.2° to 10.2° according to Eq. (5.2). The absolute values of $\Delta\Theta$ are relatively large from the calculation, but the 2° improvement of the bond angle spread is consistent with the results from the decrease of the band width. The improvement of SRO of the a-Si network by increasing H-dilution is consistent with the observations of a narrowing of the valence band tail in our previous work. For most of the high-SiH₄-flow-rate films, indicated by the open circles and big crosses, the FWHM = 67 cm⁻¹ does not change with R, but the ω_{TO} spreads from 475 to 480 cm⁻¹ at $0 < R < 3$. Whereas, the FWHM is as narrow as 58.5 cm⁻¹ and the peak frequency as low as 472 cm⁻¹ for the films deposited with the highest growth rate of ~ 20 Å/s (represented by the big crosses). The frequencies of the c-Si and g.b. peaks for those films are also low (see Figs. 5.4 and 5.5). Since a column-type growth occurs in such conditions, it implies that both the ω_{TO} and the FWHM are sensitive to the column structures. To our knowledge, there are no calculations of how the phonon density of states changes with such structures. For the c-Si component, we generally found that the width of the c-Si TO mode for the nc-Si:H films is broader than that for the c-Si wafer, i.e., 8-10 cm⁻¹ compared to 4 cm⁻¹. There were two exceptions for films with SiH₄=3 sccm with TPV=70% and $R=1.2$ and 3. The reason is unclear why the FWHM was as narrow as 4 cm⁻¹ for those two films. However, the peak frequency of the c-Si TO mode, ω_{c-Si} , changes when R increases. For the films with SiH₄ flow rate of 3 and 8 sccm, we found a blue shift from 516 to 520 cm⁻¹ in the transition region, as shown in Fig. 5.4. This indicates that the crystallite size has increased from ~ 7 nm to ≥ 10 nm. For the films with a high SiH₄ flow rate of 22 sccm, the big crosses indicate that the ω_{c-Si} blue shift occurs from 513 to 518 cm⁻¹. Again, the relatively low frequency of the c-Si TO mode could be due to the column-like structures.

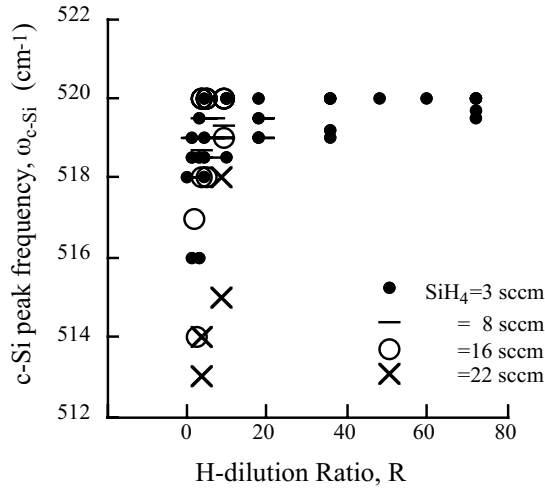


Fig. 5.4. ω_{c-Si} as a function of R.

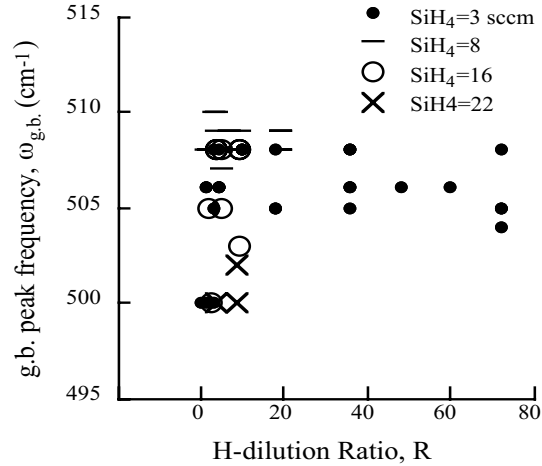


Fig. 5.5. $\omega_{g.b.}$ as a function of R.

Finally, for all the nc-Si:H films, the Raman TO mode always contains an intermediate component in addition to the a-Si and c-Si components. The intermediate component was fitted well using a Gaussian function with FWHM of 33 cm^{-1} for all the nc-Si:H films. The peak frequency of the intermediate component, $\omega_{g.b.}$, as a function of R is plotted in Fig. 5.5. One finds that the value spreads from 500 to 510 cm^{-1} . For the low-growth-rate films, there is a blue shift of the $\omega_{g.b.}$ from 500 to 507 cm^{-1} in the transition region and then spreads between 505 to 507 cm^{-1} when $R > 3$. Regardless of whether the intermediate component originates from the grain boundaries, small size ($< 3 \text{ nm}$) crystallites, or median-range ordered objects, the blue shift of the $\omega_{g.b.}$ can be attributed to the growth of the c-Si grain size. One may argue that Raman modes reflect SRO, and the phonon density of states is sensitive to the local bond angles. However, the scattering intensity is related to a coupling-parameter-weighted phonon density of states. Small differences between peak positions could be attributed to changes in median- or long-range interactions that are consequences of the coupling parameter. We could not clarify the origin of this intermediate component in this work. Whatever the origin is, one commonly takes the third component into account as part of the c-Si volume fraction as seen in equation (5.4). As shown above, the peak frequencies of all the three components of the TO modes show blue shift with an increase of H-dilution in the structural transition region. The compressive stress could be higher in films with higher hydrogen dilution ratios (the film easily peels off from the substrate), and the blue shift of the phonon bands could be partially related to an increase of the film stress.

V.4. Summary

Raman scattering studies were carried out on the transition films from amorphous-to-nanocrystalline silicon prepared by HW-CVD with varied silane and hydrogen flow rates and the T-valve position. The measurements were done for both front and back excitation. The TO mode was deconvoluted into a broad Gaussian function for the a-Si:H and a narrow Lorentzian function for the c-Si; a Gaussian function peaked at between 500 to 510 cm^{-1} with FWHM of 33 cm^{-1} for the intermediate component. We believe that the origin of the intermediate component is the grain boundaries and the small-size ($< 3 \text{ nm}$) crystallites, and attribute it into the total c-Si volume fraction. The c-Si volume fraction depends not only on the H-dilution ratio, $R = \text{H}_2/\text{SiH}_4$, and the film thickness, but also on the SiH_4 flow rate and total gas

pressure which can be explained using the silane-depletion model. The detailed calculation of gas depletion will be reported in a future work.

The most interesting finding is a narrow structural transition region of $\Delta R \sim 1$, in which the short-range order of the a-Si:H network is improved: the width of the TO mode decreased from 80 to 67 cm^{-1} and the peak frequency, ω_{TO} , blue shift from 475 to 480 cm^{-1} . These indicate that the bond-angle variation, $\Delta\Theta$, decreases from $\sim 10^\circ$ to $\sim 8^\circ$ when the crystallites start to grow. Furthermore, the crystallite grain size increases from ~ 7 nm to ≥ 10 nm in the transition region, evidenced by a blue shift of the c-Si mode, $\omega_{\text{c-Si}}$, from 516 to 520 cm^{-1} . When R continually increases beyond the transition region, the SRO of the a-Si:H network, the c-Si volume fraction, and the c-Si peak frequency are somewhat saturated. However, the structure would be continually modified at a higher hydrogen dilution ratio. Other techniques such as TEM will assist in clarifying the further structural changes.

Finally, when the films were deposited with a high growth rate ~ 20 Å/s using a high SiH_4 flow rate, the FWHM of the TO mode for a-Si network can be as narrow as 58.5 cm^{-1} and the peak frequency as low as 472 cm^{-1} . A column-type growth occurs in such conditions, which implies that both the ω_{TO} and the FWHM are sensitive to the column structures. Calculations are needed to find how the phonon density of states changes with such structures.

V.5 Conclusion

There is a narrow structural transition region of $\Delta R \sim 1$, in which the short-range order of the a-Si:H network is improved that, i.e., the bond-angle variation, $\Delta\Theta$, decreases from $\sim 10^\circ$ to $\sim 8^\circ$ and the crystallites start to grow. The crystallite grain size increases from ~ 7 nm to ≥ 10 nm in the transition region.

VI . Micro-Raman Studies of Mixed-Phase Hydrogenated Silicon Solar Cells [14]

VI.1. Introduction

A significant light-induced enhancement in the open-circuit voltage (V_{oc}) of mixed-phase silicon solar cells was observed. Since the average grain size is in the order of a few nano-meters in the mixed-phase material, the magnitude of the variation in V_{oc} (ΔV_{oc}) depends on the intrinsic (*i*) layer thickness, the deposition temperature, the initial V_{oc} , and the light soaking intensity. Under intense light soaking, a ΔV_{oc} as large as 150 mV has been observed. Subsequent annealing of the solar cells substantially restored the original V_{oc} values. *In-situ* PL spectral studies found that the PL intensity and peak-energy position associated with the amorphous component of the mixed-phase material increase upon light soaking. We proposed that a reduction of X_{c} or size is responsible for the V_{oc} enhancement. However, recent studies by conventional Raman and X-ray diffraction spectroscopy found no observable changes before and after light soaking, prompting us to carry out further investigations.

Raman spectroscopy is a sensitive tool that provides valuable structural information about a-Si:H materials. For the mixed-phase material, the X_{c} is low, and the distribution of the grains might be non-uniform. Using conventional Raman to detect the existence of nano-grains is difficult. However, micro-Raman is an effective tool for detecting nano-grains and providing their distribution information. In this paper, we present the micro-Raman data on the mixed-phase solar cells, which correlated well the structural non-uniformity to the physical model of light-induced increase of V_{oc} observed in the mixed-phase solar cells.

VI.2 Sample and Experimental

Single-junction *n i p* solar cells were deposited by United Solar onto 4 cm × 4 cm stainless steel (ss) substrates using a conventional *rf* glow discharge technique. Indium-tin-oxide (ITO) dots of area 0.25 cm² were deposited on the *p* layer as the top contact. The deposition parameters were adjusted to arrive at the amorphous-to-nanocrystalline transition region .

The Raman spectra were collected under ambient conditions using the 514.5 nm line of an argon-ion laser. The penetration depth of the 514.5-nm light is ~60 nm for a-Si:H and is larger for nc-Si:H. The spectral resolution was approximately 0.5 cm⁻¹ in a frequency range of 100 to 1000 cm⁻¹. The frequency of the Raman lines were calibrated using the TO mode of a (111) c-Si wafer at 520 cm⁻¹. A low laser power was used to avoid possibility of laser-induced crystallization. The incident beam was approximately three microns in diameter. At first, four Raman scans were taken on the bottom quadrant of the dots. The locations of the scans are shown in Fig. 6.1(a). Since non-uniformity appears to be more pronounced for the cells with $V_{oc} \sim 0.75$ V, twenty scans were made in steps of 500 μm in the same bottom quarter of sample 13678-42, as indicated in Fig. 6.1(b). The laser beam was moved to a new spot on the ITO dot. This allowed us to scan the samples under the same initial conditions for each scan and thereby avoid any residual effects (such as light induced metastable effects) of laser radiation at the previously irradiated spot.

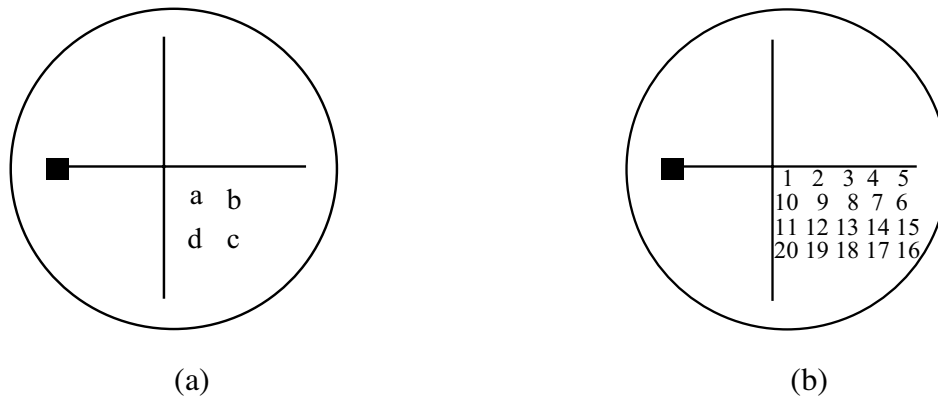


Fig. 6.1. Schematics of (a) 4 scans for all samples, and (b) 20 scans for 13678-42.

VI.3 Results and Discussion

A cell's V_{oc} can be conveniently used to determine if it is in the amorphous or mixed phase. Cells with high, low, and medium V_{oc} , corresponding to a-Si:H, nc-Si:H and mixed-phase Si solar cells were studied. Table VI.1 lists the V_{oc} values and the Raman features for four scans on each cell. The four scans for sample 13687-32 with $V_{oc} = 0.981$ V are the same and exhibit the typical amorphous signature, as seen in Fig. 6.2. The spectrum can be decomposed into four broad Gaussian distributions: one centered at 480 cm⁻¹ with a FWHM of 67 cm⁻¹ representing the TO mode, one at ~ 140 cm⁻¹ with FWHM of 100 cm⁻¹ representing the TA mode, one around ~330 cm⁻¹ with FWHM of 117 cm⁻¹ representing the LA mode, and one around ~ 440 cm⁻¹ with FWHM of 100 cm⁻¹ representing the LO mode. The four components in the spectrum are typical for high quality a-Si:H material. Figure 6.3 shows the Raman TO mode for sample 13678-13 with a $V_{oc} = 0.674$ V. All Raman spectra indicate a nc-Si:H material with a sharp c-Si TO mode around 516 cm⁻¹ appears. We decompose the Raman spectrum to calculate X_c using Eq. (5.4) and obtain a volume fraction of 35%-56%.

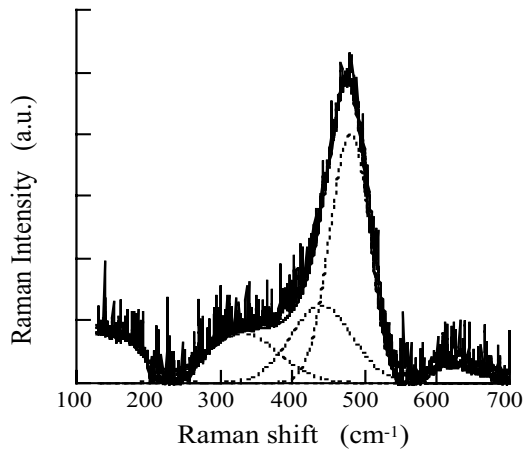


Fig. 6.2 Raman spectrum of 13687-32.

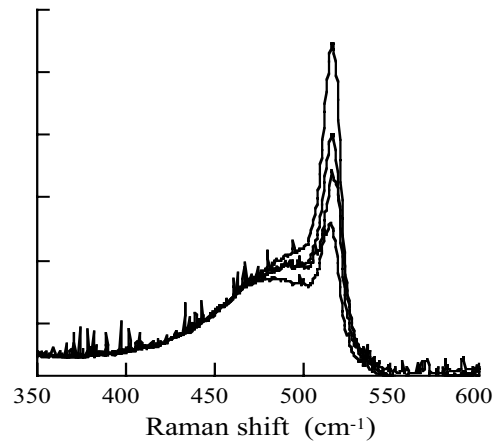


Fig. 6.3 Raman spectrum of 13678-13.

Table VI.1. V_{oc} of the mix-phase solar cells and their Raman results

Sample ID	V_{oc} (V)	Raman lineshape for four scans
13687-32	0.981	All broad a-Si peak at $\sim 480 \text{ cm}^{-1}$
13678-42	0.767	All broad a-Si peak at $\sim 480 \text{ cm}^{-1}$
13678-43	0.748	One with c-Si peak at $\sim 516 \text{ cm}^{-1}$
13678-13	0.674	All sharp c-Si peak at $\sim 516 \text{ cm}^{-1}$

When the mixed-phase cells with $V_{OC} \sim 0.767 \text{ V}$ and $\sim 0.748 \text{ V}$ were scanned by Raman, interesting results were observed as shown in Figs. 6.4 (a) and 6.4 (b). The four scans in Fig. 6.4(a) show typical amorphous features. In Fig. 6.4(b), three scans show the amorphous signature, but one scan clearly exhibits a sharp Lorentzian peak around 516 cm^{-1} . The fact that only one of the eight spectra shows nanocrystallinity indicates that the material is very non-uniform in the micrometer scale. One may question if the cell in Fig. 6.4 (a) also contains nc-Si, because the $V_{OC} \sim 0.767 \text{ V}$ corresponds to a mixed-phase structure. The sample in Fig. 4 (a) was further scanned in 20 systematic steps of $500 \mu\text{m}$ illustrated in Figure 6.1 (b). Since the beam size is only $3 \mu\text{m}$ in diameter, there was no possible overlap between adjacent scans.

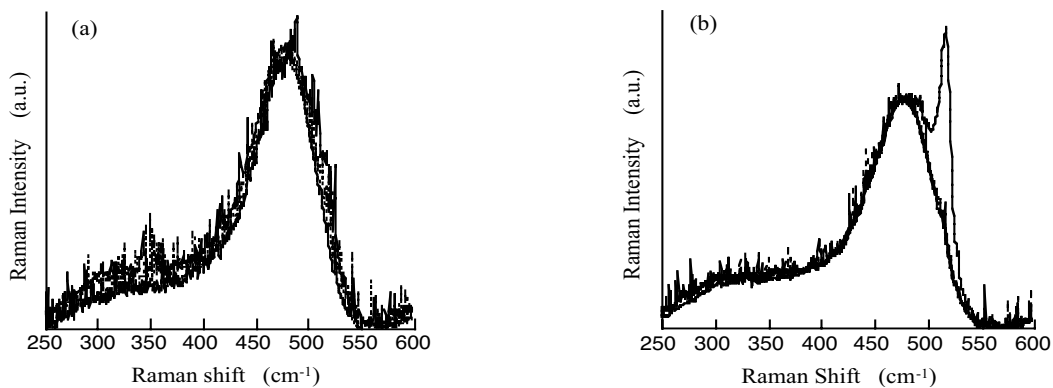


Figure 6.4. Raman shifts of mixed-phase cells with (a) $V_{oc} = 0.767 \text{ V}$ and (b) $V_{oc} = 0.748 \text{ V}$.

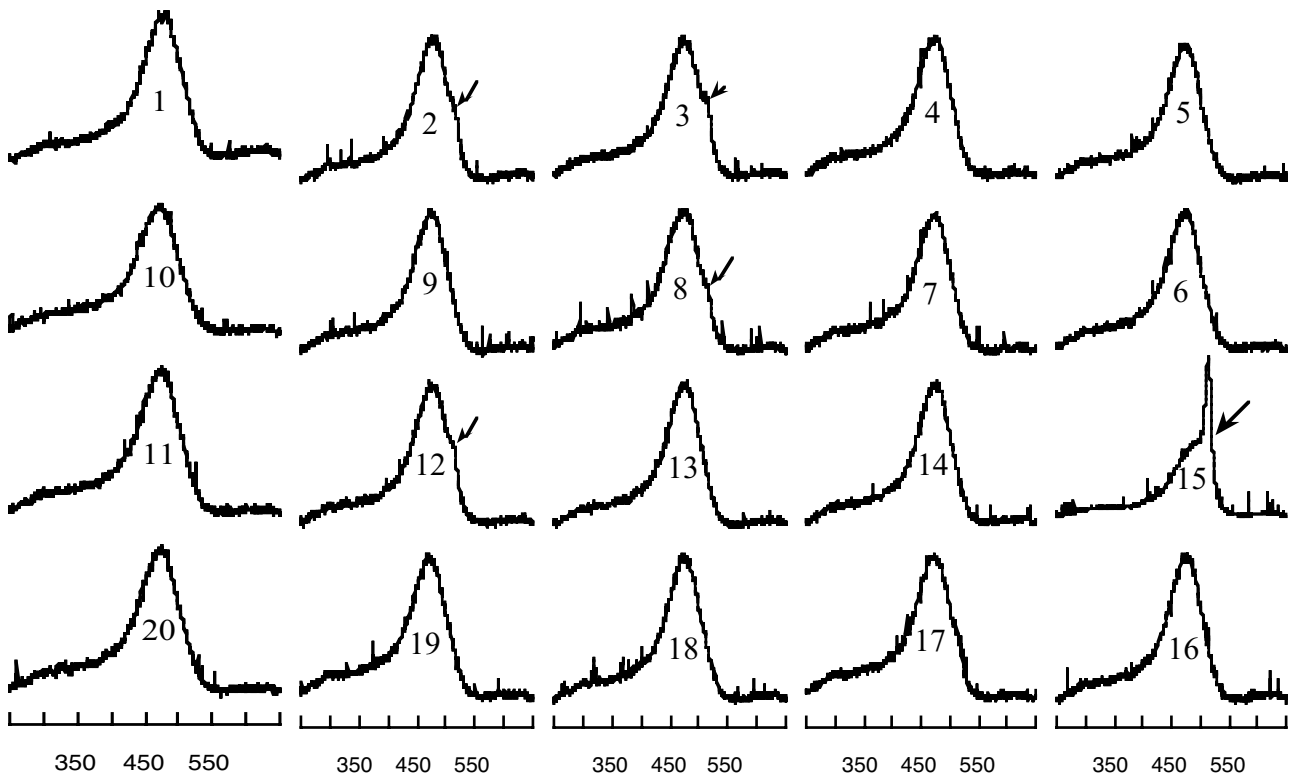


Figure 6.5. Raman Shift of 20 scans on a mixed phase cell 13678-42.

The 20 Raman spectra shown in Fig. 6.5 exhibit typical Gaussian lineshapes centered at $\sim 480 \text{ cm}^{-1}$. Several spectra show a hint of a nanocrystalline shoulder around 512 cm^{-1} . Of the entire set of spectra, only one spectrum shows definite nanocrystallinity. This confirms the structural non-uniformity for both the mixed-phase cells with $V_{oc} \sim 0.767 \text{ V}$ and $\sim 0.748 \text{ V}$. For the c-Si peak on 13678-43 and 13678-42, the frequency was at 516.7 cm^{-1} and 514 cm^{-1} , respectively. It is clear that the small c-Si grains are not uniformly distributed in the a-Si:H matrix but are clustered in a micrometer-size spot. In the two-diode model, a mixed-phase solar cell is equivalent to two diodes connected in parallel. One diode has the characteristics of an a-Si:H cell with V_{oc} around 1 V, and the other one has the characteristics of an nc-Si:H cell with a V_{oc} below 0.5 V. It is assumed in the model that a certain area of the cell contains more nanocrystallites than the others. In this case, the lateral transport between the a-Si:H phase and the nc-Si:H phase becomes negligible. The non-uniform distribution of nanocrystallites obtained by micro-Raman measurements in this study provides a direct supporting evidence for the assumption.

VI.4 Summary

We used micro-Raman spectroscopy to study the degree and dimension of the structural uniformity of mixed-phase silicon solar cells. Low-laser power was used to avoid possible thermal effects. For a cell with $V_{oc} = 0.981 \text{ V}$, four scans on different locations of the cell show typical broad Gaussian lineshapes around 480 cm^{-1} , indicative of an amorphous silicon structure. All scans of the cell with $V_{oc} = 0.674 \text{ V}$ show a sharp Lorentzian peak around 516 cm^{-1} , with an estimated 40% nanocrystalline volume fraction. For mixed-phase cells with $V_{oc} = 0.748$ and 0.767 V , one of twenty and one of four spectra, respectively,

exhibited both a broad Gaussian lineshape around 480 cm^{-1} and a sharp peak around 516 cm^{-1} . This suggests that a large fraction of a-Si:H component but small fraction of nc-Si:H grains within the mm dot of the mixed phase cells. The spatial distribution of the nc-Si:H grains is clustered in a micrometer spot. The light-induced V_{oc} enhancement has been observed in such mixed-phase cells. The structural non-uniformity observed in this micro-Raman study provides direct supporting evidence for the two-diode model recently proposed for explaining the light-induced V_{oc} enhancement in mixed-phase solar cells.

VI.5. Conclusion

A small fraction of c-Si grains clustered within the mm dot in the mixed phase cells. This micro-Raman study provides direct evidence of the structural non-uniformity that causes the light-induced V_{oc} enhancement in mixed-phase solar cells.

VII. Toward understanding the degradation without light soaking in hot-wire a-Si:H thin films and solar cells [15]

VII.1 Introduction

The advantages of HW-CVD are the simplicity in gas decomposition, the absence of ion bombardment, and the high growth rate compared with the standard PE-CVD. High performance a-Si:H based solar cells and thin-film transistors have been made using HW-CVD. In addition, several new physical phenomena were observed in the HW thin films. For instance, the NMR studies showed a new hydrogen distribution in HW films compared to PE-CVD films, the internal friction studies showed HW films have a much lower friction value than glass and are very close to the value of c-Si. In the high growth-rate films, the findings of the confinement effect on spin-spin interactions in nanogaseous systems and nanovoid-related large red shift of PL peak energy have been reported. The features of light soaking effects in HW a-Si:H films were distinguished from those in conventional PE-CVD films. The PC decreased only slightly and the dark conductivity increased in the films deposited at a substrate temperature $\geq 320\text{ }^{\circ}\text{C}$. The increase of the density of the metastable dangling bonds (ΔD°) was found to be the same as that in PE-CVD films. On the other hand, it has been reported that in addition to the light-induced degradation the HW solar cells showed a few percent decrease in efficiency without exposure to the light. Most degradation in fill factor has shown in the air but not in the vacuum or in liquid nitrogen environment. Those results suggest a possible post-oxidation in the devices. The degradation without light soaking is a more serious problem in the HW-CVD samples than that in the PE-CVD samples. In this work, we studied in detail the variations in electronic properties of intrinsic HW films in terms of gas adsorption and thermal annealing in order to understand the phenomena of degradation in the dark.

VII.2 Experimental Details

Intrinsic HW a-Si:H films with low initial dark conductivity and large $E_a \geq 0.85\text{ eV}$ were selected as listed in Table VII.1. One standard PE-CVD film, A7119, was used for comparison. Group 2 was a pair of films with and without a thin SiN_x passivation layer for post-oxidation study. Group 3 was one sample that was cut into three pieces for gas adsorption and thermal annealing studies. Corning-1737-glass substrate was used for all the samples. The coplanar metal contacts were first deposited on the glass. The details of the HW-CVD system are published elsewhere [12].

Table VII.1. Sample information

Group	Sample ID	T_s (°C)	Growth Rate (Å/s)
1	T773	360	10
	T779	360	10
	T837	400	12
2	H1441	360	14
	H1442	360	14
3	H1540a	320	12
	H1540b	320	12
	H1540c	320	12
	A7119 ^a	200	1

^a PE-CVD sample

The measurements were carried out in the following experiments: (a) Dark conductivity measurement at 300 K in environments of: vacuum (10^{-4} Torr), dry-oxygen gas, and air. Thermal annealing cycles were followed after storage in the above environments. (b) Conductivity activation-energy measurement with sample temperature ranging from 300 to 420 K. Before taken data, the sample was heated to 420 K for 30 min to clean up the film surface adsorption. Then, the E_a was deduced from the equation $\sigma_d = \sigma_0 \exp(-E_a/kT)$. (c) Hot-probe measurement is a simple way to distinguish between n- and p-type semiconductors using a hot-probe such as a heated soldering iron, a cold-probe and a standard multimeter. Based on the thermal-electric effect of semiconductors, when applying the probes to n- or p-type materials one obtains a current in opposite directions. Finally, PC temperature dependence was studied for two typical HW- and one PE-CVD film.

VII.3 Result and discussion

For group 1 HW samples, the PC decreased only slightly and the dark conductivity increased upon light soaking. We used hot probe to exam the conductive type of the intrinsic samples. We found that high T_s HW samples appeared slightly p-type initially and changed to n-type after defect creation. Figure 7.1 shows the results of the hot-probe measurement for sample T837. One can see that the sample at the initial state was slightly p-type, and then changed to slightly n-type after the metastable defect creation. In corresponding to its E_a value, the Fermi level moved up from 0.92 eV to 0.82 eV below the conduction band edge.

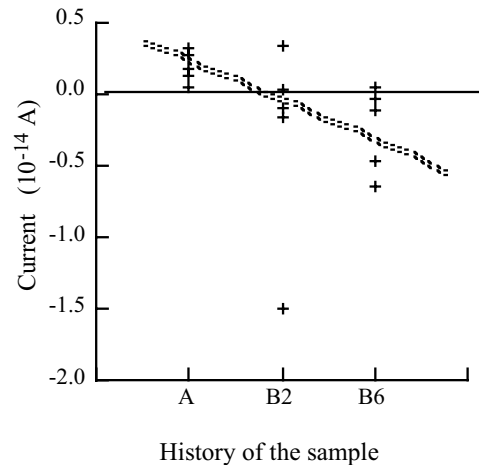


Fig. 7.1 The hot-probe data of sample T837.

The E_a of T837 was as large as 0.92 eV. After the metastable defect creation at State B2 (light soaked using 200 mW/cm^2 white light for 2 hrs) and B6 (light soaked using 200 mW/cm^2 white light for 6 hrs), the current became negative, and the E_a decreased to 0.82 eV. This change is in an opposite direction from standard PE-CVD film (A7119) in that the E_a increased from 0.73 eV to 0.77 eV after the metastable defect creation. The changes in the activation energy and the PC were partially recovered after annealing at 160°C for an hour. The activation energy recovered to ~ 0.86 eV instead of 0.92 eV. So, there

is some non-reversible degradation. In order to exam the effect of post-oxidation on the position of the Fermi level, we studied a pair of film with and without the SiN_x passivation layer. We assumed that a thin layer of SiN_x would prevent adsorption from air. The dark current as a function of temperature and annealing time are shown in Fig. 7.2. The 10 times difference in the value of the current between H1441 and H1442 can be attributed to the interface states between SiN_x and a-Si:H. This interface effect dominates the conductivity measurement on H1441. For solar cells, we have reported a 9.8% initial efficiency that became 9.2% after a few weeks of being stored in the dark. The degradation mainly came from the fill factor (FF). In order to check whether the degradation took place in the intrinsic layer, we cut sample H1540 into three pieces of H1540a, H1540b and H1541c and studied the current changes in the vacuum (x), pure oxygen (O) and the air (Δ), simultaneously. Figures 7.3(a) and 7.3(b) show the changes of the dark current at 300 K and the corresponding activation energy, respectively. The crosses in Fig. 7.3(a) show that the conductivity in the vacuum of 10^{-4} torr did not change much up to a month. However, the conductivity increased about an order of magnitude after following thermal cycles heated up to 420 K. The change in conductivity corresponded to E_a changes from 0.81 to 0.78 eV as shown in Fig. 7.3(b). The open circles show interesting changes of the conductivity in pure O_2 : the initial dark current has the same value as in the vacuum but increased and then decreased. Whereas, the current value at 300 K increased about an order of magnitude after temperature increased to 420 K; again the changes in conductivity corresponded to E_a changes as shown in Fig. 7.3(b). Finally, the open triangles show the conductivity measurement in the air: the dark current increased about 60 times more than that in the vacuum within one day and continuously increased in the air for 54 days. The current decreased an order of magnitude after E_a measurements in the air. We believe that this is due to de-adsorption of humidity at elevated temperatures.

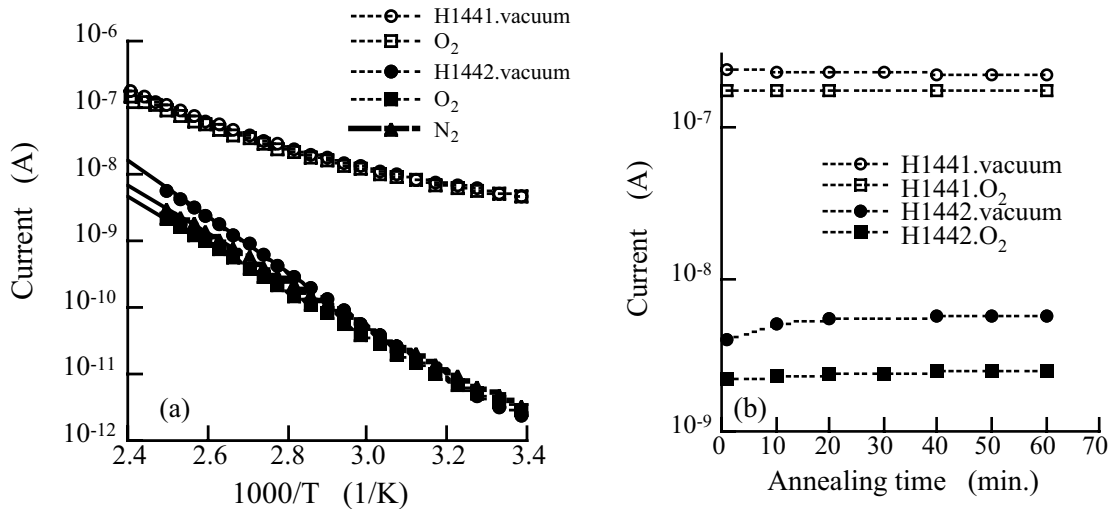


Fig. 7.2. (a) Current-temperature dependence and (b) current as a function of annealing time at 420 K, for samples of H1441 and H1442 with- and without SiN_x passivation layer. The samples were mounted in the vacuum and in pure oxygen or nitrogen, respectively.

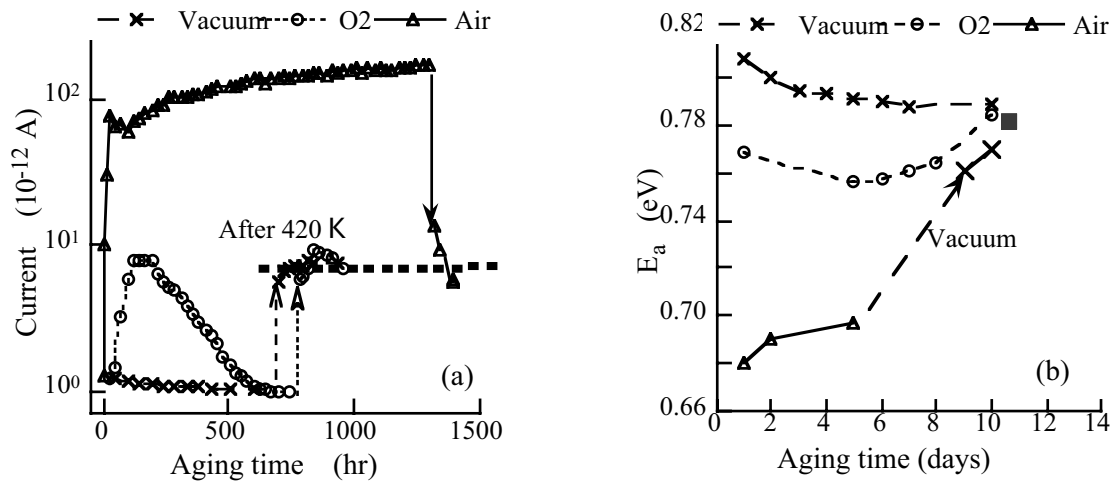


Fig. 7.3 Degradation experiments: (a) the dark current at 300 K for samples of H1540a in vacuum (x), H1540b in pure O₂ (O), and H1540c in the air (Δ). The arrows indicate the current after E_a measurements. (b) The E_a obtained from the three samples after the current measurements at 300 K for about a month. The arrow indicate the measurements were done in vacuum for H1540c.

As shown in Figs 7.3(a) and 7.3(b), the final values of both the current at 300 K and their activation energy E_a tended to reach the same value. The above results suggest that H₂O from the air has a stronger effect than the pure O₂. The source of the degradation in the dark can be related to trace oxygen incorporation at 300 K in the air or at 420 K in a 10^{-4} torr vacuum (we can not exclude the fact that the structural relaxation may also play a role) that results in an upward movement of the Fermi-level position. Consequently, the hole-mobility-lifetime product decreases and then the FF decreases.

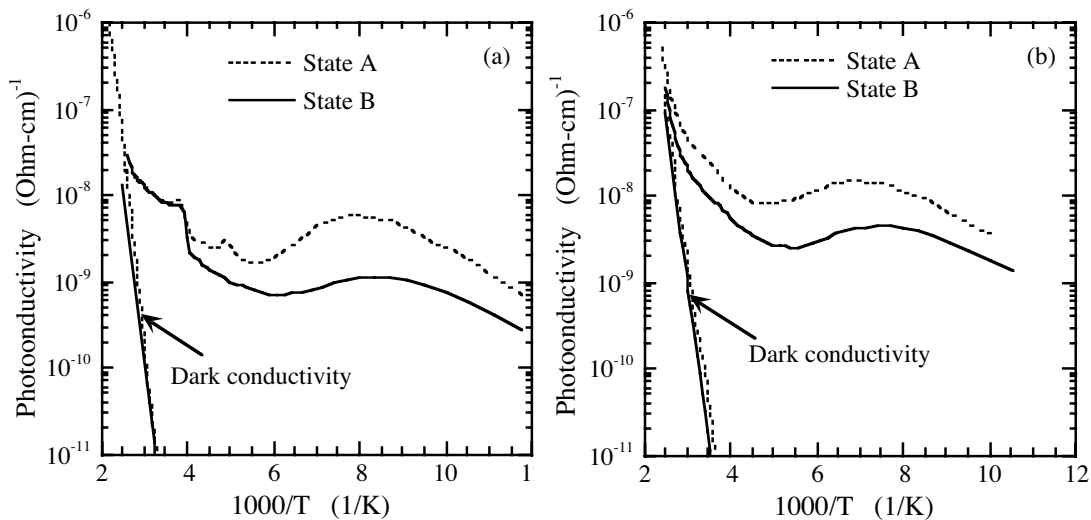


Figure 7.4 PC temperature dependence for (a) HW film T779 and (b) PE-CVD film A7119.

All of the above results showed that the changes in activation energy, in other words, the Fermi-level position were crucial to understanding the degradation in the dark. Since the gap states were crucial for the Fermi-level position, we compared the gap states between HW- and PE-CVD films in Figure 7.4 using PC temperature dependence. To show the opposite movement of the Fermi-level positions in these two films, the dark conductivity curves are also plotted in Figs 7.4(a) and 7.4(b). We found that there are two extra PC enhancement peaks at ~200 K and 250 K for HW film, and the ~200 K peak disappeared after light soaking. No matter what those states are, the disappearance of the deep traps is consistent with the upward movement of the Fermi level. One may also notice that the PC value does not decrease at ~ room temperature at State B for the HW film but it does for the PECVD film.

VII.4 Conclusions

For HW a-Si:H samples, we have observed the decreases in the FF of the solar cells and the dramatic changes in the dark conductivity for the i-layer regarding the various gases and thermal cycles. Three effects could be involved in the changes that are: surface adsorption, oxygen incorporation and thermal relaxation. We observed that the surface adsorption of H₂O in the air resulted in a great rising of the dark conductivity as shown in Fig. 7.3(a). The value of activation energy was slightly decreased after temperature cycles in the vacuum. When the activation energy decreased from ~0.9 eV to ~0.8 eV, the material changed from slightly p-type to slightly n-type, as shown in Fig. 7.1. This resulted in a decrease of the mobility-lifetime product of holes, and then a decrease of FF. We suggest that the degradation of both materials and solar cells may share the same origin. With prolonged storage time in the air at 300 K or being heated to 420 K in a 10⁻⁴ torr vacuum, oxygen incorporation resulted in the Fermi-level position moving upward. Essentially, the differences in both the microstructures and the gap states (see Fig. 7.4) in HW- from PE-CVD samples could be in response to the degradation in the dark.

VIII. Micro-Raman Studies for Electrical-induced Structural Changes in Metal/ μ c-Si/Metal Structures Made by Hot-Wire CVD [16]

VIII.1. Sample and Experiment

Boron-doped μ c-Si:H thin films of 30-50 nm thickness were deposited on Cr-coated glass substrate at 160 °C by HW-CVD. A W wire heated to 2000 °C was used to decompose silane, H₂ and B₃H₆ (3.1% in helium) precursor gases. The flow rates for those gases are 3, 45 and 3 sccm, respectively. The devices have photolitho-graphically-defined Ag or Al top contacts with the lateral size varying from 3 to 40 μ m. The thickness of both the bottom (Cr) and the top (Ag or Al) contacts was ~ 80 nm. I-V characteristics were recorded during switching with a Keithley 2400 SourceMeter. Switching was stimulated by a current-ramp from 10 nA up to 50 mA between the top and bottom contacts with a total ramp time of about 35 seconds. Before switching, the resistance of the device depended inversely on the device area. After switching, the resistance decreased more than three orders of magnitude and became independent of the area. The surface temperature on the device during stressing and switching was probed.

A Dilor Triple Spectrograph XY Raman Spectrometer (Jobin Won-Spex ISA. Inc.) was used to analyze the material structures. Raman spectra were collected under ambient conditions using a 514.5-nm line of an argon-ion laser with a beam size of 3 μ m in diameter. The laser power was more than one order of magnitude lower than the threshold power of laser-induced crystallization. The Raman frequency was calibrated using the TO mode of a (111) c-Si wafer at 520 cm⁻¹. Two arrays of 40- μ m-diameter Cr/ μ c-Si/Ag (and Cr/ μ c-Si/Al) devices were studied. The microstructure of the μ c-Si layer was analyzed after the metal top contacts were removed.

VIII.2. Results

8.2.1. The I-V characteristics of M/a-Si/M and M/ μ c-Si/M structures

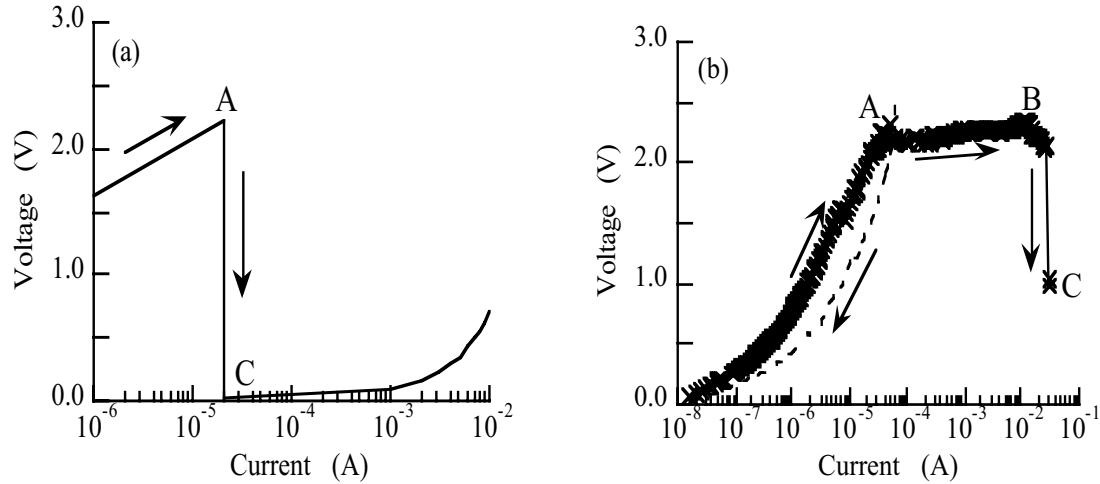


Fig. 8.1. Typical switching voltage vs. current traces in (a) a 80 μ m-diameter Cr/p⁺a-Si:H/Ag and (b) a $\sim 5 \times 5 \mu\text{m}^2$ Cr/p⁺ μ c-Si/Ag devices.

Figure 8.1 shows the comparison of the typical switching voltage-current characteristic using a current source for (a) a Cr/a-p⁺Si:H/Ag device of $5 \times 10^3 \mu\text{m}^2$ with a ramping time of ~ 0.5 sec and (b) a Cr/p⁺ μ c-Si/Ag device of $25 \mu\text{m}^2$ with a ramping time of ~ 35 seconds. The voltage across the device is plotted as a function of applied current bias. In the M/a-p⁺Si:H/M devices, as shown in Fig. 8.1(a), when the current bias increases to point A ($\sim 20 \mu\text{A}$) the voltage across the device suddenly drops from ~ 2.3 V to ~ 0.03 V at point C. Then the current near linearly depends on voltage. The switching I-V characteristic in Fig. 8.1a indicates the M/a-Si:H barrier is thermally broken down from a high- to a low-resistance state. After the thermal breakdown, there is no longer a M/a-Si:H Schottky barrier but a M/M resistance that results in the I-V linear dependence. However, in the Cr/p⁺ μ c-Si/Ag devices as shown in Fig. 8.1(b), at low bias ($\leq 1 \mu\text{A}$), the voltage is almost proportional to the current. At intermediate biases ($1 \sim 10 \mu\text{A}$), the voltage changes nearly logarithmically with the current. As the bias is raised to about $20 \mu\text{A}$, the voltage becomes saturated at about 2.2 V (point A). The voltage remains almost constant until the bias reaches about 20 mA (point B) when the voltage drops to a lower value of about 1.0 V (point C). At the same time, the device resistance permanently decreased to about 500Ω . The status of the device depends on the applied bias current. At bias $\leq 10 \mu\text{A}$, the voltage-current characteristic is reversible indicating no switching processes yet. When the bias increases to $10 \mu\text{A}$ or a little beyond, hysteresis is observed as shown by the dotted line in Fig. 8.1(b). This hysteretic behavior is repeatable, and little irreversible change occurs provided that the bias is never increased beyond the point A. When the bias current continually increases from $20 \mu\text{A}$ to 20 mA, the voltage saturated between A and B. An irreversible resistance decrease was observed at a point between A and B which implies irreversible changes of the structure. Finally, between points B and C, the voltage drops to 1.0 V with a resistance dropping to a low value. Whatever, this switching behavior is very different from what is observed in the a-Si:H devices where no saturation in voltage occurs before switching. And the voltage shows an instantaneous big drop once the bias reaches a critical value compared to a gradual and relatively small drop in the μ c-Si:H devices. After switching, the resistance is considerably lower than that in a comparable μ c-Si:H device.

8.2.2. Raman studies before and after switching of the M/ μ c-Si/M structures

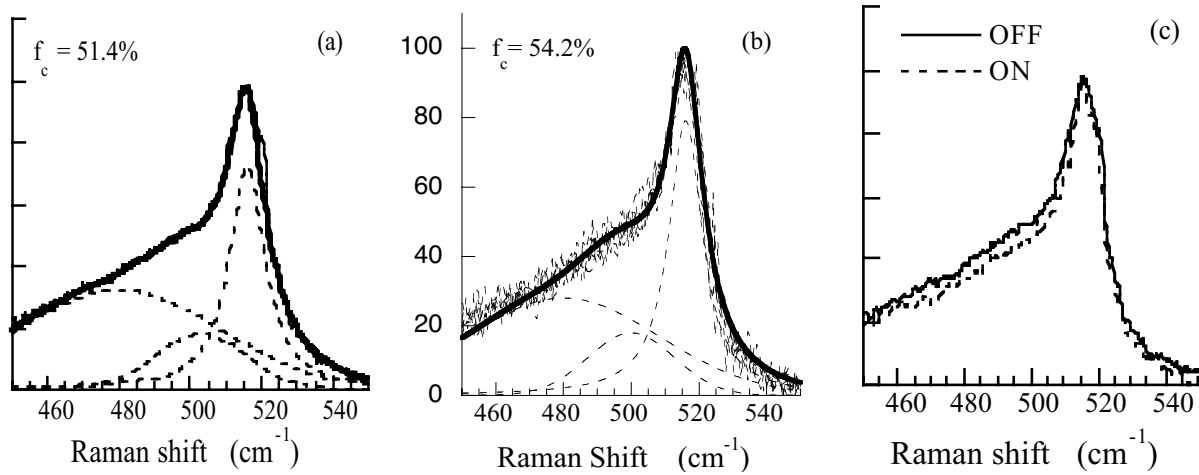


Fig. 8.2. The Raman spectra fitted using three functions for (a) the seven non-switched, (b) the eight switched devices, and (c) comparing the spectra in (a) and (b).

Previous work on M/p⁺a-Si:H/M devices was unclear as to whether there were any structural changes of the a-Si:H matrix during the forming process. In order to explore whether structural change took place during the switching in M/p⁺ μ c-Si:H/M devices, we measured Raman spectra before and after electrical switching. Raman is a sensitive tool for measuring the degree of crystallinity in μ c-Si:H materials. Two arrays of 40- μ m-diameter Cr/p⁺ μ c-Si:H/Ag and Cr/p⁺ μ c-Si:H/Al devices with a μ c-Si:H layer of 30-50 nm thickness were studied. The microstructure of the μ c-Si:H layer was analyzed after the metal top contacts were removed. For the first array (Ag contact), the Raman spectra of seven non-switched and eight switched devices were measured. The Raman laser beam excited the center of each device. The Raman signals were weak compared to the signals from other μ c-Si samples that have been studied. Long time accumulations (4000 sec for one spectrum) were needed to achieve an acceptable signal to noise ratio. Figure 8.2 shows the curve fitting of the average spectrum from (a) seven non-switched devices, (b) eight switched devices and (c) the overall average of the Raman spectra before and after switching. The data fitting results indicate that an average c-Si volume fraction increased from 51.4% to 54.2%, and the c-Si bandwidth became narrower from 12 to \sim 11 cm⁻¹ after switching.

The surface temperature on a device during switching was probed using a fine thermocouple that touched the top contact. It was seen that the surface temperature rises linearly in time from 25 °C to 40 °C during the period of voltage saturation. Finally, temperature drops dramatically with the voltage when the switching finished. The small device size and the likelihood of heat loss through the thermocouple preclude quantitative conclusions from the surface temperature measurements. The temperature in the bulk must be higher than at the surface. These observations suggest that the voltage saturation and the irreversible switching were closely related to sample heating.

VIII.3. Summary

P-type doped microcrystalline Si film deposited on Cr-coated corning 1737 glass by HW-CVD at a substrate temperature of 160 °C was used in metal/p⁺ μ c-Si/metal switching devices. Ag or Al was used for the top contact with a diameter of 3-40 μ m. After switching, the resistance decreased from >1 M Ω to <1 k Ω and became independent of the area. Compared to M/p⁺a-Si:H/M devices we found that (a) the switching in

the $\mu\text{-Si}$ devices generally required lower applied voltage than comparable a-Si:H switches, (b) the I-V characteristic of the switching processes showed a saturated voltage region. We used Micro-Raman to study structural changes due to switching processes. The incident laser beam was 3 μm in diameter. Numbers of locations (10-25 spots) were scanned across each device. We found statistically that the average c-Si volume fraction increased from $\sim 51.4\%$ to $\sim 54\%$. We have described a conducting percolation path through the g.b. regions that connect the top and bottom contacts, which results in a low resistance state permanently.

VIII.4. Conclusion

By means of micro-Raman spectroscopy, we found a small but statistically reproducible increase in crystalline volume fraction after switching in metal/ $p^+\mu\text{-Si}$ /metal devices. We conclude that an increase of crystallinity of the bottom of the i-layer was involved in the electrical switching processes.

IX. Buffer-layer Effect on Mixed-Phase Cells Studied by Raman and PL Spectroscopy [17]

IX.1. Introduction

A light induced open-circuit voltage (V_{oc}) increase has been observed in mixed-phase hydrogenated silicon solar cells, where the intrinsic layer contains a small amount of nanocrystalline grains in the amorphous matrix. An increase of PL intensity and a blue shift of the peak energy at 80 K have been observed previously in an *in-situ* light soaking experiment. The V_{oc} increase was initially explained by light-induced structural changes, i.e. an expansion of the amorphous phase and a reduction of the crystalline phase. However, the structural change model explains the light-induced enhancement of volume on the order of 0.1-0.01%, while the observed V_{oc} increase is as large or greater than 15%. Both XRD and Raman did not find any observable light-induced structural changes in the mixed-phase materials. Meanwhile, micro-Raman found non-uniform distribution of the nanocrystalline grains on a micrometer-scale in the mixed-phase cell. Experimental results also showed that the V_{oc} enhancement can be suppressed by applying a reverse bias during light soaking, which suggested that the effect is driven by the recombination of photo-generated carriers, the same as the usual SWE. Furthermore, when a fully a-Si buffer layer (~ 500 Å) was inserted between the mixed-phase intrinsic and the p layers, the solar cells showed high initial V_{oc} and no light-induced enhancement in V_{oc} . Based on those observations, we have proposed a two-diode equivalent-circuit model, which explains most of the experimental results. A mixed-phase cell was considered as two diodes connected in parallel: one cell with an amorphous signature of $V_{oc} \sim 1.0$ V and the other with a microcrystalline signature of $V_{oc} \sim 0.5$ V. The lateral transport between the two cells is negligible. According to the experimental I-V characteristics for good and poor quality $\mu\text{-Si}$ cells, the V_{oc} increase in a mixed-phase cell can be understood as the metastable defect creation in both $\mu\text{-Si:H}$ and a-Si:H diodes. Indeed, the increase of V_{oc} is always accompanied with degradation of the fill factor (FF) and short circuit current density (J_{sc}). A thin a-Si:H (100 Å) buffer layer did not change the light-induced V_{oc} increase, which was explained by carrier tunneling through the thin buffer layer. However, a thick (500 Å) buffer layer eliminated the light-induced V_{oc} increase, since it blocks the current path through the microcrystalline phase. We use micro-Raman and PL spectroscopy to further study the effects of an a-Si:H buffer layer on the microstructure and electronic density of states in mixed-phase solar cells.

IX.2. Sample and Experimental

Mixed-phase silicon $n-i-p$ solar cells were deposited using a RF glow discharge on specular stainless steel (ss) substrates. The i layer is about 250-nm thick. The top contacts are Indium-Tin-Oxide (ITO) dots with an active area of 0.25 cm^2 . The solar cells in the first group were from sample L13869, where differences in the crystalline volume fraction and cell performance are due to a nonuniform deposition. In this sample,

no a-Si:H buffer layer was deposited between the mixed-phase intrinsic layer and the doped layers. The cells in the second (sample L13868) and third (sample L13870) groups were deposited under the same conditions as in the first group except an a-Si:H buffer layer with a thickness of 100 Å and 500 Å, respectively, was deposited between the *p* layer and the *i* layer. The initial cell performances are listed in Table IX.1. In the initial state, the 100 Å thick buffer layer blocks the shunt current and increases V_{oc} and FF for the mixed-phase solar cells (cell 11 and cell 13), but does not show an effect on the cell with a fully amorphous signature (cell 23). Increasing the thickness of the buffer layer to 500 Å, the initial V_{oc} is still increased for the mixed-phase cells, but the FF decreases due to a kink in the J-V curve caused by inadequate tunneling through the a-Si:H buffer layer. After light soaking, the light-induced V_{oc} increase was observed in both the cells with no buffer layer and with a 100 Å thick buffer layer, but was not observed in the cells with a 500 Å thick buffer. Details can be found elsewhere.

Table IX.1. The initial performance of the mixed-phase solar cells with different a-Si:H buffer layers

Sample #	Cell #	Buffer (Å)	P_{max} (mW/cm ²)	J_{sc} (mA/cm ²)	V_{oc} (V)	FF
L13869	11	0	4.39	10.8	0.695	0.587
	13	0	5.47	10.3	0.852	0.621
	22	0	7.05	10.3	1.001	0.682
L13868	11	100	4.77	10.9	0.725	0.604
	13	100	6.08	10.4	0.905	0.644
	23	100	7.08	10.4	1.003	0.680
L13870	11	500	4.19	11.4	0.911	0.403
	13	500	6.83	11.3	0.970	0.625
	22	500	7.35	11.3	0.979	0.664

Raman measurements were made under ambient conditions on these solar cells using the 514.5-nm line from an argon-ion laser. The frequency was calibrated using the TO mode of a (111) c-Si wafer at 520 cm⁻¹. The penetration depth of the 514.5-nm light is ~ 600 Å for a-Si:H. Therefore, the structure of the top layer, which includes the buffer layer, was measured. Four spots were studied for each cell to evaluate the structural non-uniformity. PL spectra were measured in a temperature range of 80-300 K using a 632.8-nm laser excitation. The penetration depth of the 632.8-nm light is ~1 μm for a-Si:H. Hence, the overall electronic states in the a-Si:H buffer layer and the mixed-phase intrinsic layer are probed.

IX.3. Raman results

Figure 9.1 shows the Raman spectra for the nine cells on the three samples. The three curves from the bottom to top in each plot are arranged with increasing microcrystallinity (decreasing V_{oc}). One can see that the corresponding curves in Fig. 9.1(b) for the samples with a 100 Å thick a-Si:H buffer layer are almost identical to those in Fig. 9.1(a) for the samples with no buffer layer. This is because the 514.5-nm laser light penetrates through the 100 Å thick a-Si:H buffer layer, and the signature of the microcrystalline grains still appears on certain areas of the cell. However, no microcrystalline signature is observed on the spectra of the sample with a 500 Å thick a-Si:H buffer layer since the Raman scattering is mainly from the a-Si:H buffer layer. Concerning the relation between the Raman spectrum and V_{oc} , we find that for $V_{oc} \geq 0.911$ V, regardless of the crystallinity and the buffer layer, the TO mode peaked at ~ 480 cm⁻¹ with a width of 68 cm⁻¹ but without the peak or shoulder at 520 cm⁻¹, indicating a typical amorphous structure. In this case, the crystallinity in the probed region near the *i/p* interface is below the measurement sensitivity.

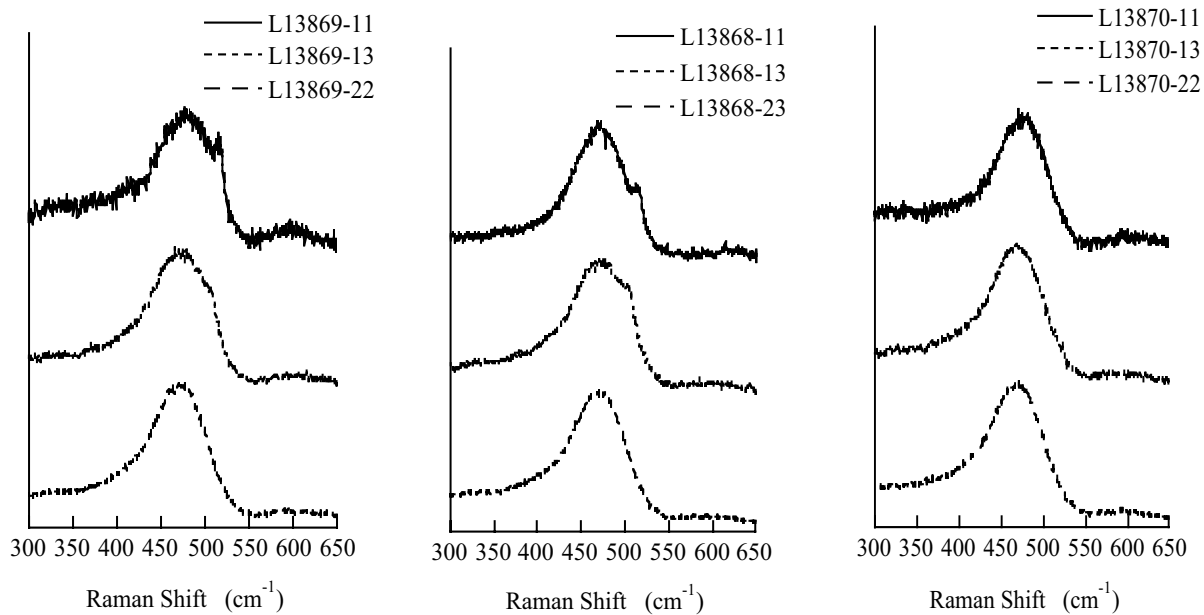


Fig. 9.1. Raman spectra for the cells on (a) L13869, (b) L13868, and (c) L13870, corresponding to no buffer layer, 100 Å thick a-Si:H buffer layer, and 500 Å thick a-Si:H buffer layer, respectively.

IX.4. PL results:

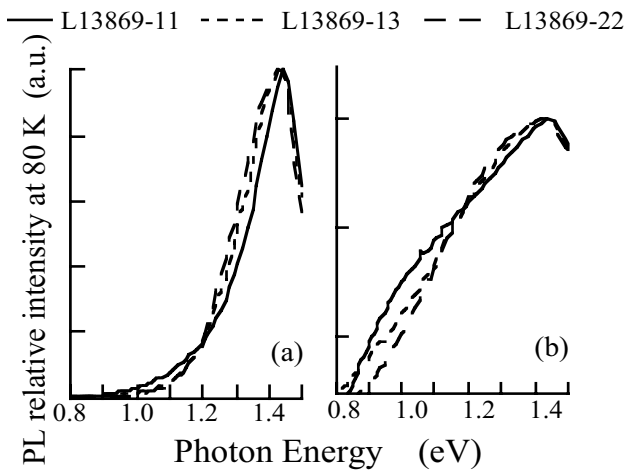


Figure 9.2. PL spectra at 80 K for cells 11, 13, and 22 on sample 13869 for (a) linear and (b) semi-log plots.

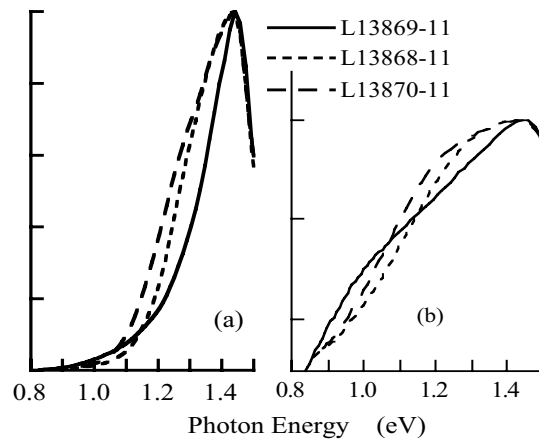


Figure 9.3. PL spectra of the low V_{oc} cells of L13869-11, L13868-11, and L13870-11 for (a) linear and (b) semi-log plots.

9.4.1. *PL spectra at low temperature:* We now show the effect of crystallinity in the mixed-phase *i*-layer on the PL lineshape. Figure 9.2 shows the PL spectra at 80 K for the three cells on sample L13869. As

the crystallinity increases, the main band becomes narrower; and the low energy (<1.2 eV) signal increases as seen clearly in the semi-log plot. When a portion of the microcrystalline phase increases, the band tail of the a-Si:H matrix becomes narrower, and extra radiative recombination in the g.b. region appears. We then show the effect of the a-Si:H *i/p* buffer layer on the PL lineshape. Figure 9.3 plots the PL spectra of cell 11 from the three samples. These cells are located at the same position on the substrate, but with different thickness of the a-Si:H buffer layer (0, 100 Å, and 500Å). The a-Si:H buffer layer makes the PL main band broad, and the low energy PL band from the g.b. regions is suppressed, which is similar to decreasing the crystallinity as shown in Fig. 9.2.

9.4.2. PL intensity temperature dependence: The differences in the PL features among the nine cells can also be seen from the temperature dependence of the PL intensity (I_{PL}). As shown in Fig. 9.4 for mixed-phase cells, the PL spectrum generally contains three components: a main band from a-Si:H at high energy with a strong temperature dependence (O), a g.b. (Δ) band at low energy with a weak temperature dependence, and a defect band (\blacksquare) that appears only at $T > 180$ K. For the cells with no a-Si:H buffer layer (sample L13869), with the increase of crystallinity (from cell 22 to 11), the PL intensity of the g.b. band increases, and the slope of the I_{PL} -T plot of the a-Si:H component becomes steeper. By fitting the data to $I_{PL} = I_0 \exp(-T/T_L)$, we obtained a PL characteristic temperature of $T_L \sim 20$ K for cell 11, which is smaller than those from the other two cells (~ 22 K). A smaller T_L implies a narrower band tail. Therefore, the PL intensity result is consistent with the PL lineshape, where cell 11 has the narrowest bandwidth as shown in Fig. 9.2. For the cells with a 100 Å thick a-Si:H buffer layer (sample L13868) as shown in Fig. 9.4 (b), the a-Si:H main-band and defect-band for the three cells are close to each and the g.b. band still appears PL contribution from the a-Si:H buffer layer. The spectra in Fig. 9.4(c) show typical characteristics for intrinsic a-Si:H films. Only the a-Si:H main-band and the defect-band are observed. The g.b. band is in the same order as in Fig. 9.4(a) but with a relatively weak intensity, which is due to the completely suppressed due to the PL contribution from the 500 Å thick a-Si:H buffer layer. In addition, the PL spectra for these three cells show the common features of the a-Si:H, including the T_L around 20-22K, the PL peak energy around 1.40-1.42 eV at 80 K, and the temperature coefficient of the peak energy around 1.5-2.0 meV/K. These data indicate a good quality a-Si:H matrix for the cells

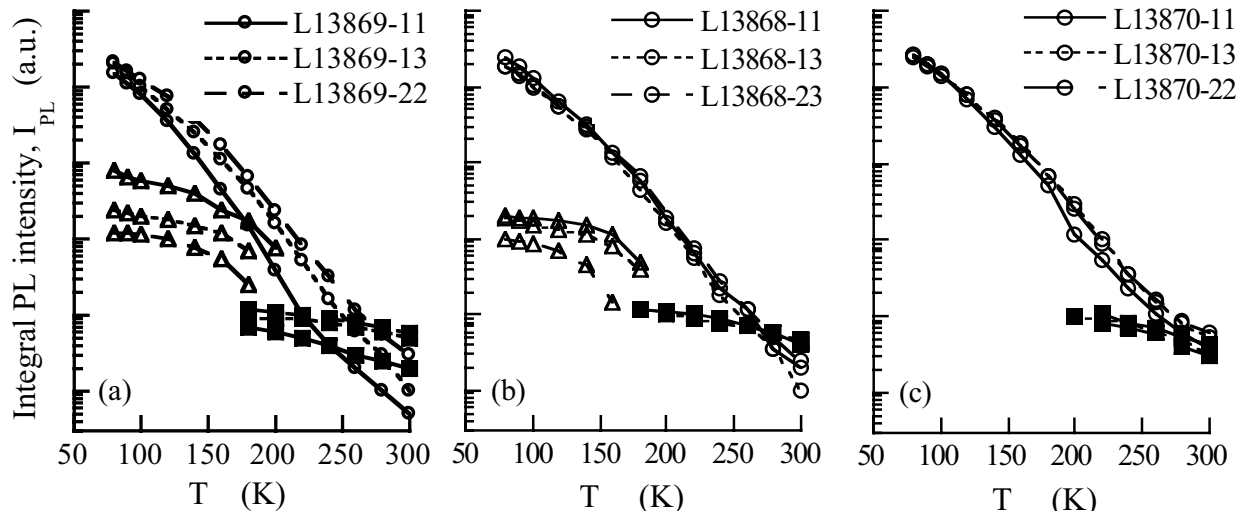


Fig. 9.4. PL intensities vs. temperature for cells of (a) L13869, (b) L13868, and (c) L13870, where circles represent the a-Si:H main band, triangles the g.b. band, and squares the defect band.

9.4.3. *in-situ* light soaking effect

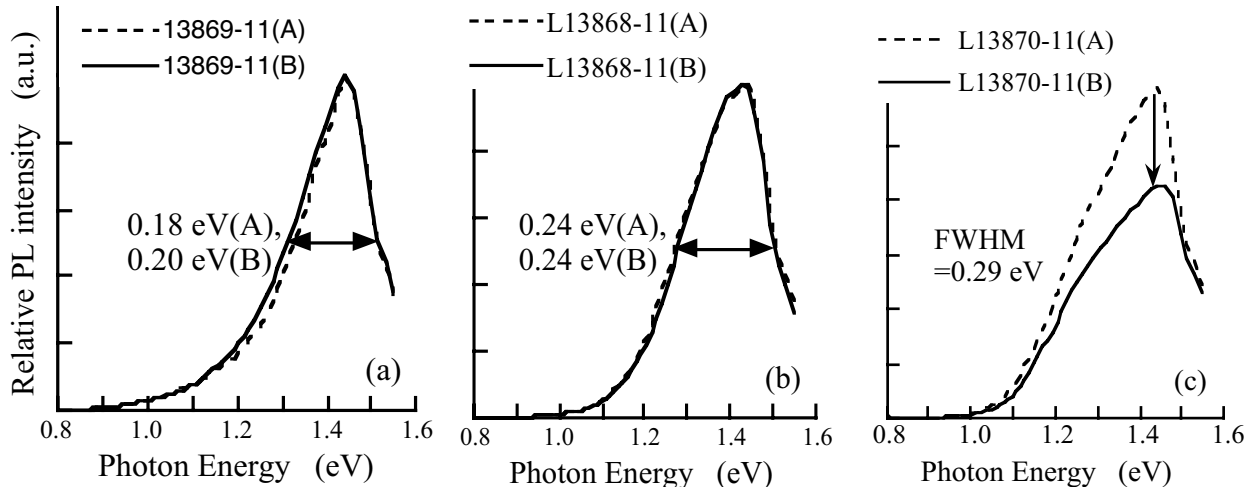


Fig. 9.5 PL spectra at 80 K before and after light soaking for cells of (a) L13869-11, (b) L13868-11, and (c) L13870-11.

After the PL was measured in the initial state (state A), *in-situ* light soaking was done at room temperature for 4 hours using a 200 mW/cm^2 white light with an infrared cut-off filter. The PL spectrum was then measured at temperatures from 80 K to 300 K in the light soaked state (state B). Correlated with V_{oc} increase an increase of PL intensity at 80 K have been observed in an *in-situ* light soaking experiments in mixed-phase solar cells. It was explained by light-induced structural changes, i.e. an expansion of the amorphous phase and a reduction of the crystalline phase. Figure 9.5 shows the PL spectra at 80 K before and after light soaking for cells L13869-11, L13868-11, and L13870-11. For the cell without a-Si:H buffer layer, we find that the PL main band becomes slightly wider and the PL total intensity also increases slightly in Fig. 9.5(a), consistent with our previous observation. For cell L13868-11 in Fig. 9.5(b), no detectable change is found on the PL spectra, which could be due to the opposite effect of the thin a-Si:H buffer layer (PL intensity decreases upon light soaking) and mixed-phase intrinsic layer (PL intensity increases upon light soaking) on PL. When the a-Si:H buffer layer was as thick as 500 \AA , the light soaking effects in the buffer layer dominate. The cell L13870-11 in Fig. 9.5(c) shows a large change in both the lineshape and intensity. The total PL intensity is decreased by $\sim 40\%$ and the relative intensity of the defect band increases, which is normally observed in a-Si:H.

IX. 5. Summary

We use micro-Raman and PL spectroscopy to study the effects of an a-Si:H buffer layer at the *i/p* interface of the mixed-phase silicon solar cells. We find that the signature of the crystalline 520 cm^{-1} mode still appears on the Raman spectrum for the cells with a 100 \AA thick a-Si:H buffer layer; but it completely disappears for cells with a 500 \AA thick a-Si:H buffer layer. At 80 K, the PL spectral lineshape reflects the features of the electronic states in the band tails. The characteristics of the PL spectra of the mixed-phase cells are a narrower main band than the standard a-Si:H band and an extra low energy band from the grain boundary region. As the thickness of the a-Si:H buffer layer increases, the PL main band becomes broader, and the low energy band is depressed. We find that, after light soaking, the PL main band is slightly broadened for the cells with no a-Si:H buffer layer, almost no change for the cells with a 100 \AA thick buffer layer, and a remarkable decrease in total PL intensity for the cells with a 500 \AA thick

buffer layer. In addition, the PL intensity of the defect band increases after light soaking for the cells with a 500 Å thick buffer layer, where light-induced defect generation in the a-Si:H buffer layer masks the changes in the mixed-phase intrinsic layer.

IX. 6. Conclusion: The Raman and PL results could explain previous observations of the effect of an thin a-Si:H buffer layer on the performance and metastability against light soaking for mixed-phase solar cells.

X. Correlation of Hydrogenated Nanocrystalline Silicon Microstructure and Solar Cell Performance[18]

X.1. Introduction

a-Si:H solar panels have been used for both terrestrial and space applications. One limitation of such panels is the light-induced degradation caused by the metastability of a-Si:H. Although much effort has been made to optimize solar cell structures, such as using a spectrum splitting triple-junction structure, the light-induced degradation still exists in a-Si:H based solar cells. In order to make high efficiency and high stable thin film solar cell, hydrogenated nanocrystalline silicon (nc-Si:H) solar cell has received a great deal of attention in the last decade due to its lower light-induced degradation and higher current density than a-Si:H cell. Initial efficiencies of over 10% for a single-junction nc-Si:H solar cell and over 14% for a-Si:H/nc-Si:H double-junction solar cell have been reported. At United Solar, several techniques have been used to increase the deposition rate and improve cell performance. It is well accepted that a high quality material is essential for achieving high efficiency solar cells. Therefore, it is very important to find a direct correlation between material properties and device performance for improving cell efficiency. In previous studies, Raman and PL spectroscopy have been used to characterize the microstructure and electronic states in nc-Si:H materials and solar cells. The Raman TO mode was used to deduce the crystalline volume fraction (X_c). For the PL spectra of nc-Si:H, a relatively narrow band at low energy was found to be the characteristic peak of nc-Si:H. To distinguish this low energy peak from the defect peak in conventional a-Si:H materials, we measured the temperature dependence of PL from 15 K to 300 K [19] and found that both the intensity and the peak energy position of the low energy PL peak in nc-Si:H are higher at low temperatures than at high temperatures. This behavior is in contrast to the defect peak in a-Si:H where the defect PL has a weak temperature dependence and is undetectable at low temperatures. In nc-Si:H, when the temperature was increased from 15 to 180 K, the intensity of the nanocrystalline related peak was rapidly quenched, and the peak energy shifted from 1.0 eV to 0.83 eV. Above 180 K, the defect peak appeared and overlapped with the PL from grain boundary regions. The behavior of the low energy PL peak in nc-Si:H was explained in terms of the carrier thermalization in an exponential band tail in the grain boundary region. The tail width kT_0 was found to be 20-24 meV, which is about half the value in typical a-Si:H. We used PL and Raman to study the relationship between the material properties and the device performance of nc-Si:H solar cells made using radio frequency (RF), modified very high frequency (MVHF), and microwave (μ W) glow discharge. In addition, not only 632.8-nm but also 442-nm laser lines are used for PL excitation to distinguish the difference in electronic density of states between the top layer and bulk.

X.2 Sample

Several *n-i-p* nc-Si:H solar cells were deposited on Ag/ZnO back reflector using various techniques at different deposition rates. Indium-tin-oxide ITO dots with an active area of 0.25 cm² were deposited on the *p* layer as the top contact. J-V characteristics was measured under an AM1.5 solar simulator at 25 °C. Quantum efficiency was measured from 300 nm to 1000 nm to calibrate the J_{sc} . Table X.1 summarizes the solar cell deposition conditions and J-V characteristics. Raman measurements were made directly on

the solar cells under the ambient condition using the 514.5-nm line from an argon-ion laser. The penetration depth of the 514.5-nm light is ~60 nm for a-Si:H and is larger for nc-Si:H.

Table X.I. Preparation conditions and solar cell performance of the nc-Si:H solar cells studied.

Dep. method	Sample ID#	d (μm)	Rate ($\text{\AA}/\text{s}$)	Eff (%)	J_{sc} (mA/cm^2)	V_{oc} (V)	FF	Comments
RF	13917	1.1	1	6.66	23.43	0.472	0.593	Flat H2 dilution, ambient stable
	14085	1.0	1	7.00	22.55	0.493	0.630	H2 dilution profiling , ambient stable
VHF	11667	1.1	3	6.85	23.73	0.464	0.622	Flat H2 dilution, thick <i>i/p</i> buffer , ambient stable
	10973	0.9	3	4.92	22.39	0.415	0.530	Flat H2 dilution, ambient stable
	10976	1.1	3	5.00	23.26	0.406	0.530	Flat H2 dilution, ambient unstable
	11538	1.1	3	4.55	24.92	0.406	0.450	Flat H2 dilution, ambient stable
	11486	0.7	12	3.20	17.05	0.381	0.493	Flat H2 dilution, ambient unstable
μW	7073	0.8	20	3.03	15.22	0.390	0.510	Flat H2 dilution, ambient stable

X.3. Raman and PL results

Table X.2. Summary of the Raman and PL analyses of the nc-Si:H solar cells.

Dep. method	Sample ID#	X_{c} (%)	$X_{\text{g.b}}$ (%)	$I_{\text{PLc}}/(I_{\text{PLc}}+I_{\text{PLa}})$		T_{L} (K), 633 nm		T_{L} (K), 442 nm	
				633 nm	442 nm	nc-peak.	a-peak	nc-peak.	a-peak
RF	13917	80.6	35.8	68.7	92.8	19.3	17.4	17.8	-
	14085	53.4	13.1	32.5	3.4	20.7	21.7	22.0	18.1
VHF	11667	40.4	5.0	26.3	2.1	21.7	23.7	20.2	15.2
	10973	74.8	30.8	5.1	24.1	15.6	21.1	15.2	-
	10976	79.0	34.5	32.9	87.0	19.9	23.3	18.7	-
	11538	77.8	34.5	25.1	95.0	17.8	23.0	16.7	-
	11486	72.2	31.1	1.0	18.5	31.2	21.5	22.2	-
μW	7073	37.6	14.5	4.0	3.7	36.9	22.8	29.1	-

where X_{c} , and $X_{\text{g.b}}$, are the total nanocrystalline volume fraction included in the grains and the grain boundaries and the grain boundary volume fraction calculated from Raman spectra, respectively, $I_{\text{PLc}}/(I_{\text{PLc}}+I_{\text{PLa}})$ the fraction of the nanocrystalline PL intensity, and T_{L} the characteristic temperature of PL as described in the text.

Figure 10.1 shows the Raman spectra of the TO mode for the eight cells listed in Table X.1. The PL spectra for the same samples were measured in a temperature range of 80-300 K using 632.8-nm and 442-nm laser line excitations to probe the electronic properties in the bulk of the nc-Si:H intrinsic layer and the top layer near the *i/p* interface, respectively. The PL spectra were plotted in Fig. 10.2 for comparison with the Raman results. Table X.2 lists the calculated X_{c} and $X_{\text{g.b}}$, values from Fig.10.1.

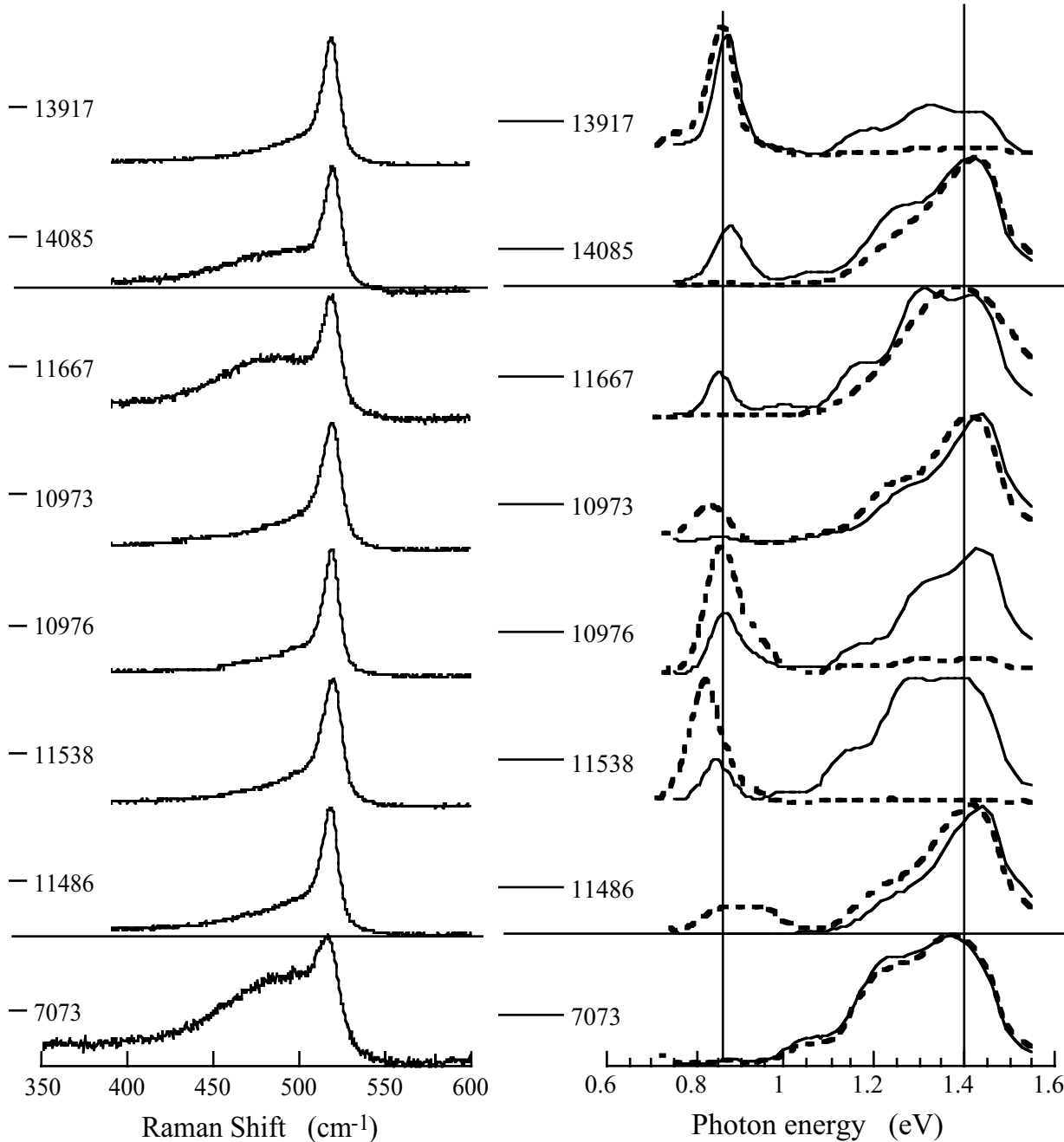


Figure 10.1. Raman spectra of the eight nc-Si:H solar cells.

Figure 10.2. PL spectra of the same nc-Si:H solar cells at 80 K excited by 632.8-nm (solid) and 442-nm (dashed) laser beams.

As shown in Fig. 10.2, most of the nc-Si:H solar cells show two separated PL peaks at 80 K. The broad peak at ~1.4 eV originates from the tail-to-tail radiative recombination in the a-Si:H region, while the narrow peak at ≤ 0.9 eV is related to the nanocrystalline grains and from the tail-to-tail radiative recombination in the grain boundary regions. The relative PL intensity of the grain boundary region is represented by the fraction of $I_{PLc}/(I_{PLc}+I_{PLa})$, where I_{PLc} and I_{PLa} are the integrals of the low and high energy PL peaks, respectively. One finds that $I_{PLc}/(I_{PLc}+I_{PLa})$ using 442-nm excitation change in the same

manner as $X_{g.b.}$ does. Furthermore, the width of the electronic band tails, kT_o , could be obtained from the temperature dependence of the corresponding PL intensities. According to the carrier thermalization model, $kT_o = kT_L \ln(v_o \tau_r)$, where T_L , v_o , and τ_r are the slope of I_{PL} - T plot, the attempt-to-escape frequency, and the carrier's recombination lifetime, respectively. The T_L can be deduced by fitting the experimental data into $I_{PL} = I_o \exp(-T/T_L)$. Table X.2 also summarizes the analysis of PL data for the eight nc-Si:H cells.

X.4 Discussion

We first compare the two nc-Si:H cells deposited using RF glow discharge. The main difference is that the sample 13917 was deposited using a constant hydrogen dilution, while the sample 14085 using a profiled hydrogen dilution with decreasing hydrogen dilution during the deposition. As shown in Table I, the hydrogen dilution technique has improved V_{oc} and FF significantly, but there is a slight loss in the J_{sc} . A recent study using the hydrogen dilution profiling technique has resulted in an efficiency of 8.4% of the nc-Si:H single-junction cell and 13.4% of a-Si:H/nc-Si:H double-junction cell. Raman results indicate that sample 14085 has much lower crystalline volume fraction than sample 13917, which is consistent with the observed higher V_{oc} and lower J_{sc} in the profiled cell than in the flat one. However, we need to keep in mind that the Raman measurement with 514.5-nm excitation only detects the top layer near the *i/p* interface. The crystalline volume fraction may be over-estimated for the sample with flat hydrogen dilution, but under-estimated for the sample with the profiled hydrogen. Another interesting observation is that the grain boundary volume fraction is relatively lower in the sample 14085 than in the sample 13917, which implies that a low percentage of grain boundary is desirable for solar cell performance. Meanwhile, the hydrogen dilution profiling (#14085) results in a clear difference of the electronic density of states in the top layer from the bulk as shown in the PL spectra, i.e. the amorphous-related peak dominants and the nanocrystalline-related peak diminishes when the excitation was changed from the long wavelength (632.8-nm) to the short wavelength (442-nm). This is opposite to the samples with flat hydrogen dilution (#13917), where the nanocrystalline-related peak increases at the top layer.

The MVHF deposited nc-Si:H cells (#11667) with a thick a-Si:H *i/p* buffer layer showed an improved cell performance due to reduced shunt current. Raman measurement showed a low crystalline volume fraction with very little of grain boundary component and PL showed a low nanocrystalline related peak at the *i/p* interface layer. Both results are consistent with the expected effect of the a-Si:H buffer layer. We found that some unoptimized nc-Si:H solar cells showed a significant ambient degradation related to post-oxidization. Cells 10973 and 10976 are made under two conditions such that one produces no ambient degradation and the other one does. Raman results show that sample 10976 has slightly high X_c , whereas, PL spectra are very different. Sample 10976 has a much higher nanocrystalline related PL peak than sample 10973, especially, at the top layer, indicating a high non-uniformity along the growth direction. It has been showed that a high nanocrystalline volume fraction with large grains easily causes micro-cracks, post-oxidization, and consequently the ambient degradation.

Now we discuss the band tail width deduced from PL temperature dependence. As listed in table II, the T_L related to the amorphous PL peak is in the range from 17 to 23 K for all the eight cells in the bulk (632-nm excitation), and in the top layer (442-nm excitation) T_L is $\sim 17 \pm 2$ K for the two high efficiency cells. The T_L for the nanocrystalline related PL peak could be categorized into two types. In the cells with reasonable performance, the T_L is smaller than 23 K and changes very little from the bulk to the top layer. In contrast, in the high rate MVHF (#11486) and the microwave cell (#7073) have large T_L values (31-37 K) in the bulk. Since the band tail width kT_o is proportional to T_L , the large T_L in the poor nc-Si:H solar cells implies that a broad band tail in the nanocrystalline region leads to a poor cell performance. Normally, the band tail in the nanocrystalline region is considered from the grain boundary states. Therefore, finding ways to improve the grain boundary quality (less defects and less distorted bonds) would be beneficial for improving the nc-Si:H solar cell performance.

X.5. Summary

We used Raman and PL spectroscopy to study the relationship between the material properties and the solar cell performance of hydrogenated nc-Si:H. The crystalline volume fraction was deduced from the Raman spectrum. Generally, a high X_c leads to a high short circuit current density and a low open circuit voltage. PL spectra were measured using 632.8-nm and 442-nm laser lines. There are two distinguished PL peaks at 80 K, one at ~ 1.4 eV originating from the amorphous region, while the other at ≤ 0.9 eV from the nanocrystalline grain boundary regions. Generally, the intensity fraction of this low energy PL peak, $I_{PLc}/(I_{PLa}+I_{PLc})$, was larger for 442-nm than 632.8-nm excitation, indicating an increase in crystallinity along the growth direction. However, for the best initial performance cells obtained by H_2 dilution profiling and the *i/p* buffer layer, the intensity fraction $I_{PLc}/(I_{PLa}+I_{PLc})$ decreased from the bulk to the top *i/p* interface. The Raman and PL results give insight into the correlation between the microstructures and the cell performance, and verified that properly-controlled crystallinity in the intrinsic layer and buffer layer at the *i/p* interface layer are important for optimizing nc-Si:H solar cells.

The Raman results show that a high X_c leads to a high J_{sc} and low V_{oc} in nc-Si:H solar cells made with constant hydrogen dilution. X_c increases as film grows for flat hydrogen dilution. However, hydrogen dilution profiling, with dilution decreasing as film grows, lowers X_c as measured by 514-nm light with a penetration depth of 60 nm. The PL spectra excited by 632-nm and 442-nm laser beams indicate that the crystallinity increased along the growth direction for the flat hydrogen diluted samples. The top layers in the hydrogen dilution profiled nc-Si:H cells, however, have a higher amorphous PL signal than in the bulk. The improved cell efficiency by hydrogen dilution profiling indicates that a properly controlled X_c distribution along the growth direction is a very useful technique to obtain high efficiency. The band tail width in the grain boundary region was deduced from the PL intensity temperature dependence. The results show that a narrow band tail in the nanocrystalline phase correlates to improved cell efficiency.

X.6. Conclusion

The Raman and PL results give insight into the correlation between the microstructures and the cell performance, and verified that properly-controlled crystallinity in the intrinsic layer and buffer layer at the *i/p* interface layer are important for optimizing nc-Si:H solar cells.

FURTHER EFFORTS

The P.Is. Daxing Han, Keda Wang have had response the LOS of Thin-Film PV Partnerships Program, No.RXL-4-44205 under a project title of Correlation between Thin Film Properties and their Solar Cell Performance Studied by PL and Raman Spectroscopies from Department of Physics, Boston College (BC)

We address the category of Specialized Contributors in a title of Correlation between Thin Film Properties and their Solar Cell Performance Studied by PL and Raman Spectroscopies. A study of the Staebler-Wronski Effect in the intrinsic layer of solar cells in relation to solar cell degradation is included.

We choose the PL and Micro-Raman spectroscopies as the main characterization methods to support thin-film PV industry R&D in improvement of solar cell's performance and reliability. PL and Raman are non-contact and non-destructive techniques that can be used on both thin film and solar cell structures. It allows us to find the correlation between the i-layer properties and the solar cell performance that is crucial for understanding the device physics and then improving cell design and optimizing preparation conditions. Our PL and Raman techniques are able to probe the uniformity in growth direction. In addition, Micro-Raman probes the horizontal uniformity. So far, we have studied a-Si and film-Si in collaboration with United Solar Ovonic Corporation and National Renewable Energy Laboratory. The same techniques can be used to study CdTe and CIS.

If awarded a subcontract, BC will participate in National R&D Team activities and continue to cooperate with the team members.

Publications

1. Hydrogen dilution profiling for hydrogenated microcrystalline silicon solar cells, Baojie Yan, Guozhen Yue, Jeffrey Yang, Subhendu Guha, D. L. Williamson, Daxing Han and Chun-Sheng Jiang, to be published in APL (2004).
2. Micro-Raman studies for electrical-induced structural changes in metal/ $\mu\text{c-Si}$ /metal structures made by hot-wire CVD, Brittany Huie, J.R. Weinberg-Wolf, E.C.T. Harley, Keda Wang and Daxing Han, Jian Hu, Pauls Stradins, Howard M. Branz, and Qi Wang. To be published in Thin Solid Films (2004).
3. MICROSTRUCTURE EVOLUTION WITH THICKNESS AND HYDROGEN DILUTION PROFILE IN MICROCRYSTALLINE SILICON SOLAR CELLS, Baojie Yan, Guozhen Yue, Jeffrey Yang, Subhendu Guha, Keda Wang and Daxing Han, MRS *symp. Proc.* **808**, A8.5 (2004), in press.
4. Increase of crystallinity during electrical switching in metal/ $\mu\text{c-Si}$ /metal structures, Jian Hu, Pauls Stradins, Howard M. Branz, Qi Wang, J.R. Weinberg-Wolf, E.C.T. Harley, Chris Lawyer, Brittany Huie and Daxing Han, MRS *symp. Proc.* **808**, A4.25 (2004), in press.
5. Correlation of Hydrogenated Nanocrystalline Silicon Microstructure and Solar Cell Performance, Keda Wang, Anthony Canning, J.R. Weinberg-Wolf, E.C.T. Harley, Daxing Han, Baojie Yan, Guozhen Yue, Jeffrey Yang, and Subhendu Guha, MRS *symp. Proc.* **808**, A9.53 (2004), in press.
6. Buffer-layer Effect on Mixed-Phase Cells Studied by Micro-Raman and Photoluminescence Spectroscopy, Andrea Hilchey, Chris Lawyer, keda Wang, Daxing Han, Baojie Yan, Guozhen Yue, Jeffrey Yang, and Subhendu Guha, MRS *symp. Proc.* **808**, A4.38 (2004), in press.
7. High-throughput chemical vapor deposition system and thin-film silicon library, Qi Wang, Fengzhen Liu, Daxing Han, Macromolecular Rapid Communications, Jan. 2004.
8. Raman study of thin films from amorphous-to-microcrystalline silicon prepared by hot-wire chemical vapor deposition, Daxing Han, J. D. Lorentzen, J. Weinberg-Wolf, L. E. McNeil, and Qi Wang, J. Appl. Phys., **94**, 5 (2003) 2930-2936.
9. Micro-Raman studies of Mixed-Phase Hydrogenated Silicon Solar Cells, J. Owens, D. Han, B. Yan, J. Yang, K. Lord, and S. Guha, Amorphous and Heterogeneous Silicon-Based Films, MRS Symposium Proc. **762**, edited by J.R. Abelson, G. Ganguly, H. Matsumura, J. Robertson, and E. Schiff, 339 (2003).
10. Toward understanding the degradation without light soaking in hot-wire a-Si:H thin films and solar cells, Qi Wang, Keda Wang, and Daxing Han, MRS Symposium Proc. **762**, edited J.R. Abelson, G. Ganguly, H. Matsumura, J. Robertson, and E. Schiff, 399 (2003).
11. Combinatorial approach to thin-film silicon materials and devices, Qi Wang, Leandro R. Tessler, Helio Moutinho, Bobby To, John Perkins, Daxing Han, and Howard M. Branz, MRS Symposium Proc. **762**, edited by J.R. Abelson, G. Ganguly, H. Matsumura, J. Robertson, and E. Schiff, 413 (2003).
12. Micro-Raman Measurements of Mixed-Phase Hydrogenated Silicon Solar Cells, J. Owens, D. Han, B. Yan, J. Yang, K. Lord, and S. Guha, Proc. NCPV review meeting (2003, 3, 21-24, Denver, CO).
13. Correlation between cell performance and film properties as function of growth rate, G. Ganguly, Daxing Han, et al, Proc. NCPV review meeting (2003, 3, 21-24, Denver, CO).
14. Narrow Gap a-SiGe:H Grown by HWCVD, Brent P. Nelson, Daxing Han, M. Boshta, B. Alavi, Rubin Braunstein, Don L. Williamson, and Yueqin Xu, Proc. NCPV review meeting (2003, 3, 21-24, Denver, CO).
15. Hydrogen Distribution, Nanostructures and Optical Properties of High Deposition Rate Hot-Wire CVD a-Si:H, Jonathan Baugh, Keda Wang, Daxing Han, and Yue Wu, Thin Solid Films **430** (2003) 95-99.
16. Neutral Dangling Bonds May Not Be The Dominant Recombination Centers For Photoconductivity In Hot-Wire a-Si:H, Daxing Han, Guozhen Yue, Qi Wang, Tatsuo Shimizu, Thin Solid Films **430** (2003) 141-144.

17. Photo- and electro-luminiscence of a-Si:H and mixed-phase alloys, Daxing Han and Keda Wang, "Critical Review of Amorphous and Microcrystalline Silicon Materials and Solar Cells" a special issue of *Solar Energy Materials and Solar Cells*, **78** (2003) 181-233.
18. Hydrogen structures and the optoelectronic properties in transition films from amorphous to microcrystalline silicon prepared by hot-wire chemical vapor deposition, Daxing Han, Keda Wang, Jessica M. Owens, Lynn Gedvilas, Brent Nelson, Hitoe Habuchi and Masako Tanaka, *J. Appl. Phys.* **93** (2003) 3776-3783.
19. Qi Wang, Eugene Iwaniczko, Jeffrey Yang, Kenneth Lord, Subhendu Guha, Keda Wang, and Daxing Han, "WIDE-GAP THIN FILM SI n-i-p SOLAR CELLS DEPOSITED BY HOT-WIRE CVD", 29th PVSC IEEE Orlando, USA, 2002.
20. A two-domain model of light-induced structural changes in hydrogenated amorphous silicon, Jonathan Baugh and Daxing Han, *Phys. Rev.* **B66** (2002) 115203.
21. Optical Properties of i-layers as a Function of Growth Rate in Correlation to the Performance of a-Si:H Solar Cells, Keda Wang, Jessica M. Owens, Jennifer Weinberg-Wolf, Daxing Han, Lynn Gedvilas, and Gautam Ganguly, *Amorphous and Heterogeneous Silicon-Based Films*, MRS Symposium Proc. **715**, edited by J.D. Cohen, H. Matsumura, J.R. Abelson, and J. Robertson, pp 571-576 (2002).
22. Characterization of Microcrystalline Transition from Amorphous Silicon as a Function of Hydrogen Dilution and Substrate Temperature of Hot-wire CVD, Keda Wang, Haoyue Zhang, Jing Zhang, Jessica M. Owens, Jennifer Weinberg-Wolf, Daxing Han, Lynn Gedvilas and Brent Nelson, *Amorphous and Heterogeneous Silicon-Based Films*, MRS Symposium Proc. **715**, edited by J.D. Cohen, H. Matsumura, J.R. Abelson, and J. Robertson, pp 147-152 (2002).
23. Correlation of Light-induced Enhancement of Open-Circuit Voltage and Structural Change of Heterogeneous Silicon Solar Cells, Jeffrey Yang, Kenneth Lord, Baojie Yan, Arindam Banerjee, Subhendu Guha, Daxing Han and Keda Wang, *Amorphous and Heterogeneous Silicon-Based Films*, MRS Symposium Proc. **715**, edited by J.D. Cohen, H. Matsumura, J.R. Abelson, and J. Robertson, pp 601-610 (2002).
24. Nanovoid-related Large Red Shift of Photoluminescence Peak Energy in Hydrogenated Amorphous Silicon, Daxing Han, Guozhen Yue, Keda Wang, Jonathan Baugh, Yue Wu, Yueqin Xu, and Qi Wang, *Appl. Phys. Lett.* **80**, 40-42 (2002).
25. Effects of Hydrogen Dilution and i-layer Thickness on a-Si:H Solar Cells Studied by Photoluminescence Spectroscopy, Guozhen Yue, Daxing Han, Jeffrey Yang, Kenneth Lord, Boajie Yan, and Subhendu Guha, NCPV Program Review Meeting, (Oct, 2001, Denver, CO).
26. Link of the Light-induced Structural Changes and the Conductivity Changes in Hydrogenated Amorphous Silicon --a Two-domain Model, Jonathan Baugh and Daxing Han, NCPV Program Review Meeting, (Oct, 2001, Denver, CO).
27. Confinement effect on spin-spin interactions in nanogas systems, Jonathan Baugh, Alfred Kleinhammes, Daxing Han, Qi Wang & Yue Wu, *Science*, **294**, issue 5546, 1505-1507 (2001).

Reference

- [1]. Daxing Han, Guozhen Yue, Keda Wang, Jonathan Baugh, Yue Wu, Yueqin Xu, and Qi Wang, *Appl.Phys. Lett.* **80**, 40-42 (2002).
- [2]. Jonathan Baugh, Alfred Kleinhammes, Daxing Han, Qi Wang & Yue Wu, *Science*, **294**, issue 5546, 1505-1507 (2001).
- [3]. P.A. Fedders, D.J. Leopold, P.H. Chan, R. Borzi, and R.E. Norberg, *Phys. Rev. Lett.* **85**, 401 (2000).
- [4]. Daxing Han, Keda Wang, Jessica M. Owens, Lynn Gedvilas, Brent Nelson, Hitoe Habuchi and Masako Tanaka, *J. Appl. Phys.* **93** (2003) 3776-3783.
- [5]. U. Kroll, J. Meier, A. Shah, S. Mikhailov and J. Weber, *J. Appl. Phys.* **80**, 4971 (1996).
- [6]. A. H. Mahan, J. Yang and S. Guha, *D.L. Willamson, Phys Rev. B* **61**, 1677 (2000).
- [7]. Daxing Han, Guozhen Yue, Qi Wang, Tatsuo Shimizu, *Thin Solid Films* **430** (2003) 141-144.
- [8]. T. Shimizu, M. Shimada, H. Sugiyama and M. Kumeda, *Jpn. J. Appl. Phys.* **40**, 54 (2001).
- [9]. T. Shimizu, M. Shimada, and M. Kumeda, *Jpn. J. Appl. Phys.* **41**, 2829 (2002).
- [10]. Keda Wang, Jessica M. Owens, Jennifer Weinberg-Wolf, Daxing Han, Lynn Gedvilas, and Gautam Ganguly, *Amorphous and Heterogeneous Silicon-Based Films, MRS Symposium Proc.* **715**, edited by J.D. Cohen, H. Matsumura, J.R. Abelson, and J. Robertson, pp 571-576 (2002).
- [11]. Ganguly, Daxing Han, et al, *Proc. NCPV review meeting* (2003, 3, 21-24, Denver, CO).
- [12]. Daxing Han, J. D. Lorentzen, J. Weinberg-Wolf, L. E. McNeil, and Qi Wang, *J. Appl. Phys.*, **94**, 5 (2003) 2930-2936.
- [13]. D. Beeman, R. Tsu, and M.F. Thorpe, *Phys. Rev. B* **32**, 874 (1985).
- [14]. J. Owens, D. Han, B. Yan, J. Yang, K. Lord, and S. Guha, *Amorphous and Heterogeneous Silicon-Based Films, MRS Symposium Proc.* **762**, edited by J.R. Abelson, G. Ganguly, H. Matsumura, J. Robertson, and E. Schiff, 339 (2003).
- [15]. Qi Wang, Keda Wang, and Daxing Han, *MRS Symposium Proc.* **762**, edited J.R. Abelson, G. Ganguly, H. Matsumura, J. Robertson, and E. Schiff, 399 (2003).
- [16]. Jian Hu, Pauls Stradins, Howard M. Branz, Qi Wang, J.R. Weinberg-Wolf, E.C.T. Harley, Chris Lawyer, Brittany Huie and Daxing Han, *MRS symp. Proc.* **808**, A4.25 (2004), 459.
- [17]. Andrea Hilchey, Chris Lawyer, keda Wang, Daxing Han, Baojie Yan, Guozhen Yue, Jeffrey Yang, and Subhendu Guha, *MRS symp. Proc.* **808**, A4.38 (2004), 35.
- [18]. Keda Wang, Anthony Canning, J.R. Weinberg-Wolf, E.C.T. Harley, Daxing Han, Baojie Yan, Guozhen Yue, Jeffrey Yang, and Subhendu Guha, *MRS symp. Proc.* **808**, A9.53 (2004), 59.
- [19]. Guozhen Yue, Laurie E. McNeil and Daxing Han, Qi Wang, *J. Appl. Phys.* **88**, 4940 (2000).

ABSTRACT

In high growth rate ($\geq 50 \text{ \AA/s}$) HW-CVD a-Si:H films, for the first time, we show gaseous molecules in nanovoids ($\sim 2\%$ volume fraction of tube-like nanoscale voids), and demonstrate that confinement on the nanometer scale generates NMR effects that have never been observed in macroscopic systems. In the same system we found the PL peak red shift. We suggest that highly strained bonds on the inner surfaces of the nanoscale voids form broad conduction-band tail states that are responsible for the PL red shift.

We characterized the structural transition from a- to nc-Si as function of H-dilution, thickness and T_s of both HW- and PE-CVD films using IR, Raman, PL, CPM/PDS and E_a et al. We found not only the c-Si volume fraction but also the g.b. and microstructures play an important role in the properties of the i-layer and their solar cell performance. We found a narrow structural transition zone in which the bond-angle variation, $\Delta\Theta$, decreases from 10° to 8° . For nc-Si samples, we found a characteristic low energy PL peak and proved that is originated from the g.b. regions.

Using micro-Raman, we found the structural non-uniformity in the mixed-phase solar cells that showed V_{oc} enhancement after light soaking. Using micro-Raman, we also found the slight increase of crystallinity in M/ $\mu\text{c-Si}$ /M devices after current forming.

In cooperation with USOC, we studied the correlation between the microstructure, the DOS, and the solar cell performance before and after light soaking using Raman and PL with varied excitation wavelength and explained the microscopic origin of the optimized conditions for the solar cell preparations. The best cells have been prepared at near the edge of the transition from amorphous to microcrystallin silicon. More detailed studies of such cells can be found in our last final technical report (1998-2001).

REPORT DOCUMENTATION PAGE

Form Approved
OMB No. 0704-0188

The public reporting burden for this collection of information is estimated to average 1 hour per response, including the time for reviewing instructions, searching existing data sources, gathering and maintaining the data needed, and completing and reviewing the collection of information. Send comments regarding this burden estimate or any other aspect of this collection of information, including suggestions for reducing the burden, to Department of Defense, Executive Services and Communications Directorate (0704-0188). Respondents should be aware that notwithstanding any other provision of law, no person shall be subject to any penalty for failing to comply with a collection of information if it does not display a currently valid OMB control number.

PLEASE DO NOT RETURN YOUR FORM TO THE ABOVE ORGANIZATION.

1. REPORT DATE (DD-MM-YYYY) May 2005		2. REPORT TYPE Subcontract Report		3. DATES COVERED (From - To) 1 October 2001–30 September 2004	
4. TITLE AND SUBTITLE Microscopic Mechanism of the Staebler-Wronski Effect in a-Si Films and High-Efficiency Solar Cells: Final Subcontract Report, 1 October 2001–30 September 2004			5a. CONTRACT NUMBER DE-AC36-99-GO10337		
			5b. GRANT NUMBER		
			5c. PROGRAM ELEMENT NUMBER		
6. AUTHOR(S) D. Han			5d. PROJECT NUMBER NREL/SR-520-37990		
			5e. TASK NUMBER PVB55101		
			5f. WORK UNIT NUMBER		
7. PERFORMING ORGANIZATION NAME(S) AND ADDRESS(ES) Department of Physics University of North Carolina Chapel Hill, North Carolina				8. PERFORMING ORGANIZATION REPORT NUMBER ADJ-1-30630-09	
9. SPONSORING/MONITORING AGENCY NAME(S) AND ADDRESS(ES) National Renewable Energy Laboratory 1617 Cole Blvd. Golden, CO 80401-3393				10. SPONSOR/MONITOR'S ACRONYM(S) NREL	
				11. SPONSORING/MONITORING AGENCY REPORT NUMBER NREL/SR-520-37990	
12. DISTRIBUTION AVAILABILITY STATEMENT National Technical Information Service U.S. Department of Commerce 5285 Port Royal Road Springfield, VA 22161					
13. SUPPLEMENTARY NOTES NREL Technical Monitor: Bolko von Roedern					
14. ABSTRACT (Maximum 200 Words) In high growth rate ($\geq 50 \text{ \AA/s}$) HW-CVD a-Si:H films, for the first time, we show gaseous molecules in nanovoids (~2% volume fraction of tube-like nanoscale voids), and demonstrate that confinement on the nanometer scale generates NMR effects that have never been observed in macroscopic systems. In the same system we found the PL peak red shift. We suggest that highly strained bonds on the inner surfaces of the nanoscale voids form broad conduction-band tail states that are responsible for the PL red shift. We characterized the structural transition from a- to nc-Si as function of H-dilution, thickness and T_s of both HW- and PE-CVD films using IR, Raman, PL, CPM/PDS and E_a et al. We found not only the c-Si volume fraction but also the g.b. and microstructures play an important role in the properties of the i-layer and their solar cell performance. We found a narrow structural transition zone in which the bond-angle variation, $\Delta\theta$ decreases from 10° to 8° . For nc-Si samples, we found a characteristic low energy PL peak and proved that is originated from the g.b. regions. Using micro-Raman, we found the structural non-uniformity in the mixed-phase solar cells that showed V_{oc} enhancement after light soaking. Using micro-Raman, we also found the slight increase of crystallinity in $M/\mu\text{c-Si/M}$ devices after current forming.					
15. SUBJECT TERMS PV; Staebler-Wronski effect; amorphous silicon (a-Si:H); solar cells; microscopic mechanism; photoluminescence (PL); Raman spectroscopies; manufacturer; thin film; light-induced degradation;					
16. SECURITY CLASSIFICATION OF:			17. LIMITATION OF ABSTRACT UL	18. NUMBER OF PAGES	19a. NAME OF RESPONSIBLE PERSON
a. REPORT Unclassified	b. ABSTRACT Unclassified	c. THIS PAGE Unclassified			19b. TELEPHONE NUMBER (Include area code)